UNIVERSITY OF CANTERBURY

MASTERS THESIS

Optical Modelling Techniques for Refinement of a Prototype Radiation Dosimeter

Author:
Lancia M HUBLEY

Supervisor:
Dr. Steven MARSH,
Dr. Juergen Meyer,
Dr. Alicia Moggré

A thesis submitted in partial fulfillment of the requirements for the degree of Master of Science

in the

School of Physical and Chemical Sciences

July 31, 2018

Abstract

This research was conducted in order to verify that the optical modelling software FRED, produced by Photon Engineering LLC of Tucson Arizona, was a suitable candidate to virtually prototype improvements to our research group's digital holographic interferometric radiation dosimeter. After extensive testing, FRED was determined to be a good candidate for such studies.

FRED was used to construct a model of the prototype dosimeter, and this model dosimeter was used to produce holograms which matched the output of the experimental dosimeter. The virtual model of the prototype was capable of accurately reconstructing doses as low as 0.01 Gy, which shows its potential for application in clinical dosimetry.

FRED was also able to accurately model the response of the dosimeter to different sources of environmental uncertainty. Case studies in measuring the uncertainty produced by atmospheric fluctuations, heat expansion and environmental noise were undertaken using FRED's scripting environment. These investigations showed that the virtual dosimeter's response was in accordance with interferometric theory and the observations of Cavan et al. in her PhD thesis with regards to the dosimetric errors observed in the experimental prototype.

Finally, it was shown that FRED is a suitable tool for virtually testing dosimeter improvements. Its merit function optimisation tools were used to make changes to the dosimeter geometry and these changes were found to improve the dosimeter's response to the main sources of environmental uncertainty.

It is therefore indicated that FRED is a suitable candidate for virtual refinement of the prototype dosimeter, and can be used to test the error response and sensitivity of new configurations before changes are made to the experimental prototype.

Acknowledgements

Enormous thanks to my wonderful supervisory team, Steve Marsh, Juergen Meyer, and Alicia Moggré for their constant availability, encouragement and support. Your help has been invaluable and I have learned so much from you. I would also like to acknowledge Jackson Roberts for his valuable contributions in data and advice in recent months.

Thanks to Roger Reeves for the loan of much appreciated real-estate in his laboratory and for the use of his equipment over the course of the project.

I would also like to thank Photon Engineering, without whose provision of a gratis software license, this research would not have been possible.

Contents

Chapter 1

Introduction

1.1 Motivation

1.1.1 Cancer Epidemiology

Cancer is an umbrella term for over 100 specific disorders characterised by abnormal cell growth with the potential to spread and invade other locations in the body. This stands in contrast to benign cell growth disorders which cause tumours but do not spread invasively. Fundamentally, cancer is the breakdown of biological mechanisms designed to regulate tissue growth [1]. Although different cancers are the result of different sets of mutations, in general cancer results from mutations in two sets of genes; oncogenes, which promote cell growth and reproduction, and tumour suppressor genes, which inhibit the survival and division of cells. Typically, a single change is insufficient to transform an ordinary cell into a cancer cell; multiple genetic errors must occur in a certain order to yield a malignant neoplasm.

Genetic changes which result in cancer are usually the result of mutations, which can happen a number of ways. Spontaneous mutations may occur during cell division, even in perfectly healthy cells, resulting in a daughter cell with an imperfect copy of the parent cell's DNA. DNA molecules also experience regular structural damage and degradation, even in healthy individuals unexposed to mutagens. In humans, an average of tens of thousands of DNA damage events occur per day in every cell due to reactive molecules produced by metabolism and other chemical reactions [2]. These events are most often repaired through cellular processes, but errors can persist past these corrections, especially if the repair processes are overloaded by too many errors or otherwise compromised. Exposure to environmental mutagens such as radiation or certain chemicals can cause a higher rate of

mutation, or more deleterious mutations, overloading repair structures [3]. A recent Science study exploring the origin of carcinogenic mutations found that 66% of the studied mutations occurred randomly, 29% were due to environmental factors and 5% were hereditary [4].

The statistical nature of mutation and DNA repair failure makes contracting cancer an event with a finite non-zero probability. Older individuals' tissues have undergone more cell division events and more genetic damage. In general, older tissues have therefore experienced more total mutations. It follows that as an individual ages, their chances of contracting a malignant neoplasm increase steadily [5]. As a result, the disease burden of cancer has increased in recent history, particularly in nations where medical and lifestyle advances have resulted in longer lifespans. New Zealand is an example of such a country, where life expectancy has increased by a decade in the last half-century, from 71 years in 1960 to 81 years in 2016 [6]. This increase in life expectancy was accompanied by an increasing rate of registrations for new cancers, as illustrated in Figure 1.1. New cancer registrations increased steadily from 4087 in 1960 to 23,149 in 2015, the date of last official record [7]. Cancer is now also a leading cause of death in New Zealand, with death from cancer accounting for 30% of all deaths in 2014 [8, 9]. As our population ages and life expectancy continues to increase, we can expect consistently increasing rates of new cancer registrations [10].

Although cancer registration rates have increased over time, many cancers have become more survivable. Developments in scientific understanding of the cause and mechanisms of cancer have led to more targeted and sophisticated treatments, which in turn increase the likelihood of a favourable long-term prognosis. In particular, more common cancers, such as those of the breast and prostate, have particularly good survival rates over time [11]. Continued innovation in diagnosis and treatment is needed to ensure positive patient outcomes and successfully handle what is likely to be an increasing incidence of cancer in the coming years as our population ages and other causes of death tend downwards [12].

1.1.2 Radiation Therapy And Dosimetry

There are currently three leading techniques employed to treat cancer: surgical excision, chemotherapy and radiation therapy, with immunotherapy

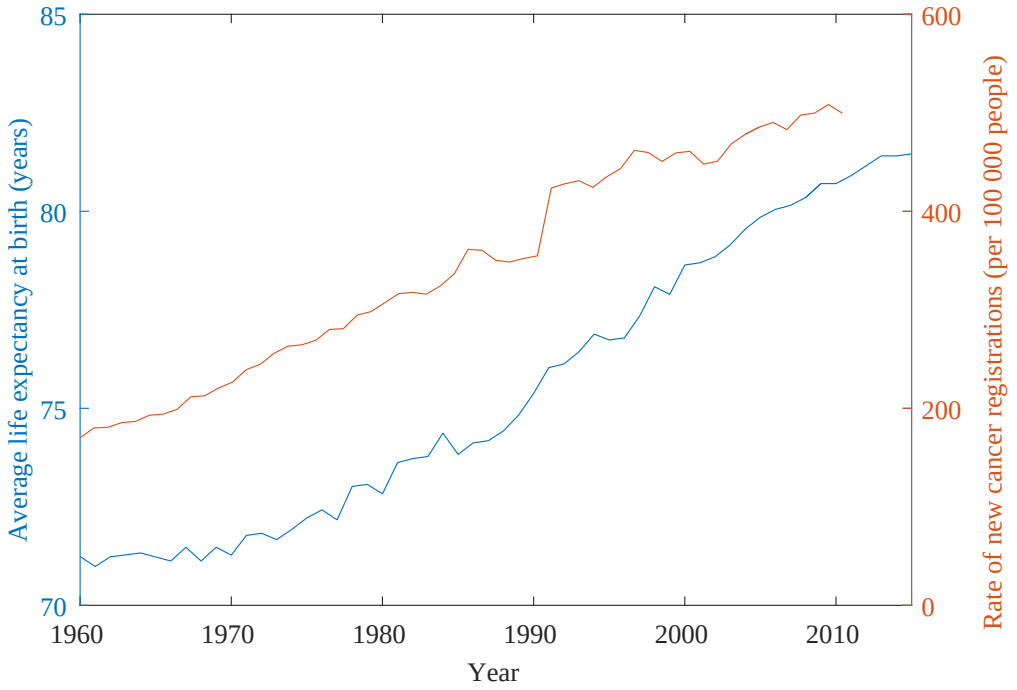

FIGURE 1.1: Graph showing the correlation between increase in life expectancy in New Zealand (bottom, blue line) [6] and increase in rate of cancer registrations (top, orange line) [8].

emerging as a potential fourth pillar [13]. The focus of this research is radiation therapy, which encompasses any technique using ionizing radiation to kill and control malignant cells. Radiation therapy can be used on its own or in concert with surgery or chemotherapy to maximise control of tumour cells [14].

Ionising radiation comes in several forms: photon, subatomic particle or ion, with the common characteristic that they have enough energy to liberate electrons, thereby creating atomic or molecular ions. When applied to biological tissues, these ionisation events occur inside cells, causing general cellular damage, DNA breakage, and cell death [15]. The degree of these deleterious effects is dependent on the amount of radiation energy absorbed per mass of tissue (the dose), and the susceptibility of the particular tissue to radiation damage, referred to as the radiosensitivity. Formally, the dose deposition of a radiation beam or source is often referred to in terms of absorbed dose in Gray (Gy), where

$$1Gy = 1Jkg^{-1}. \tag{1.1}$$

The radiosensitivity of tissue is more complex, and is dependent on the

type and energy of the radiation, as well as the type of tissue being investigated. In general, for a type of radiation, each tissue is assigned a relative biological effectiveness (RBE) which multiplies the dose received by the relative biological impact of the dose [15]. Other factors including tissue oxygenation and the selection of a biological endpoint to measure RBE further complicate the assessment of tissue radiosensitivity [16]. The power of radiotherapy in treating cancer stems from the fact that many neoplasms exhibit high radiosensitivity, meaning that they are more susceptible to ionising radiation than the tissues which surround them [17].

Radiation therapy is thus a balancing act between controlling tumour cells by applying high doses of radiation, and minimising complications related to irradiation of the healthy tissues surrounding the tumour. This balance is typically visualised by dose-response curves which show the probability of controlling the tumour versus the probability of compromising healthy tissues. Figure 1.2 shows the contrasting dose-response curve pairs for a radiocurable cancer versus a less curable cancer. In the left-hand graph, the curve representing tumour control probability (TCP) sits at a lower dose than the curve representing normal tissue complication probability (NTCP), yielding a larger dose window where a high probability of tumour control can be achieved with low probability for tissue complication. In contrast, the graph on the right represents a neoplasm with less relative susceptibility compared to surrounding tissues. A dose which achieves a high probability of tumour control is associated with a higher risk of normal tissue complications in this case, so either the dose must be delivered with extreme precision, or a different treatment method must be utilised.

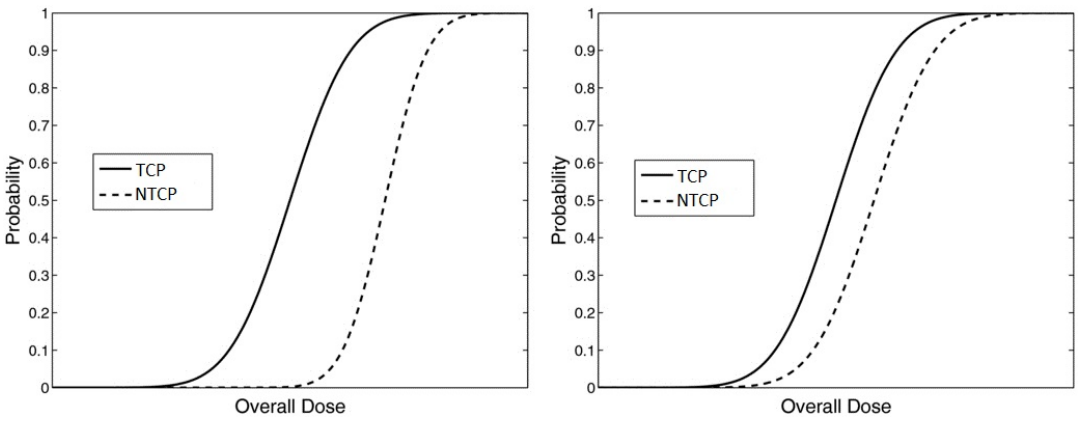

FIGURE 1.2: Comparison between the tumour control probability, TCP, and normal tissue complication probability, NTCP, curves for a more radiocurable cancer (left) and a less radiocurable cancer (right) [18].

Examination of the TCP and NTCP probability curves shows that even a small uncertainty in delivered dose can have a large associated increase in risk to the patient, depending on their gradient about the dose being delivered. This emphasises the need for accurate dosimetry in radiotherapy; correct dose delivery is essential to ensure positive patient outcomes. The requirements for dosimetric accuracy are established by the International Atomic Energy Agency (IAEA), which mandates an uncertainty cap of 5% for therapeutic radiation doses [19], and the International Commission on Radiation Units and Measurements (ICRU) which mandates that doses be delivered within +7% or -5% of their prescribed values [20, 21]. Compounding uncertainties in patient positioning, geometry, and biological response mean that dosimetric uncertainties should be kept as low as possible in order to minimise risk to patients. The design of any dosimeter must therefore make consideration of associated uncertainties in order to be clinically viable.

The minimisation of dosimetric uncertainty in radiation therapy is complicated by the steady forward progress of radiotherapy techniques. Current dosimetric methodology is entirely adequate for more conventional radiotherapy techniques, involving flat or simply-modulated radiation fields, which are generally low in dose rate and well-behaved over time. However a plethora of new radiotherapy modalities have been introduced in recent decades, each of which pose unique difficulties. Some techniques employ radiation fields with a high degree of spatial modulation, removing them from the paradigm of charged particle equilibrium used to calculate the dose of well-behaved flat fields [22]. In other cases, the use of heavier particles such as protons or ionic nuclei result in a new characteristic dose-delivery profile and uncertainties in the range and RBE of these less-investigated radiation types [23]. In yet other cases, some novel treatment modalities deliver extremely high or extremely low doses, or, in the case of flash-irradiation techniques, deliver doses at extremely high rates [24]. All of these non-standard irradiation practices can result in less-well quantified radiobiological effects. In such scenarios, radiotherapy modalities push the boundaries of the models used in current dosimetric techniques, necessitating the use of additional conversion or correction factors, all of which have their own associated uncertainties. Research into new dosimetric technology must therefore keep pace with the progression of radiation therapy so that dosimetric uncertainties can be kept as low as possible.

1.1.3 Prototype Dosimeter

The development of a new dosimetry technology is the aim of our research group, which began with the work of Juergen Meyer and Alicia Cavan [25, 26]. Over the course of the latter's doctoral research, a novel radiation dosimeter was produced which operated on the principles of Digital Holographic Interferometry (DHI). The fundamentals and physics underlying this dosimeter are discussed in full in Section 2.4. In brief, the dosimeter directly measures absorbed radiation dose to water by probing a water-filled test cell with a laser, then interfering this beam with a reference laser field. By capturing the interference pattern twice, once before and once after irradiation, the differences between the two can be related to the change in refractive index across the test cell. This refractive index change can then be used to infer a spatial map of change in temperature, or energy deposited. By capturing the interference pattern repeatedly over the course of irradiation, a series of 2-D spatial maps can be reconstructed, allowing for the calculation of dose deposited over time.

This prototype dosimeter performed well as a proof-of-concept, measuring spatially modulated patterns of incident radiation produced with three different complex radiotherapy modalities. However, experimental uncertainties were high, with a best case estimate of 15%, and over the course of testing several areas for improvement were identified [26]. The dosimeter was built with re-purposed optical components on a large, heavy breadboard, making it difficult to transport and susceptible to environmental fluctuations. To improve this, specialised optical components can be purpose built in order to miniaturise and stabilise the dosimeter. In collaboration with the University of Washington, the possibility exists of using microelectromachine systems (MEMS) technology to replace our standard optical components and miniaturise the dosimeter. However, due to the expense of purchasing new components and commissioning the MEMS components, it was deemed prudent to refine the dosimeter in a virtual environment using optical simulation software before attempting to build a new iteration of the prototype.

Although optical modelling software has been implemented successfully in a wide range of applications, including laser interference [27], coherent diffraction effects [28] and holography [29], there exists no current precedent for using commercial optical modelling packages to simulate interferometry

for radiation dosimetry. Therefore, establishing that the optical modelling program FRED is capable of reproducing the results observed over the course of Cavan's investigations will be an important aim of this thesis.

1.2 Thesis Aims

The aim of this thesis was to verify that the FRED optical modelling program was capable of accurately simulating our interferometric dosimeter, including sources of uncertainty, so that the model could be used to virtually improve the prototype.

It is important to note that due to the time constraints posed by an MSc, the aim of this thesis was confined to creating the DHI dosimeter model and developing algorithms for reconstructing its output, developing a protocol for characterising the dosimeter's spatial and dose resolution, and showing whether FRED was a suitable tool to conduct further refinements upon the prototype. Conducting a full uncertainty analysis and completely refining the prototype are outside the scope of this thesis, and these goals are left for future research.

1.3 Thesis Outline

This chapter serves to outline the motivation and basic aims of this research. Chapter 2 outlines the theoretical and historical background behind the use of digital holographic interferometry for radiation dosimetry. Chapter 3 covers the mathematical principles and computational methods which underpin optical simulations conducted in FRED. Chapter 4 describes the experimental procedure of initialising the model of our prototype dosimeter, from early tests on FRED's coherence handling to the full DHI dosimeter model. Chapter 5 outlines the methods used to conduct case studies into the dosimetric uncertainties of the prototype model. Chapter 6 describes the procedure used to model two proposed geometric improvements to the prototype, and quantifies their impact on dosimetric uncertainty. Chapter 7 discusses the results of these case studies and outlines the advantages and disadvantages of FRED as a candidate for modelling the prototype. Finally, Chapter 8 concludes the work.

Chapter 2

Principles of Digital Holographic Interferometric Dosimetry

2.1 Fundamentals of Light

Light has been studied extensively for centuries, but to this day there is no unified model which explains all of its behaviours. Instead, two paradigms, the classical and quantum models, are used to explain different phenomena and aspects of optics.

The classical model was developed in the 19th century as a result of the discovery of electromagnetism and the interference experiments conducted by Fresnel [30], Young [31], and many others. James Maxwell is generally credited with codifying the classical model of light in his 1865 paper which unified the leading optical observations of his time with the nascent theory of electromagnetism [32]. This model treats light as a wave, and explains interference phenomena as the superposition of the amplitudes of interacting wavefronts.

The next major development in optics was made at the turn of the 20th century, when Max Planck modelled black-body radiation and found that matter contributed energy to light only in discrete amounts, a fact that was unexplained by the classical electromagnetic model of light [33]. Compounded by Einstein's 1905 writings on the photoelectric effect, it catalysed the development of Bohr's atomic model which eventually led to the establishment of quantum physics as a field [34]. As part of the discovery of quantum mechanics, these optical phenomena were explained by treating light as a current of massless particles called photons. This model was initially explored and unified by Dirac, Schrödinger and their

contemporaries in the 1920s [35, 36]. On the back of developments made by Bethe in 1947 [37], it eventually developed into quantum electrodynamics in the late 40s and early 50s [38].

Although the quantum model of light is technically more complete, many macroscopic optical phenomena can be fully explained in a much simpler manner via the classical electromagnetic model. For holography and the measurement of refractive index in transparent media, the classical model is an accurate and elegant treatment, so the electromagnetic wave formalism will be used exclusively from this point onward.

2.1.1 Propagation of Light as an Electromagnetic Wave

The classical model treats light as an electromagnetic wave, which means that by definition it propagates through space due to the synchronised oscillations of coupled electric and magnetic fields. As an electromagnetic wave, light obeys Maxwell's equations, which means that its propagation is governed by the wave equation

$$\nabla^2 \mathbf{E} - \frac{1}{c^2}\frac{\partial^2 E}{\partial t^2} = 0\,, \tag{2.1}$$

where ∇^2 is the Laplace operator acting on the Cartesian spatial coordinate vector $\mathbf{r} = (x, y, z)$:

$$\nabla^2 = \frac{\partial^2}{\partial x^2} + \frac{\partial^2}{\partial y^2} + \frac{\partial^2}{\partial z^2}\,, \tag{2.2}$$

$\mathbf{E}$ is the vector quantity describing electric field strength, and c is the speed of light, equal to roughly $3 \times 10^8\,\mathrm{m\,s^{-1}}$.

By the definition of an electromagnetic wave, the electric and magnetic fields oscillate orthogonal to one another and to the direction of propagation. The electric field can oscillate in the vertical, horizontal or any linear combination of these directions. The oscillation direction can also evolve over time, resulting in elliptically or circularly polarised light. Differences in polarisation types are illustrated in Figure 2.1. For holography applications, polarisation effects can be ignored, and we will treat light from now on as linearly polarised unless stated otherwise.

A linearly polarised wave is also called plane-polarised. For waves of this nature propagating along the z axis in Cartesian spatial coordinates, instead

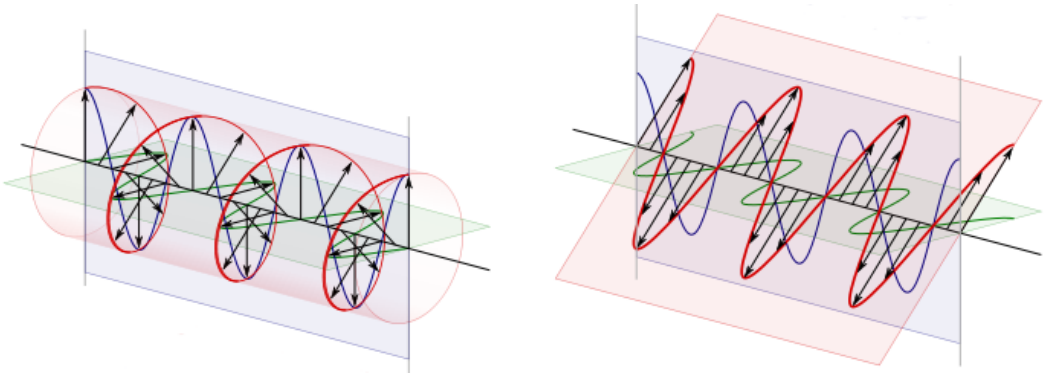

(a) Circularly polarised light. (b) Linearly polarised light.

FIGURE 2.1: Illustration of the evolution of the electric field vector in light with different polarisations [39].

of the vector wave equation used above, we can substitute the scalar wave equation:

$$\frac{\partial^2 E}{\partial z^2} - \frac{1}{c}\frac{\partial^2 E}{\partial t^2} = 0. \tag{2.3}$$

The most widely used solution to the scalar wave equation is the harmonic wave, given by

$$E(z,t) = E_0 \cos(kz - \omega t), \tag{2.4}$$

where E_0 is the real amplitude of the wave and the cosine term $kz - \omega t$ gives the phase, where the wavenumber k is directly related to the wavelength of the light by:

$$k = \frac{2\pi}{\lambda}. \tag{2.5}$$

Similarly, ω is the angular frequency of the wave, also related to the wavelength of the light via:

$$\omega = \frac{2\pi c}{\lambda}. \tag{2.6}$$

In order to account for a phase shift, where the maximum amplitude does not correspond to the zero-time point, we can add the phase offset (ϕ) to the cosine term, modifying the harmonic wave equation to:

$$E(z,t) = E_0 \cos(kz - \omega t + \phi). \tag{2.7}$$

Using Euler's identity, we can rewrite this complete harmonic wave equation in complex notation:

$$E(z,t) = \frac{1}{2}E_0 e^{i(kz-\omega t+\phi)} + \frac{1}{2}E_0 e^{-i(kz-\omega t+\phi)}. \tag{2.8}$$

The physical aspects of the wave field are fully represented by the first term in this equation, and the second term is its complex conjugate. We can therefore simplify the complex harmonic solution propagating in the z-direction to its real component as follows:

$$E(z,t) = \frac{1}{2}E_0 e^{i(kz-\omega t+\phi)}. \tag{2.9}$$

Therefore, Equation 2.9 describes the evolution of the electric field over space and time. If we consider the evolution in space with the wave frozen in time, the electric field amplitude varies sinusoidally, with the maximum amplitude values of E_0 occurring at integer multiples of λ along the propagation direction. Similarly, if we consider the wave evolution in time at a fixed point in space, the maximum field value is achieved at time $t = 0 + \phi$, and subsequent maxima occur at every integer multiple of the wave's period T, where $T = {}^{\lambda}/_{c}$ given that the propagation occurs in a vacuum.

2.1.2 Wavefront Geometry

Equation 2.9 describes the simplest case of a linearly-polarised sinusoidal wave propagating in the z-direction. For optics applications, the three-dimensional geometry of the propagation must be accounted for. It is characterised as the wavefront of the light, which describes the shape of the surfaces of constant phase in a propagating wave in three dimensions. In practical applications, the wavefront geometry is initially determined by the type and geometry of the source which generated the light, and is further modified by the use of optics to direct and shape the propagating wave field. This research makes use of beams with two wavefront geometries: planar and spherical.

A planar wavefront is characterised by each plane orthogonal to the propagation direction of the wave having constant phase. For a plane wave, the

product of the wave vector, **k**, and the spatial vector, **r**, is a constant:

$$\mathbf{k} \cdot \mathbf{r} = constant. \tag{2.10}$$

The wave vector ($\mathbf{k} = (k_x, k_y, k_z)$) is the 3-D equivalent of the wavenumber described in Equation 2.5 to account for propagation away from the z-axis. Similarly, the spatial vector is simply the Cartesian coordinate vector $\mathbf{r} = (x, y, z)$. The harmonic solution for a plane-propagating wave is

$$E(\mathbf{r}, t) = E_0 e^{i(\mathbf{k}\cdot\mathbf{r} - \omega t + \phi)}. \tag{2.11}$$

Spherical waves are easily visualised as light generated from a point source, and also result from light being modified by spherical optics. Spherical wavefronts are more intuitively modelled in spherical coordinates, (r, θ, ψ), where the wave equation becomes

$$\frac{1}{r}\frac{\partial^2}{\partial r^2}(rE) - \frac{1}{c^2}\frac{\partial^2 E}{\partial t^2} = 0 \tag{2.12}$$

and the harmonic spherical solution is

$$E(r, t) = \frac{E_0}{r} e^{i(kr - \omega t + \phi)}. \tag{2.13}$$

Equations 2.11 and 2.13 describe the two propagation geometries which are most frequently used in this thesis.

2.1.3 Refractive Index and Speed of Light

The above exclusively considers light that is propagating in a vacuum. Light propagates in a similar way in other transparent media, but its speed changes depending on the medium, an effect which is quantified by the refractive index (n) of the medium, as given by the identity

$$n = \frac{c}{v}, \tag{2.14}$$

where c and v represent the speed of light in a vacuum and in the given medium respectively. Figure 2.2 illustrates that when light traverses a boundary between two materials of different refractive indices, n_1 and n_2, its velocity will change in accordance with Equation 2.14, and its angle from the

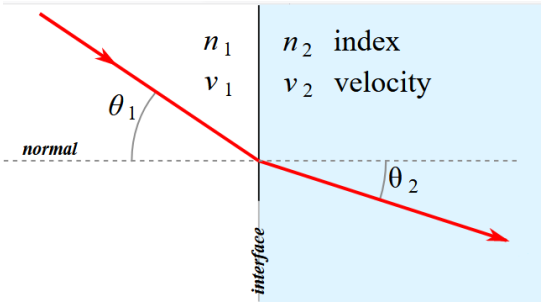

FIGURE 2.2: Illustration of Snell's law at a refractive index interface [40].

normal will change from θ_1 to θ_2 as per Snell's law, given by

$$n_1 \sin(\theta_1) = n_2 \sin(\theta_2). \tag{2.15}$$

The change in speed undergone by light in a medium results in a change of phase relative to an identical light wave propagating in the vacuum, or a medium with a different refractive index. This is quantified in terms of the optical path length (OPL) given by

$$OPL = nd, \tag{2.16}$$

where n is the refractive index of the medium and d is the distance traversed in the medium. Where refractive index varies across the medium, the integral version of this law applies. This is given by

$$OPL = \int_C n(s)ds, \tag{2.17}$$

where C is the path travelled by the light, and $n(s)$ is the refractive index over the distance s along the light's path.

On a microscopic level, the refractive index of a medium describes the degree to which the atomic and electronic charges in the material perturb the electric field of a light wave, reducing its propagation velocity. Therefore, any change to the medium that alters the distribution of its internal electric charges has the potential to change the medium's refractive index. Light waves of different wavelengths also experience different perturbations, so the refractive index of a material varies according to the wavelength used to measure it.

2.1.4 Interference

Laser interferometry is based on electromagnetic wave interference, the principle which underpins the classical model of light. Interference is based on the superposition principle which states that the sum of solutions to the wave equation is also a solution, and electromagnetic fields co-incident in space will superimpose to create a new electromagnetic field which has an amplitude distribution equal to the sum of the two amplitudes at every point.

For the purposes of laser interferometry, we can assume that the interfering wave fields have the same frequency. As a case study, we can examine two plane waves of the same frequency:

$$\mathbf{E_1}(\mathbf{r},\mathbf{t}) = \mathbf{E_{01}} e^{i(\mathbf{k_1}\cdot\mathbf{r}-\omega t+\phi_1)} \tag{2.18}$$

and

$$\mathbf{E_2}(\mathbf{r},\mathbf{t}) = \mathbf{E_{02}} e^{i(\mathbf{k_2}\cdot\mathbf{r}-\omega t+\phi_2)}. \tag{2.19}$$

The resultant electric field due to the interference of the two electromagnetic waves is then given by their sum:

$$E_{total} = E_1 + E_2 = [E_{01} e^{i(\mathbf{k_1}\cdot\mathbf{r}+\phi_1)} + E_{02} e^{i(\mathbf{k_2}\cdot\mathbf{r}+\phi_2)}] e^{-i\omega t}. \tag{2.20}$$

It is important to note that optical detectors, from cameras to the human eye, do not measure the field amplitude of an electromagnetic wave. Instead, they measure optical intensity, which is defined as the energy flux through an area per unit time. Optical intensity is defined as:

$$I = \epsilon_0 c n E^2, \tag{2.21}$$

where ϵ_0 is the permittivity of free space, c is the speed of light in a vacuum, and n is the refractive index of the medium in which the light is travelling.

A common simplification in optics applications is to leave out the proportionality constants and express intensity only in terms of the electric field, such that:

$$I = |E_0|^2 = \langle E_0 \rangle \langle E_0^* \rangle . \tag{2.22}$$

When we consider the interference pattern yielded by the interfering plane waves described by Equation 2.20, the intensity distribution will be:

$$\begin{aligned} I(\mathbf{r},t) =& (E_{01}e^{i(\mathbf{k_1}\cdot\mathbf{r}-\omega t+\phi_1)} + E_{02}e^{i(\mathbf{k_2}\cdot\mathbf{r}-\omega t+\phi_2)}) \times (E_{01}e^{-i(\mathbf{k_1}\cdot\mathbf{r}-\omega t+\phi_1)} \\ &+ E_{02}e^{-i(\mathbf{k_2}\cdot\mathbf{r}-\omega t+\phi_2)}) \\ =& E_{01}^2 + E_{02}^2 + E_{01}E_{02}\{e^{i(\mathbf{k_1}\cdot\mathbf{r}-\mathbf{k_2}\cdot\mathbf{r}+\phi_1-\phi_2)} + e^{i(\mathbf{k_2}\cdot\mathbf{r}-\mathbf{k_1}\cdot\mathbf{r}+\phi_2-\phi_1)}\} \\ =& E_{01}^2 + E_{02}^2 + 2E_{01}E_{02}\cos\left((\mathbf{k_1}-\mathbf{k_2})\cdot\mathbf{r}+2\Delta\phi\right). \end{aligned} \tag{2.23}$$

This result can be written in terms of the individual intensities:

$$I = I_1 + I_2 + 2\sqrt{I_1 I_2}\cos((\mathbf{k_1}-\mathbf{k_2})\cdot\mathbf{r}+2\Delta\phi). \tag{2.24}$$

In the case that the interfering waves have equal amplitude ($E_{01} = E_{02} = E_0$), Equation 2.23 becomes

$$I(\mathbf{r}) = 4E_0^2\cos^2\left(\left(\frac{\mathbf{k_1}-\mathbf{k_2}}{2}\right)\cdot\mathbf{r}+\Delta\phi\right). \tag{2.25}$$

For two waves of equal amplitude, it can be seen that the intensity map has the widest dynamic range, from 0 to $4E_0^2$. As the interfering waves' intensities become more different, the contrast (C) of the interference pattern becomes smaller, where the formula

$$C = \frac{I_{max}-I_{min}}{I_{max}+I_{min}} \tag{2.26}$$

quantifies the degree of contrast in the interference pattern.

2.2 Interferometry

Interferometry refers to a family of metrology techniques which use interference phenomena to measure physical parameters of a system. Interferometry is used in a wide range of fields due to its ability to make extremely high-precision measurements [41]. This ability stems from the fact that interference patterns are sensitive to sub-wavelength changes between the interfering waves, meaning that displacements on the order of nanometres can be measured with optical frequencies.

2.2.1 History and Applications

Interferometry was first used for metrology by Albert Michelson and Edward Morley in 1887. They used a right-angle interferometer in an attempt to measure the aether wind created by the relative speed between Earth and the luminiferous aether, the medium through which electromagnetic waves were thought to propagate at the time [42]. Although this experiment failed, leading to the popular move away from aether theory of electromagnetism, the potential of interferometry as an extremely sensitive metrology technique was recognised at this time, and the experiment was repeated with increasingly sensitive interferometers [43]. Michelson went on to design interferometric instruments for astronomy applications, and interferometers were widely adopted in many fields of physics by the mid 20th century [44].

Interferometry is used today in any field which requires measurement of small changes in a physical quantity which affects the path length of light [45, 46, 47]. It is especially valuable in areas of metrology where extreme precision is required, since its ability to encode information as a change in path length of light makes it sensitive to changes on the order of whatever wavelength is used.

An important metrological example is the use of test-plate interferometry to measure deformation constants and moduli in material science. This technique involves a reference plate and test surface being placed together under coherent illumination by a laser, where a reference interference pattern is acquired. The test object is then deformed by a known force in a manner consistent with the modulus being measured and an interference pattern is acquired for this state. The difference between these patterns is processed to yield a displacement measurement, which can then be used to quantify the modulus of deformation for the given material [48].

A similar application also occurs in quality assurance and manufacturing, where test-plate interferometers probe the uniformity of surfaces by interferometric comparison with a flat reference surface [49].

Refractive Index Determination in Transparent Media

For the purposes of this research, the measurement of refractive index in transparent media is the most relevant application of interferometry. A

schematic of a Mach-Zehnder interferometer configured for this purpose is shown in Figure 2.3

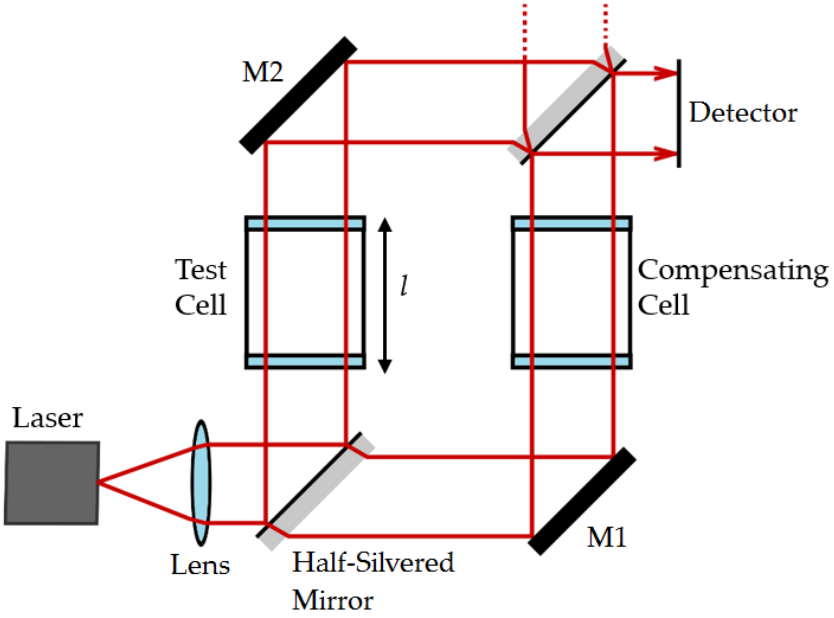

FIGURE 2.3: Mach-Zehnder interferometer configured for the measurement of refractive index. M1 and M2 are turning mirrors. l is the optical path length of the test cell.

In this experiment, the object beam passes through a test cell which contains the medium being probed. The reference beam passes through an identical cell in order to negate its geometrical effects. With the test cell empty, a reference interference pattern is collected on the detector. Upon introduction of a sample with unknown refractive index (n), the interference pattern will change due to the phase shift induced in the object beam along the length (l) of the test cell. Mathematical processing is then employed to quantify the change and measure the optical path length difference induced in the object beam by the sample. With a known optical path length difference, ΔOPL, the refractive index of the sample can then be calculated via Equation 2.16.

This technique has also been employed in substances with known refractive indices to measure complex phenomena. These interferometry techniques have been used to gather high-resolution spatial data in order to more accurately model heat diffusion from chaotic sources like flames [50], the fluid dynamics of mixing liquids [51], and problems of air-turbulence and non-laminar fluid flow [52].

2.2.2 Holographic Wavefront Recording

History and Early Application

Holography was pioneered by Dennis Gabor in 1948, as an extension of his work on optimising electron microscopes [53]. Prior to this discovery, conventional photographic techniques were capable only of recording a two-dimensional cross-section of the wave field reflected or radiated from an object. Contrastingly, holography interferes the object's wave field with that of another beam and records the interference pattern, allowing a full three-dimensional reconstruction of the wave field to be obtained upon reconstruction using the same reference field [54, 55]. At the time of its invention, holography was highly limited by the lack of coherent optical sources. This changed in 1960, when Maiman et al. constructed the first working ruby laser [56], providing a high-power coherent optical source with which to encode the hologram. This allowed for the creation of higher-fidelity holographic recordings, which could be reliably reconstructed into three-dimensional images [57].

Other technological limitations also hampered early experiments. Initially, fringes were counted and their spacing was measured manually by researchers, which limited the precision of quantitative measurements [41]. Holographic interferometry of the 1960s relied upon the exposure of analogue silver halide plates, which limited the temporal resolution of the measurements and were inefficient at converting the incident intensity to optical density [58]. Fringe-counting computers were later employed, but their use required the analogue plates to be digitised via camera after their initial exposure, which was a laborious process [59]. These limitations eventually led to the development of modern digital holography, which forms the foundation of this research and will be discussed in Section 2.3 below.

Principles of Hologram Acquisition

There are a variety of techniques for recording holograms, each of which has a distinct experimental configuration and underlying imaging equations. For expediency, the equations of holography will be discussed in terms of the Lensless Fourier Transform Digital Holography (LFTDH) interferometer,

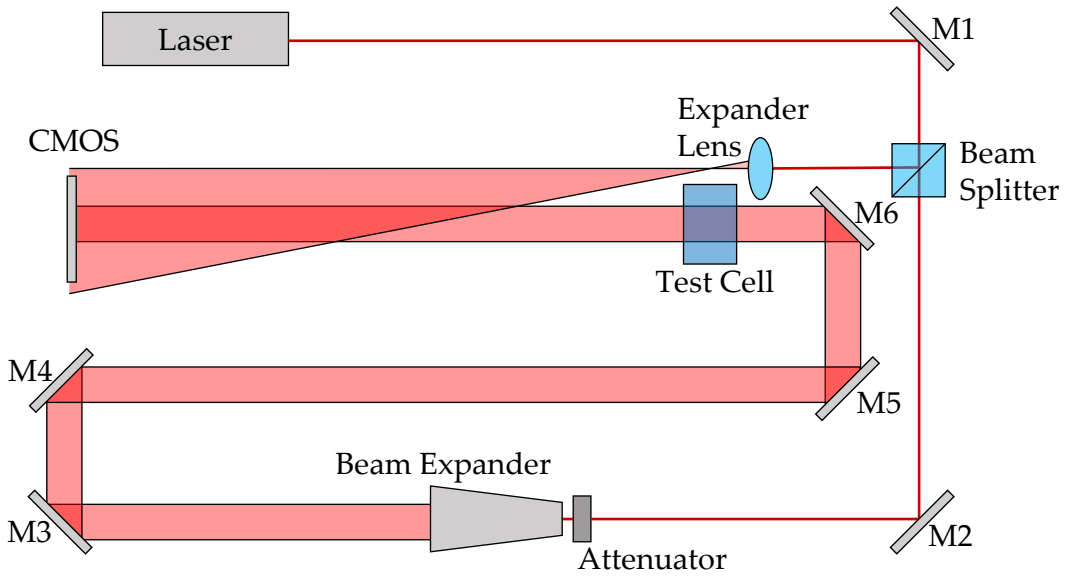

FIGURE 2.4: Schematic of the simple LFTDH interferometer used in this research.

since this is the configuration employed in our prototype dosimeter. However, it is important to note that this is neither the simplest nor the most common holographic imaging configuration.

Figure 2.4 shows a schematic of the LFTDH configuration used in this research. The laser source is separated via a beamsplitter into two coherent beams. The reference beam is expanded via a spherical lens and then bypasses the test cell to fall on the complimentary metal oxide semiconductor (CMOS) detector chip. The object beam is expanded and collimated to approximate a plane wave and then passes through the test cell, where its geometric path length is modified by the refractive index of the test cell according to Equation 2.16. The object beam then interferes with the reference beam where they coincide on the CMOS.

Recalling Equations 2.11 and 2.13 from Section 2.1, it can be seen that the time-dependent electric fields of the reference (E_R) and object (E_O) beams are of the forms:

$$E_R(r,t) = \frac{E_{0R}}{r} e^{i(k_R r - \omega_R t + \phi_R)}, \tag{2.27}$$

and

$$E_O(\mathbf{r},t) = E_{0O}\, e^{i(\mathbf{k_O}\cdot\mathbf{r} - \omega_O t + \phi_O)} \tag{2.28}$$

respectively. The CMOS detector chip will therefore detect a pattern of interference fringes given by

$$\begin{aligned}
I =& |E_O + E_R|^2 \\
I =& E_O E_O^* + E_R E_R^* + E_O^* E_R + E_O E_R^* \\
=& E_{0O}^2 + \frac{E_{0R}^2}{r^2} + E_{0O} e^{-i(\mathbf{k_O}\cdot\mathbf{r} - \omega_O t + \phi_O)} \frac{E_{0R}}{r} e^{i(k_R r - \omega_R t + \phi_R)} \\
&+ E_{0O} e^{i(\mathbf{k_O}\cdot\mathbf{r} - \omega_O t + \phi_O)} \frac{E_{0R}}{r} e^{-i(k_R r - \omega_R t + \phi_R)} \\
=& E_{0O}^2 + \frac{E_{0R}^2}{r^2} + E_{0O}\frac{E_{0R}}{r}\Big(e^{-i(\mathbf{k_O}\cdot\mathbf{r} - \omega_O t + \phi_O)} e^{i(k_R r - \omega_R t + \phi_R)} \\
&+ e^{i(\mathbf{k_O}\cdot\mathbf{r} - \omega_O t + \phi_O)} e^{-i(k_R r - \omega_R t + \phi_R)}\Big) \\
=& E_{0O}^2 + \frac{E_{0R}^2}{r^2} + 2E_{0O}\frac{E_{0R}}{r}\cos(\mathbf{k_O}\cdot\mathbf{r} - \omega_O t + \phi_O - k_R r + \omega_R t - \phi_R).
\end{aligned} \tag{2.29}$$

From the above, we can see that the temporal dependence of this interference pattern is exclusively described by the terms $-\omega_O t$ and $\omega_R t$ inside the cosine operator. By the definition of angular frequency ($\omega = 2\pi\nu$), if the interfering waves share the same frequency, as they do in the case of our laser interferometer, then $\omega_O = \omega_R$ and these terms cancel, yielding

$$\begin{aligned}
I &= E_{0O}^2 + \frac{E_{0R}^2}{r^2} + 2E_{0O}\frac{E_{0R}}{r}\cos(\mathbf{k_O}\cdot\mathbf{r} - k_R r + \phi_O - \phi_R) \\
&= E_{0O}^2 + \frac{E_{0R}^2}{r^2} + 2E_{0O}\frac{E_{0R}}{r}\cos(\mathbf{k_O}\cdot\mathbf{r} - k_R r + \Delta\phi)
\end{aligned} \tag{2.30}$$

which describes a temporally stable interference pattern, given that the phase difference ($\Delta\phi$) is also constant.

A temporally constant interference pattern is necessary for holographic recording, since a fluctuating intensity on the CMOS would cause blurring over the course of the hologram exposure, adding noise and potentially obscuring the signal in the reconstructed image. To meet the criteria of $\omega_O = \omega_R$, single frequency light must be used, and to ensure that $\Delta\phi$ is constant, the reference and object beams must be coherent. Using an amplitude-split laser to generate the reference and object beams meets both of these criteria.

The interference pattern captured by the CMOS can be recorded to produce a hologram, and this hologram can be reconstructed using the techniques described in the next section to create a three-dimensional copy of the object wavefront used to acquire it.

Principles of Hologram Reconstruction

In analogue holography, the object wave in the image plane, $O(x_I, y_I)$, can be reconstructed and viewed by re-illuminating the developed hologram plate with the reference beam. Mathematically, this re-illumination is equivalent to taking the product of the interference pattern, $I(x_H, y_H)$, and the reference wave, $R(x_H, y_H)$ in the plane of the hologram, denoted by the subscript H.

To obtain the object wave reconstruction, $O(x_I, y_I)$, from a given interference pattern, $I(x_H, y_H)$, recorded on a discrete pixel-based detector, a numerical variant of the Fresnel transform, developed for this purpose by Cavan and Meyer can be used [25]. Equation 2.31 is applied to the two-dimensional intensity map of the interferogram to calculate the reconstructed complex amplitude of the object wave, $O(x_I, y_I)$, in the image plane [26].

$$O(x_I, y_I) = B\frac{e^{ikd}}{i\lambda d}e^{[-i\frac{k}{2d}(x_I\Delta x)^2+(y_x\Delta y)^2]} * F_{\lambda d}^{-1} I(x_H, y_H) \tag{2.31}$$

In this equation, x_I and y_I are the indices of the detector pixels whose spacing is given by Δx and Δy. B is a constant dependent on the reference beam amplitude, d is the distance between the reference beam's focal point and the sensor plane, and $F_{\lambda d}^{-1}$ represents a discrete inverse Fourier transform scaled by $1/\lambda d$. Note that this variant of the Fresnel transform is specific to reconstructing the output of an LFTDH interferometer, as it relies on geometric factors for some of its simplifications.

The intensity of the resultant reconstructed object wave can be obtained by taking the modulus squared:

$$I(x_I, y_I) = |O(x_I, y_I)|^2 = Re^2|O(x_I, y_I)| + Im^2 O(x_I, y_I) \tag{2.32}$$

where the final two terms are the real and imaginary components of the complex field respectively. Similarly, a two-dimensional map of the phase angle can be obtained by taking the angle between these components

$$\phi(x_I, y_I) = \arctan\left(\frac{Im[O(x_I, y_I)]}{Re[O(x_I, y_I)]}\right) \tag{2.33}$$

It can be seen from Equation 2.31 that using a digital detector limits the spatial resolution of the reconstruction to the size of its pixels, Δx and Δy. However, digital detection eliminates the need for a development step and

reduces exposure time, thereby improving the temporal resolution of the holograms. Acquiring and reconstructing the holograms digitally also eliminates the need to remove and reposition a hologram plate, reducing error. The advantages afforded by replacing film with a digital detector therefore outweigh the slight loss of spatial resolution in almost every application.

2.3 Holographic Interferometry

The previous section introduced the concept of encoding three-dimensional spatial information in a two-dimensional hologram image. If a hologram is captured of an object twice in identical states, the two holograms will be identical. However, if a small deformation is applied to the object in between recording the first and second holograms, the interference pattern will be altered slightly due to the perturbation in the object beam's phase.

In the mid 1960s, it was discovered that if a reference hologram, $I_R(x,y)$, was recorded of a system in a reference state, and then an object hologram, $I_O(x,y)$, was exposed onto the same plate after the system had been perturbed, the resultant interference pattern could be reconstructed to yield the difference between the two states of the object [60]. Digitally, the same result can be achieved by recording separate reference and object interference patterns, reconstructing them using Equation 2.31 and then adding their reconstructed wavefronts digitally. The interference phase between these two object reconstructions can then be obtained via Equation 2.33, and the cyclic interference phase map can be unwrapped to a continuous distribution as follows:

$$\Delta\Phi(x_I,y_I) = \begin{cases} \Phi_R - \Phi_O & if \Phi_R \geq \Phi_O \\ \Phi_R - \Phi_O + 2\pi & if \Phi_R < \Phi_O, \end{cases} \tag{2.34}$$

where $\Delta\Phi$ represents the continuous two-dimensional phase difference map between the reference and object states. We call this map the interferogram, as it represents the amplitude of interference between the two hologram states. If we recall Equation 2.29, the intensity of this interference pattern has four terms. The first two represent the zero-order diffraction term of the object and reference wave fields, and contribute to the central bright component of the interferogram, the DC component. The third term adds the twin conjugate image, which is a pseudoscopic image appearing at a distance d past the hologram plane. Finally, the fourth term contributes the real image,

which is a non-pseudoscopic image of the test object which appears at the same position that the test object occupied during the hologram acquisition. Figure 2.5 shows an example of an experimentally acquired interferogram with these regions labelled.

The separation and size of each of these image regions is dependent upon the geometry of the interferometer. Placing the reference beam at a small angle to the object beam separates the image regions from the DC terms and one another in the image plane, which is necessary for straightforward extraction of the object wave phase map. The magnification of the image regions, and thus the resolution of the phase map of the real image, can also be modified by changing the object-to-sensor distance. These alignment procedures are discussed more fully in the experimental Section 4.2.3, which describes the alignment steps undertaken on our virtual LFTDH interferometer.

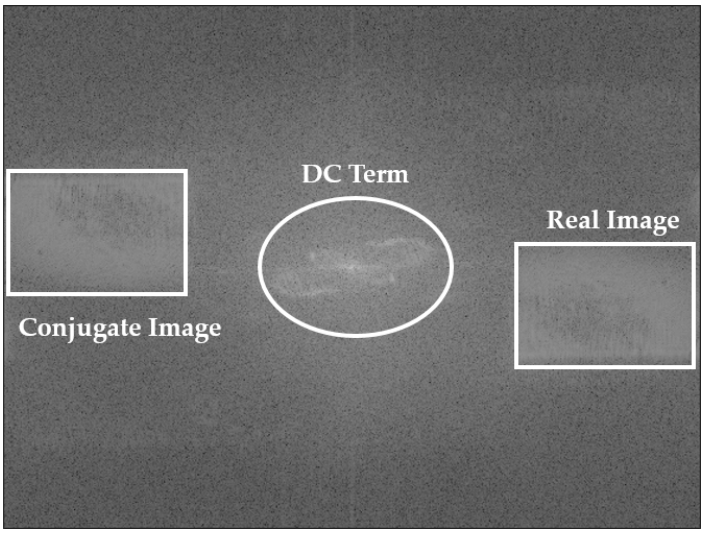

FIGURE 2.5: Example of a reconstructed interferogram.

2.3.1 DHI for Radiation Dosimetry

History of DHI Dosimetry

The use of holographic interferometry for radiation dosimetry was pioneered by E K Hussmann in 1971, when he used a Michelson-style interferometer to measure the fringe patterns from a water-filled cell under electron-beam irradiation [61]. Interference patterns from the un-irradiated state and the irradiated state were superimposed on a film plate and reconstructed via the process described above, yielding the interferogram shown in Figure 2.6a

which was subsequently reconstructed into an absorbed dose distribution, as shown in Figure 2.6b.

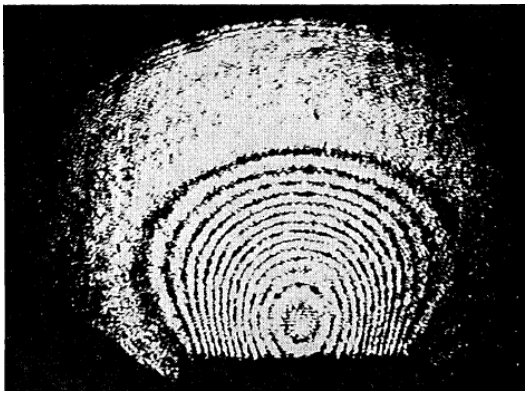

(a) Interferogram collected by Hussmann.

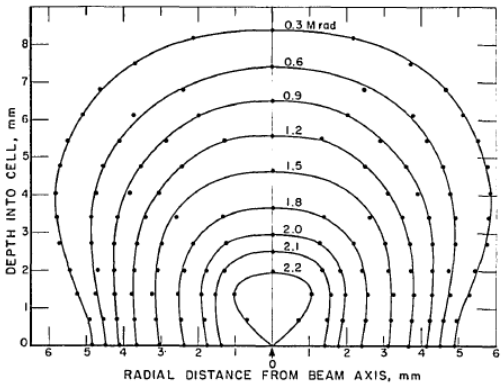

(b) Dose reconstructed by Hussmann.

FIGURE 2.6: Figures from Hussmann's early interferometry experiments in 1971 [61].

Following the success of the method for dose measurements, Hussmann continued work through the 1970s with Miller and McLaughlin, where the same calorimetric principles were adapted to measure fast refractive index and temperature changes in transparent media via the fringe shift in the interference pattern, rather than through holographic reconstruction [62]. Miller continued Hussmann's original dosimetric measurement work through 1979, improving on both the sensitivity and stability of the original dosimeter [63, 64].

Although the original Hussmann and Miller work represents a promising proof-of-concept of DHI as a radiation metrology technique, these experiments were hampered by the same factors which challenged all early interferometric experiments. The manual counting of fringes severely limited the accuracy of dose measurements, and confined the research to only simple dosimetric distributions. In addition, the double-exposure method used to capture interfering holograms on film severely limited the temporal resolution of the measurements.

As a result of these challenges, holographic interferometric radiation dosimetry went largely uninvestigated for several decades following the work of Hussmann, Miller and McLaughlin, although researchers periodically revisited the idea of a non-invasive calorimetric measuring technique in the same spirit [65, 66]. In the early 2010s, our research group, beginning with Cavan and Meyer chose to revisit holographic interferometry for

radiation dosimetry [25]. Their aim was to replicate the results of Hussmann and Miller, replacing their analogue approach with digital detection so that interferograms could be reconstructed and analysed digitally. They constructed a prototype dosimeter using a lensless Fourier transform (LFT) configuration to capture holograms and reconstructed them digitally. Their proof-of-concept dosimeter succeeded at measuring dose distributions under several challenging paradigms, including high-dose-rate brachytherapy and proton minibeam therapy modalities [26].

The work of Cavan and Meyer established a modern proof-of-concept as to the utility of DHI for dosimetric metrology, and their work has been furthered by other researchers in recent years [67, 68].

Theory of DHI Dosimetry

The fundamental principle underpinning DHI dosimetry is that the refractive index of water will change in response to temperature perturbations. Since radiation dose as defined by Equation 2.35 has the units of energy deposited per unit mass in water, a given radiation dose will correspond to a specific change in temperature in the water-filled test cell, which will in turn result in a certain defect being created in the refractive index of the irradiated water. As per Equation 2.16, the optical path length of the light in the test cell is therefore altered by this refractive index defect, and the fringe pattern on the detector will be modified according to this ΔOPL.

According to the definition of absorbed dose, the dose (D) is calculated using Equation 2.35

$$D = \frac{E}{m}, \tag{2.35}$$

where E, measured in Joules is the total energy deposited over a mass, m of water, measured in kilograms. The specific heat of any material is similarly defined by Equation 2.36

$$c = \frac{\Delta E}{\Delta T m}, \tag{2.36}$$

where ΔE is the amount of energy deposited to induce a temperature change of ΔT in a given weight, m of the medium. Substituting the specific heat of water (4185.5 J/kgK) into Equation 2.35 yields an identity for the change in temperature due to deposited radiation dose, 2.37.

$$\Delta T = \frac{D}{c} \tag{2.37}$$

The relationship between water temperature and refractive index is empirical rather than analytical, so a polynomial of the form $P(T) = n$ is required to convert the known temperature change ΔT to a refractive index change Δn. The fitting process and data used to generate the polynomial for this research is outlined in Section 4.1.2.

With the dependencies of dose, temperature, and refractive index quantified, the two-dimensional map of phase defect $\Delta\Phi$ between the object and reference states of the test cell can then be converted to an optical path length change, ΔOPL via Equation 2.38.

$$\Delta OPL = \frac{\Delta\Phi\lambda}{2\pi} \tag{2.38}$$

where λ is the laser wavelength. Equation 2.16 from Section 2.1 can then be used to convert the change in optical path length to a change in refractive index, such that

$$\Delta n = \frac{\Delta OPL}{d}. \tag{2.39}$$

This suite of equations therefore provides a pathway for the calculation of absorbed dose to water, D from the change in phase across the two-dimensional test cell, $\Delta\Phi$, as given by the reconstructed holograms.

2.4 Results of the Prototype DHI Dosimeter

Cavan and Meyer's research into interferometric dosimetry was undertaken according to the principles outlined above. Their prototype LFTDH dosimeter successfully provided a proof-of-concept as to the utility of DHI for the purposes of radiation dosimetry. However, the prototype dosimeter had high uncertainties, with the best-case interpretation of their results suggesting a minimum uncertainty of 15% on a 40 Gy dose when measured against treatment planning simulations [26].

The main sources of uncertainty contributing to the high noise levels and resulting lack of sensitivity were environmental and mechanical. The prototype dosimeter was intended only as a proof-of-concept, and so was constructed on a strict budget from mostly repurposed optical components. It was large and fairly heavy, filling most of a 25 $\times$75 cm optical breadboard, and only rudimentary environmental isolation was able to be employed,

leading to high levels of noise due to the influence of ambient parameters. The prototype configuration also lacked portability, so had to be disassembled for transport and reassembled on-site for measurements, which greatly affected the reproducibility of Cavan's results.

The key challenge encountered by Cavan and Meyer in their testing of this prototype was that the impact of therapeutic radiation doses upon the refractive index of water was extremely small. The calculation of refractive index of water is discussed in full in Chapter 4, but in brief, clinical quality assurance doses for typical radiotherapy modalities are on the order of 1 Gy. As per equation 2.37 above, a deposited dose of 1 Gy corresponds to a temperature increase of

$$\Delta T = \frac{1}{4185.5} \quad \left[\frac{\mathrm{J}}{\mathrm{kg\,K}}\right] \tag{2.40}$$

yielding a temperature change of 239 µK, which induces a refractive index change on the order of 10×10^{-9} in a water sample. In addition, clinical dosimetric standards as set by the ICRU and the IAEA recommend uncertainties of no more than 2% in clinically measured dose, in order to keep the total uncertainty below the recommended 5% limit [19]. This implies that, as a rough estimate, a dosimeter will need to have a resolution of approximately tens of micro-Kelvin in order to be clinically useful. A fine temperature resolution will also make the DHI dosimeter more useful for real-time visualisation of dose deposition, since the ability to resolve small dose differences will allow dose maps at smaller time intervals to be distinguished.

2.4.1 Proposed Improvements and the Role of Modelling

Many experimental improvements were suggested by Cavan and Meyer following the testing of the DHI dosimeter prototype, and Cavan's thesis discussion can be consulted for a full review [26]. Some of the suggestions, like miniaturising the system and conducting other geometric improvements are simple and cost-effective to test. However, others, like acquiring new optical components, adding additional detector surfaces, and altering the laser source require the procurement of new components, some of which are prohibitively expensive.

To this end, it was deemed prudent to simulate the interferometer in an optical modelling program in order to fully quantify the effect of different uncertainties and assess which improvements would be the most cost-effective. The aim of this research is therefore to determine the viability of modelling the prototype dosimeter in a current optical modelling package (FRED, produced by Photon Engineering LLC in Tucson Arizona) in order to confirm that this plan of action is feasible.

Chapter 3

Principles of Optical Modelling

In the previous chapter, the propagation and energy distribution of light waves is described in terms of four-dimensional solutions to the wave equation (Equation 2.1). Although physically rigorous, this formulation is cumbersome in application and computationally expensive, so a different method is necessary for approximating optical paths in computer modelling applications. Although the precise algorithms used in FRED (the computational suite used in this research) are proprietary and thus unknown, the general principles behind their application will be discussed in this chapter.

3.1 Geometric Optics

Geometric optics is the foundation of most computational optical methods. The utility of geometric optics lies in its treatment of wave fields as collections of vectors whose propagation is equivalent to transformation by a series of linear operators [69]. Modelling optical sources via geometric optical methods is therefore more computationally viable than using the four-dimensional solutions to Maxwell's wave equation, since all the computational steps are executable with linear algebra, with no numerical approximations needed [70].

At the heart of geometric optics is the ray, an abstraction which approximates the path along which light propagates under certain conditions. Geometric optics is underpinned by four assumptions which govern ray behaviour. These state that rays propagate in straight lines in homogeneous media, bend and may split at the interface of dissimilar media, follow a curved trajectory in materials with a variable refractive index, and may be absorbed or reflected at the interface between some media.

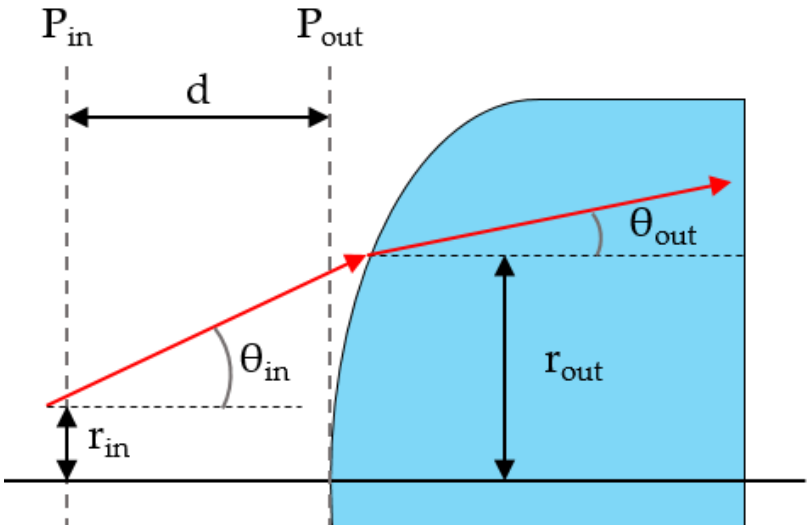

FIGURE 3.1: Geometry of ray transfer matrix analysis for an optical element.

A ray is taken to be the line which is normal to the wavefront of a light wave at any given point. The direction of the ray is thus the same as the wave vector (**k**) at any given point [69].

3.1.1 Ray Transfer Matrix Analysis

In an optomechanical system where all elements are perfectly aligned along the optical axis, a ray can be fully characterised by a two-dimensional vector, **r**, given by:

$$\mathbf{r} = \begin{bmatrix} r \\ \theta \end{bmatrix}, \tag{3.1}$$

where r is the distance of the ray away from the optical axis and θ is the angle of propagation away from the optical axis, as shown in Figure 3.1. Each optical interface that the ray encounters is assigned a 2×2 matrix with the form of the matrix determined by the nature of the element. An input ray ($\mathbf{r_{in}}$) encountering a particular element is operated on by the element matrix (M_E), such that the output ray ($\mathbf{r_{out}}$) is given by

$$\mathbf{r_{out}} = M_E \, \mathbf{r_{in}}. \tag{3.2}$$

Figure 3.2 illustrates a generalised system with an arbitrary number (n) of optical interfaces where this type of analysis might be applied. The system is divided into a series of reference planes, numbered 1 through $2n + 2$. Each

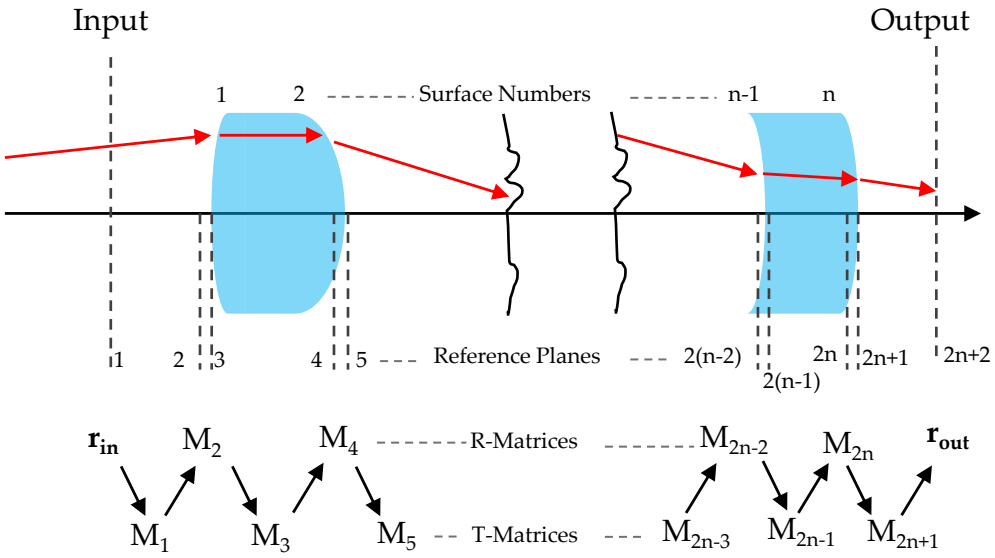

FIGURE 3.2: Schematic of the construction of a ray transfer matrix for a generalised optical system. Adapted from [70].

plane is assigned a matrix M such that for every reference plane index i,

$$\mathbf{r_i} = M_i \mathbf{r_{(i-1)}}. \tag{3.3}$$

The radial coordinate and angle of the ray at each optical interface can therefore be calculated via successive matrix manipulations, such that

$$\mathbf{r_1} = M_1 \mathbf{r_{in}}, \quad \mathbf{r_2} = M_2 \mathbf{r_1}, \quad \dots \quad \mathbf{r_{out}} = M_{(2n+2)} \mathbf{r_{(2n+1)}}. \tag{3.4}$$

It follows that by substituting the expression for each ray into the next matrix multiplication, we obtain an expression for the output ray ($\mathbf{r_{out}}$) in terms of the input ray ($\mathbf{r_{in}}$) multiplied by each of the propagation matrices:

$$\mathbf{r_{out}} = M_{(2n+2)} M_{(2n+1)} M_{(2n)} \ \dots \ M_3 M_2 \ M_1 \mathbf{r_{in}}. \tag{3.5}$$

Therefore, a general 2×2 ray transfer matrix describing an entire optical system is equal to the outside product of the 2×2 matrices corresponding to each reference plane in the system. Equation 3.5 illustrates the computational expediency of geometrical optical methods; once the system matrix, M, has been calculated, modelling beam propagation through a system of any number of optics is reduced to a single matrix-vector multiplication operation.

The two-dimensional formalism is the simplest case of geometric optics and only applies to perfectly aligned systems which are completely centred on the optical axis. Matrix formalisms of higher order also exist, where three, four, and six dimensional matrices can be used to more thoroughly describe optical systems [71]. These higher order methods account for linear offset, tilt and skew of the optical elements from the system axis [72]. The algorithms of ray tracing are unchanged for these higher order methods, and full system matrices are found using the same methodology in higher dimensions.

3.1.2 Geometric Optics and Gaussian Beams

The ray transfer matrix analysis described above is useful for well-behaved light fields with a homogeneous cross-sectional energy density and discrete boundaries. Provided the field is paraxial and rotationally symmetrical about the optical axis, one ray placed at the field boundary is sufficient to characterise the field boundaries at the output of the optical system. It can also be assumed that the cross-sectional energy density is constant throughout the propagation, barring any absorption or reflection of energy.

Laser beams, which are used in our prototype dosimeter, do not meet these criteria. Instead of a homogeneous energy distribution, their transverse electric and magnetic field amplitude profiles are apodised in accordance with the Gaussian function

$$f(r) = ae^{\left(\frac{r-b^2}{2c^2}\right)}, \tag{3.6}$$

where a, b, and c are constants and r is the radius away from the central point of the beam. A Gaussian beam also diverges, meaning that its radius increases and its wavefront curvature evolves as it propagates. These evolving parameters can be completely expressed as long as the wavelength of the light (λ) and the radius of its smallest spot size, known as the beam waist (w_0), are known.

The beam waist size and wavelength are used to calculate a beam parameter called the Rayleigh length

$$z_R = \frac{\pi w_0^2}{\lambda}, \tag{3.7}$$

which is the propagation distance at which the beam radius is doubled [71]. The Rayleigh length can be used to express the evolution of the beam radius (w) as

$$w(z) = w_0\sqrt{1 + \left(\frac{z}{z_R}\right)^2}. \tag{3.8}$$

Similarly, the radius of the wavefront curvature can be expressed as

$$R(z) = z\left[1 + \left(\frac{z_R}{z}\right)^2\right]. \tag{3.9}$$

An important property of Gaussian functions is that their Fourier transforms are also Gaussian. This is significant; many optical operations are mathematically characterised as Fourier transforms applied to the electromagnetic field, so a Gaussian propagating through a Fourier optical system will retain its form. This means that a Gaussian beam will remain Gaussian as long as it travels through homogeneous media, refracts through thin lenses, or reflects from flat or gently curved mirrors [73].

3.1.3 Gaussian Beam Matrix Analysis

Although the geometry of Gaussian beams is more nuanced than that of the sources discussed in Section 3.1.1, ray matrix analysis can still be applied to propagate them through an optical system. This requires the calculation of the complex beam parameter, $q(z)$, which expresses the wavefront geometry and beam radius at a given point z along the optical axis:

$$q(z) = \frac{1}{R(z)} - \frac{i\lambda_0}{\pi n w(z)^2}. \tag{3.10}$$

The Gaussian beam can be propagated through an optical system in the same way as described above. The propagation equation for a Gaussian beam is given by

$$\mathbf{q_i} = \begin{bmatrix} q_i \\ 1 \end{bmatrix} = kM_i \begin{bmatrix} q_{(i-1)} \\ 1 \end{bmatrix} \tag{3.11}$$

where k is a normalisation constant to keep the second vector element equal to 1. A Gaussian beam can therefore be propagated through a general system

by substituting the complex beam vector for the position vector ($\mathbf{r_i}$) in Equation 3.5. The radius of wavefront curvature and the beam radius can thus be calculated from the complex beam parameter at any point in the beamline.

3.2 Complex Ray Tracing

The geometric optical techniques discussed above are computationally efficient, but they have some drawbacks. For systems with aspherical optical components or sharp apertures, this method requires the introduction of complex transmission functions, some of which poorly approximate the effects that they are intended to model [71].

More modern optical software packages, including FRED, use a more nuanced approach known as complex ray tracing, which utilises electromagnetic field formalisms for areas of free space propagation, but converts the field to a collection of rays at the surface of each material interface. This method is more successful at modelling non-paraxial surfaces and a wider variety of optical components.

3.2.1 Gaussian Beam Decomposition

Complex ray tracing for Gaussian beams is aided by the fact that any electromagnetic field distribution can be represented as a basis set of small Gaussian beamlets which are effectively treated as rays at optical interfaces. This decomposition facilitates the above computational method and stands as a middle ground between the ray and field formalisms.

This formalism originated with a Bell Labs scientist, Jacques Arnaud [74]. Arnaud proposed that Gaussian beams could be fully represented by a base ray and a collection of secondary parabasal rays, of which there are two types: waist and divergence. Parabasal waist rays propagate parallel to the base ray at a distance of the beam waist radius w_0, and effectively track the centre of the ray through the system. Divergence rays intersect the base ray in the plane of the beam waist, and propagate outwards in a cone at an angle θ, tracking the envelope of the diverging spherical wave in the far field. This collection of base, waist and divergence rays comprises one Gaussian beamlet, as shown in Figure 3.3.

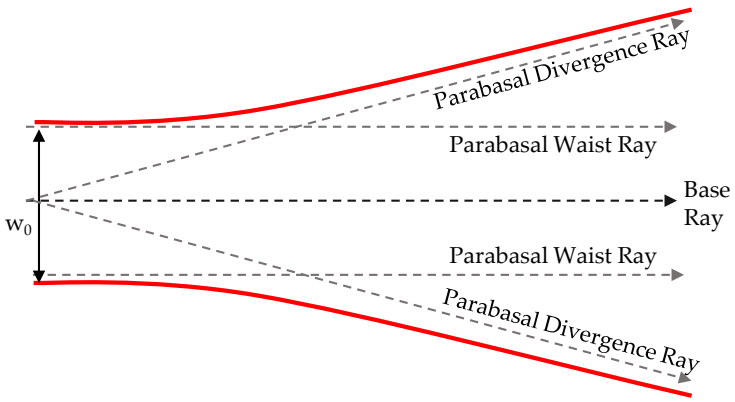

FIGURE 3.3: Illustration of the decomposition of a Gaussian beamlet into rays.

The divergence angle θ is calculated via the same equations which determine classical Gaussian beam divergence, such that

$$\tan\theta = \frac{\lambda}{\pi w_0} \tag{3.12}$$

where λ is the wavelength of the light and w_0 is the beam waist.

A superposition of Gaussian beamlets can be used to represent any optical field of interest. It is important to note that this representation is an approximation, the quality of which is highly influenced by the overlap factor between beamlets and the number of beamlets being used. Figure 3.4 shows beamlet diagrams and measured irradiance profiles for a flat square field represented by 121 rays with small, medium and large overlap profiles respectively. It is clear that if the overlap factor is too low, as in Figure 3.4a, the irradiance profile develops non-physical fluctuations with peaks at the centre of each beamlet. However, if the overlap factor is too large, small features are blurred by the large ray diameter, as in Figure 3.4c where the sharp field boundary appears as a Gaussian shoulder instead.

Equation 3.12 illustrates a final issue in parameter selection for the Gaussian beam decomposition approximation. Since increasing the ray number will decrease the waist radius in order to preserve the overlap factor, according to Equation 3.12, this will increase the divergence angle, θ, of the field. Ray overlap factor and number must therefore be balanced in order to achieve reasonable adherence to the field's irradiance map without the field becoming excessively divergent.

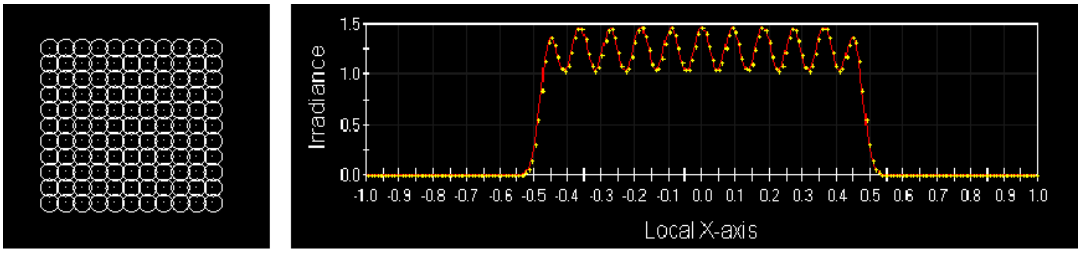

(a) Beamlet diagram and intensity profile for a Gaussian beam with a small overlap factor.

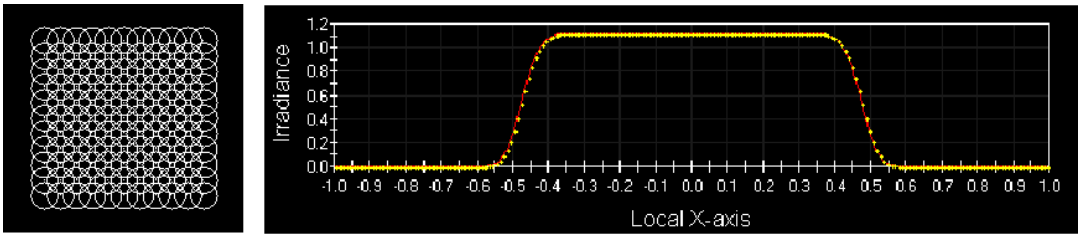

(b) Beamlet diagram and intensity profile for a Gaussian beam with a medium overlap factor.

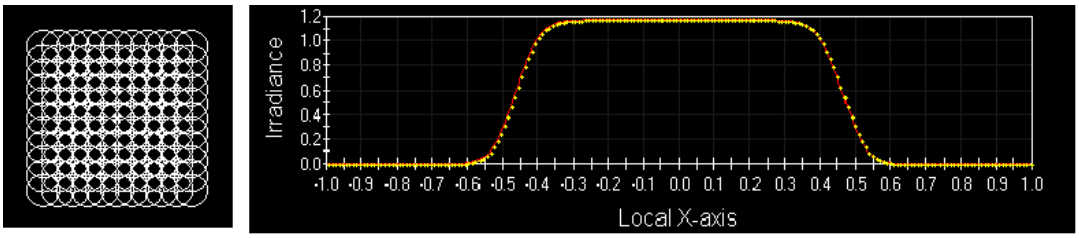

(c) Beamlet diagram and intensity profile for a Gaussian beam with a large overlap factor.

FIGURE 3.4: Comparison between Gaussian decompositions with different ray numbers for the same square laser field.

3.2.2 Field Resampling

Due to the balance between representing both the field irradiance and divergence of an optical source, different beamlet geometries are often required to adequately trace complex optical systems. For example, a configuration with fewer rays is desirable for tracing free-space propagation over long distances in order to avoid problematic levels of divergence [75]. Contrastingly, interaction with problematic optical elements, like hard-edged apertures or attenuators, requires a large number of sample points to adequately model the discrete amplitude steps at the edge of the field [76].

It is therefore common practice in complex ray tracing to generate new beamlet configurations at problematic areas in the optical system being traced. The rays will be propagated surface-by-surface through the system,

and when a resampling plane is reached, the irradiance map of the field is measured. A new beamlet configuration is then specified to replicate the field at this point. For large or highly irregular optical geometries, it may be necessary to resample the field several times. Commercial optical modelling software will generally include a GUI or scripting element to facilitate field resampling. FRED includes both, and their operation is discussed in Section 4.3.2 where a field resampling protocol was developed for the prototype LFTDH dosimeter model.

3.2.3 Analysis Tools

Tracking the evolution of the wave field as it is traced through a model is critical for creating optical simulations with complex ray tracing and coherent sources. Below is a brief summary of the FRED analysis tools used to monitor field parameters, troubleshoot the model and export the irradiance data as holograms. Each of these functions is executed on an analysis plane, which is the FRED analogue of a detector chip, with configurable dimensions and resolutions in the x and y axes. Any number of these surfaces can be added to the hierarchy in order to characterise the beam at any point in the model.

The 'Irradiance Spread' function mimics a simple camera acquisition, measuring a 2-D map of the wave intensity across the detector surface. It was used to check the spatial irradiance distribution for artefacts and to collect the holograms on an analysis plane configured to match the Pixelink CMOS detector.

The 'Gaussian Spot Size Diagram' (GSSD) analysis function returns a map of all the Gaussian beamlets, with each base ray plotted as a point with a circle around it representing the $1/e^2$ amplitude radius of the beamlet. The evolving radius of the $1/e^2$ beamlet radius can be used to track the divergence of wave fields through an optical model.

The 'Spatially Resample Field' function measures the irradiance map of a wave field on an analysis surface, then resamples the field into a new selection of Gaussian beamlets. Each pixel in the detector is used as the origin for one new base ray, and the beam overlap factor is specified to determine the waist size and divergence angle.

Finally, the scalar wave field function measures a wave field at the analysis plane and outputs a structure including two-dimensional maps of its phase, wavefront contours, and other complex parameters on the surface. This was not employed in any numerical analyses in this research, but was useful for troubleshooting problems with the simulation, since visualising the phase map of the reference and object beams was valuable in assessing unexpected hologram results.

Chapter 4

Initialising the FRED Model

As discussed in Section 2.3.1, interferometer sensitivity is of crucial importance for interferometric radiation dosimetry. Broadly speaking, a typical radiation dose delivered to water will generate temperature changes on the order of milli-Kelvin and will therefore perturb the refractive index of the water sample by 10^{-9} or less [77]. Therefore, any interferometer used in a clinical setting must be capable of resolving temperature changes of this magnitude, and FRED must be able to accurately model the nanoscale optical effects caused by these small changes if it is to be used to model our prototype interferometer.

In order to verify that FRED was fit for purpose before constructing a detailed model of our prototype interferometer, preliminary investigations were undertaken. To this end, a basic Michelson interferometer was first modelled to test the coherent light functionality of FRED against a well-understood system with easily verifiable results. The results of this analysis were used to confirm that FRED's handling of interferometric phenomena was sensitive to sub-wavelength changes in optical path length.

Once these preliminary explorations were completed, an extremely simplified version of the lensless Fourier transform interferometric dosimeter was constructed. In order to analyse the images acquired with this model, hologram reconstruction algorithms first had to be adapted from those developed by Cavan et al. Following this, the system required alignment and optimisation in order to yield useful results. Once the system was optimised, the spatial resolution and dose resolving power of the modelled interferometer were tested and compared to theoretical limitations and the experimental observations of Cavan et al.

Finally, once it was verified that FRED was fit for the purpose of modelling our prototype dosimeter, a complete model which included all beam-expanding optics and turning mirrors was configured. This required characterisation measurements to be undertaken on the laser so that an accurate representation of the optical source could be created. The optics used in the prototype dosimeter also had to be parametrised and individually created in FRED. Once the source and optics were initialised, the model was created, aligned and optimised, and the spatial and dose resolution were tested the same way as for the simple LFTDH model described above.

4.1 Michelson Interferometer

Before modelling the prototype LFT-style radiation dosimeter, we chose to confirm that the coherent light functionality in FRED was precise enough to be applied to interferometry. To this end, a simple Michelson interferometer was created in FRED's graphical design environment. The interferometer was similar to that used by Cavan in the early testing stages of her doctoral research [26], which in turn was based upon the interferometer used by Hussmann and Miller in their early research into interferometric radiation dosimetry [61].

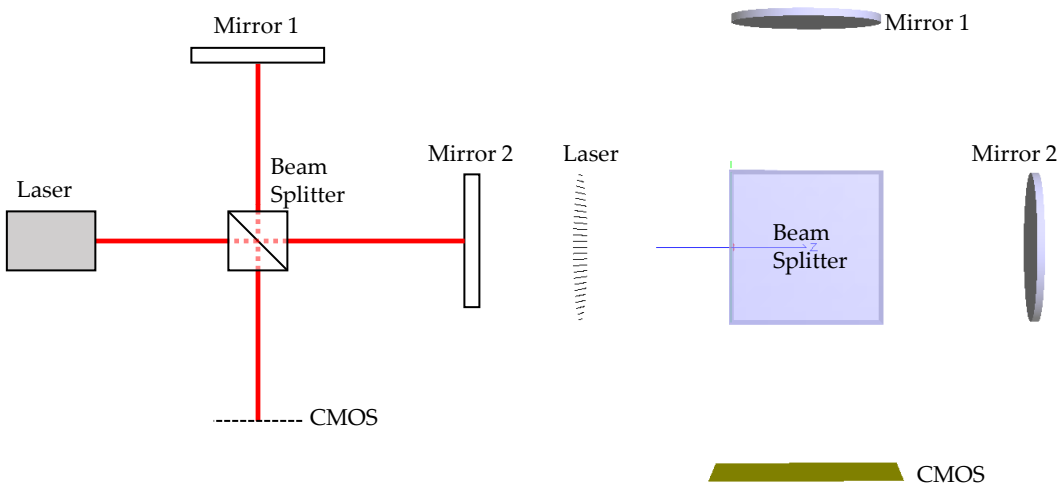

(a) Schematic of a simple Michelson interferometer

(b) FRED model of the Michelson interferometer.

FIGURE 4.1: The Michelson interferometer configuration used for preliminary experiments.

The Michelson interferometer is a simple double-pass interferometer consisting minimally of two mirrors and a beam splitter, as shown in Figure 4.1a. The beam splitter creates coherent reference and object beams, which are reflected from separate mirrors and recombined through the same beam splitter on the return trip. The recombined beams then fall upon the CMOS detector chip, which records the resultant interference pattern. If the reference and object mirrors are aligned at a precise right angle, the interference fringes manifest as concentric circles. However, if the object mirror is tilted off-axis, the expected fringe pattern will change from circular to linear comb-tooth fringes. A screenshot of the FRED model is shown in Figure 4.1b alongside the schematic of the interferometer.

4.1.1 Interferometric Testing Procedure

In order to ensure that the output of the FRED model was consistent with the physical reality of interferometry, simple changes were made to the geometry of the Michelson interferometer which would have predictable effects on the interference pattern.

First, the object mirror (M1) of the interferometer was incrementally translated over a distance of 316.4 nm, or half the HeNe laser wavelength. This increased the optical path length of the object beam by one wavelength while the reference beam remained fixed. The predicted effect of this translation was that the fringe pattern would cycle through one count, meaning that the central fringe would fade and reappear exactly once.

For the second test, the object mirror (M1) was tilted incrementally and the fringe pattern was recorded for each mirror inclination. As the mirror tilt became more pronounced, it was predicted that the path length difference in the object beam across the detector would increase. The expectation was thus that the fringes would form concentric circles when the mirror inclination was 0°, and would trend increasingly toward a linear comb-tooth pattern with increasing mirror tilt. The spacing of the fringes was also expected to decrease with increasing tilt, due to an increasing number of fringe cycles being represented across the detector.

Once these first tests confirmed that FRED's coherence handling was robust enough to be applied to interferometric systems in general, a specific

proof-of-concept of the principles underlying our DHI dosimeter was undertaken. A simple MATLAB script was created to calculate the change in refractive index in a water sample due to a given absorbed radiation dose. Next, this refractive index value was used to calculate the change in optical path length across a water cell in the prototype dosimeter. The mirror in the Michaelson interferometer was then translated to induce an equivalent ΔOPL in order to test whether a change of this magnitude was detectable in FRED.

4.1.2 Interferometric Testing Results

Mirror Translation

The fringe patterns generated by each mirror translation are shown in Figures 4.2a through 4.2f. Because this is a double-pass interferometer, note that each translation of the object mirror over a distance of 0.1λ, where λ is the laser wavelength, induces a ΔOPL of 0.2λ between the object and reference beams.

It can be seen that the central maximum is brightest in Figure 4.2a, where there is no path length difference. Translating the mirror by this length five times results in one fringe-count cycle where the central fringe broadens and dims in Figure 4.2b, reaches its minimum between Figures 4.2c and 4.2d, and then reappears in Figure 4.2e. In addition, it can be seen that the fringe patterns in Figures 4.2a 4.2f are identical, which is as expected given that in both these trials ΔOPL was an integer multiple of the wavelength.

This result is as expected, and aligns with the mathematics governing the fringe patterns of a Michelson interferometer [42]. This verifies that FRED's coherence physics handling is robust enough to resolve sub-wavelength optical path length changes, indicating that FRED is suitable for precision interferometry.

It is important to note that as the position data for optical elements is stored as a double precision number in FRED, there exists a hard lower limit on the resolution of small path length differences. However in the worst case, this lower limit is 15 decimal points, equivalent to atto-metre precision when the system units are set to milli-metres. This is many orders of magnitude below the optical path length shifts that we can measure, and therefore cannot impact the physical interpretation of our hologram results [78].

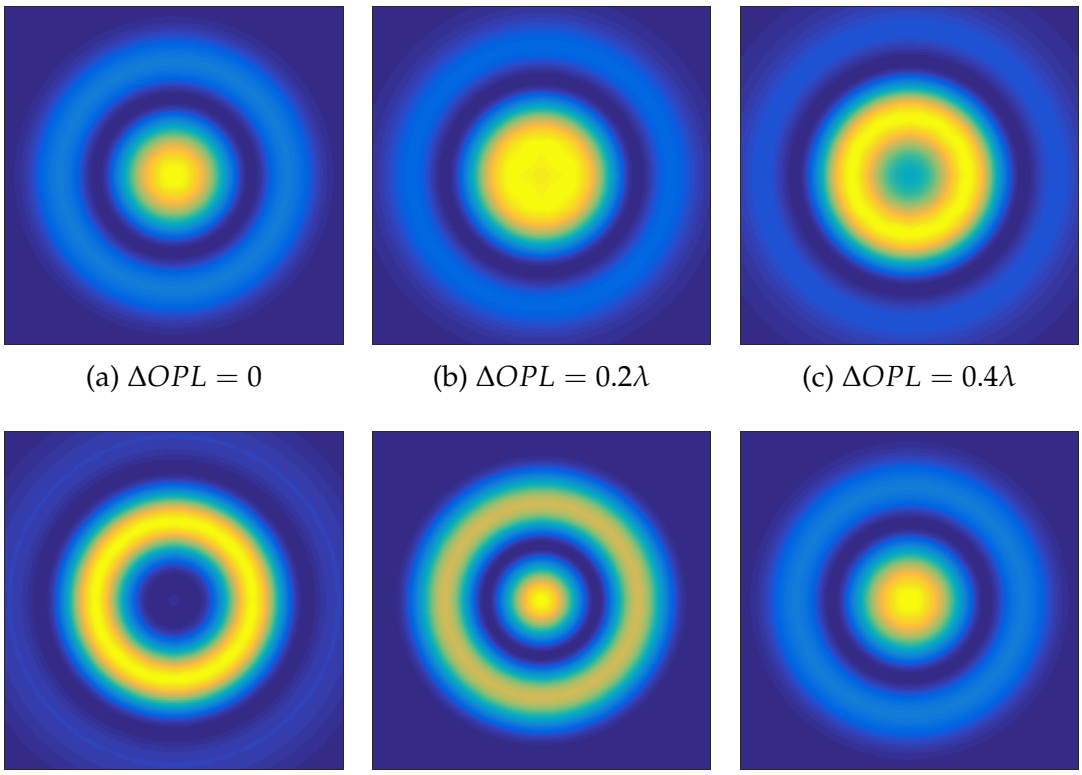

(a) $\Delta OPL = 0$ (b) $\Delta OPL = 0.2\lambda$ (c) $\Delta OPL = 0.4\lambda$

(d) $\Delta OPL = 0.6\lambda$ (e) $\Delta OPL = 0.8\lambda$ (f) $\Delta OPL = 1.0\lambda$

FIGURE 4.2: Evolution of simulated fringe patterns as mirror translation increases from 0 to 0.5 λ.

Mirror Tilt

As the mirror was tilted an increasing amount about its vertical axis, the fringe pattern generated by the interferometer shifted observably from concentric circles at 0° tilt in Figure 4.3a toward a comb-tooth pattern in Figures 4.3b and onwards. In addition, as the mirror tilt was increased, the fringes became less curved and more closely spaced, evolving toward a dense linear pattern at 1° mirror tilt in Figure 4.3f.

Both of these trends were as expected from the theory of a Michelson interferometer [42]. Increasing the mirror tilt increased the optical path length gradient across the detector, causing an increase in the number of vertical fringes observed. These observations were also consistent with those documented by Cavan during the early development of her interferometer [26].

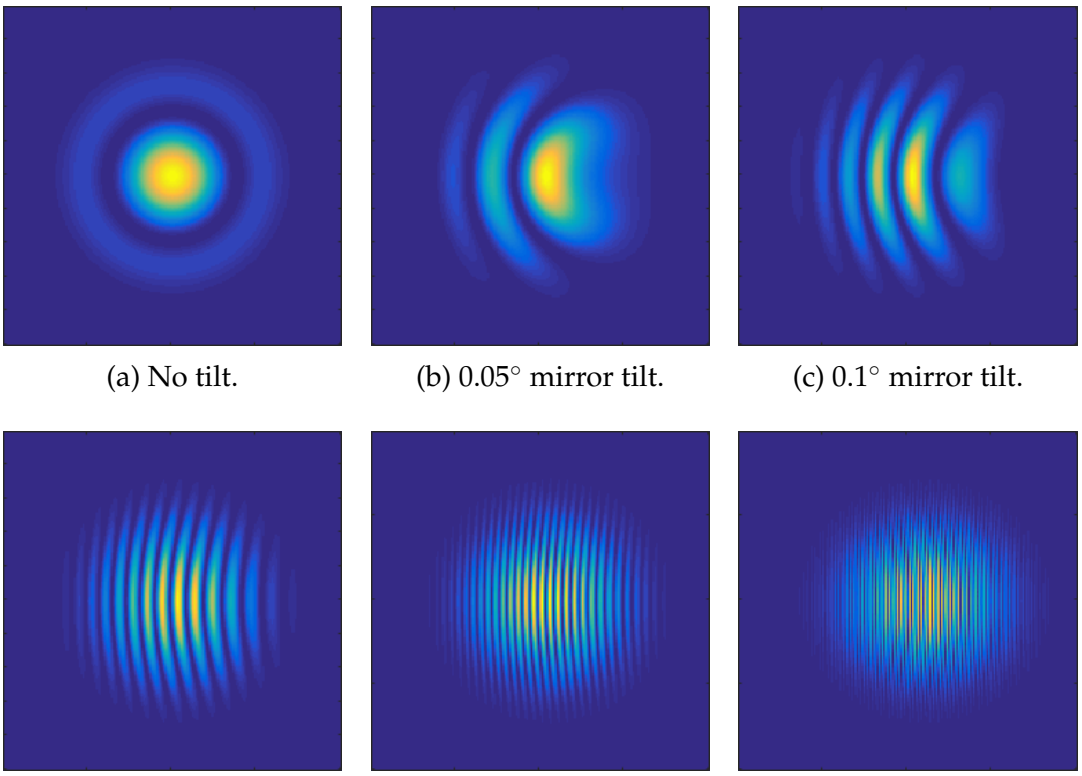

(a) No tilt. (b) 0.05° mirror tilt. (c) 0.1° mirror tilt.

(d) 0.25° mirror tilt. (e) 0.5° mirror tilt. (f) 1° mirror tilt.

FIGURE 4.3: Evolution of simulated Michelson interferometer fringe patterns as the object mirror (M1) was incrementally tilted from a 0° offset to a 1° offset.

Dose to Optical Path Length Calculations

In order to test that FRED was capable of resolving optical path length changes (ΔOPL) on the small scales associated with radiation dosimetry, a MATLAB routine, 'DoseToOPL', was developed. This script took user inputs of absorbed dose, initial cell temperature, and geometric path length through the test cell and returned the ΔOPL caused by the irradiation. The full 'DoseToOPL' script is included in Appendix A.1.

The first stage of this calculation proceeded exactly as described in our introduction to the prototype DHI dosimeter in Section 2.3.1. Specifically, Equation 2.37 was used to calculate the change in temperature of the test cell, and this value was added to the initial temperature to calculate the post-irradiation cell temperature.

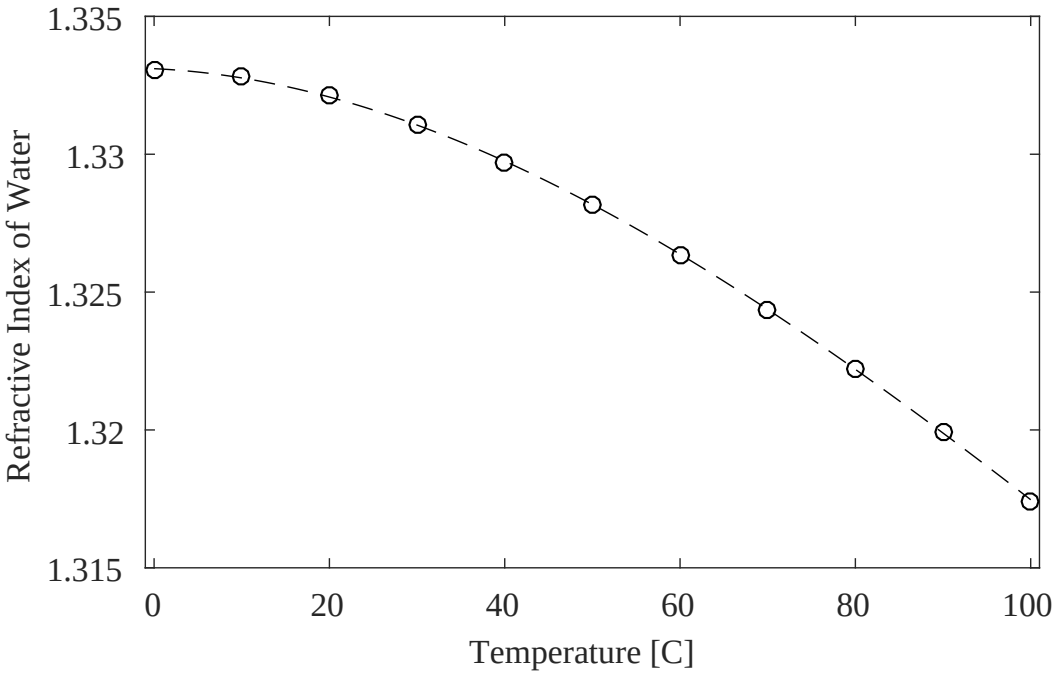

FIGURE 4.4: Graph of the measured refractive index data (circles) against the fitted third-degree polynomial (dashed line).

Calculating the refractive index of the test cell based on its temperature was more complex, as no analytical relationship exists between these quantities. An empirical method was therefore employed to calculate the cell's refractive index. Using data from a 2016 study [77], a third degree polynomial was used to estimate the relationship between refractive index and temperature. The experimental data and empirical fit are shown in Figure 4.4 as circled points and a dashed line respectively.

The data used to generate this fit and the complete coefficients of the polynomial P, where $n = P(T)$ can be found in Appendix A.1. This polynomial was used to calculate the expected change in refractive index of water given its initial temperature and the temperature increase induced by irradiation.

The final step in the calculation was to calculate the optical path length change (ΔOPL) induced by the alteration in refractive index. As stated by Equation 2.16, the optical path length is the product of the refractive index and the geometric path length. Therefore the change in optical path length is simply the product of the geometric path length and the refractive index change:

$$\Delta OPL = d\Delta n \tag{4.1}$$

This product was then subtracted from the reference optical path length, which was calculated for the cell at its initial temperature. The resultant ΔOPL was exported by the 'DoseToOPL' script.

Clinical OPL Resolution Test

With the 'DoseToOPL' script completed, a final test was conducted on the Michelson interferometer in order to establish that FRED was capable of sensing optical path length changes on the order relevant to clinical dosimetry. Three representative doses were selected and the change in optical path length (ΔOPL) induced by each dose was calculated. The test mirror in the Michelson interferometer was then translated to induce each of these path length changes and interference patterns were measured for each translation. The interference patterns were examined to ensure that there was a quantifiable difference between the zero-translation reference state and each of the irradiated states to confirm that FRED was capable of interferometrically sensing path length changes on the scales relevant to our dosimeter.

The doses selected for this test were intended to reflect clinically relevant dosimetric quantities. Specifically, optical path length changes corresponding to doses of 2 Gy, 2.04 Gy, and 0.008 Gy were calculated with the 'DoseToOPL' script and modelled in the Michelson interferometer. The 2 Gy dose was chosen to correspond to a total dose deposition of 200 Monitor Units (MU) on a typical linear accelerator under standard calibration conditions, a dose value which is routinely measured as part of linear accelerator quality assurance [19]. The dose of 2.04 Gy was selected to ensure that the required

Dose (Gy)	ΔOPL (mm)	Translation (mm)
0.008	3.3010×10^{-9}	1.6505×10^{-9}
2	8.2526×10^{-7}	4.1263×10^{-7}
2.04	8.4177×10^{-7}	4.2088×10^{-7}

TABLE 4.1: Parameters calculated with 'DoseToOPL' to establish the mirror translation necessary to model each dose.

uncertainty window of 2 % could be distinguished from the 2 Gy measurement. Finally, the dose of 8 mGy was chosen to roughly reflect one second of dose deposition at 50 MU/s, or 0.5 Gy s^{-1}, which is on the low end of the dose rate for clinical linear accelerators. Resolving a dose of this magnitude in FRED would allow us to model the potential real-time dose tracking applications of the prototype dosimeter.

It is important to note that these values are rough estimates of doses encountered in only one type of quality assurance radiation dosimetry. They are not reflective of all linear accelerator dosimetry, and do not apply to dosimetry on other modalities. However they are more than sufficient to provide an order-of-magnitude estimate of the path length changes which this dosimetric system, and thus the software being used to model it, are required to resolve.

Each absorbed dose investigated in this trial is shown in Table 4.1 alongside the optical path length change it induces, and the test mirror translation required to model it. These calculations assume an initial cell temperature of 20 °C and a test cell with a geometric path length of 20 mm, equal to the path length of the test cell used in our dosimeter.

Interference patterns were generated for each of the required mirror translation values, and profiles were collected across the centre of each one. The reference zero-dose profile was then subtracted from the profiles representing each of the dose-equivalent mirror translations. Figure 4.5 shows the difference plot between each of the profiles and the zero-dose profile. It can be seen that the profiles corresponding to the different doses are distinguishable from the zero-phase profile, and from one another. This is a very basic analysis, and does not take into account aliasing effects from phase overlap, but it serves as a basic proof of concept that FRED is capable of interferometrically sensing optical path length differences on the order of those found in clinical dosimetry.

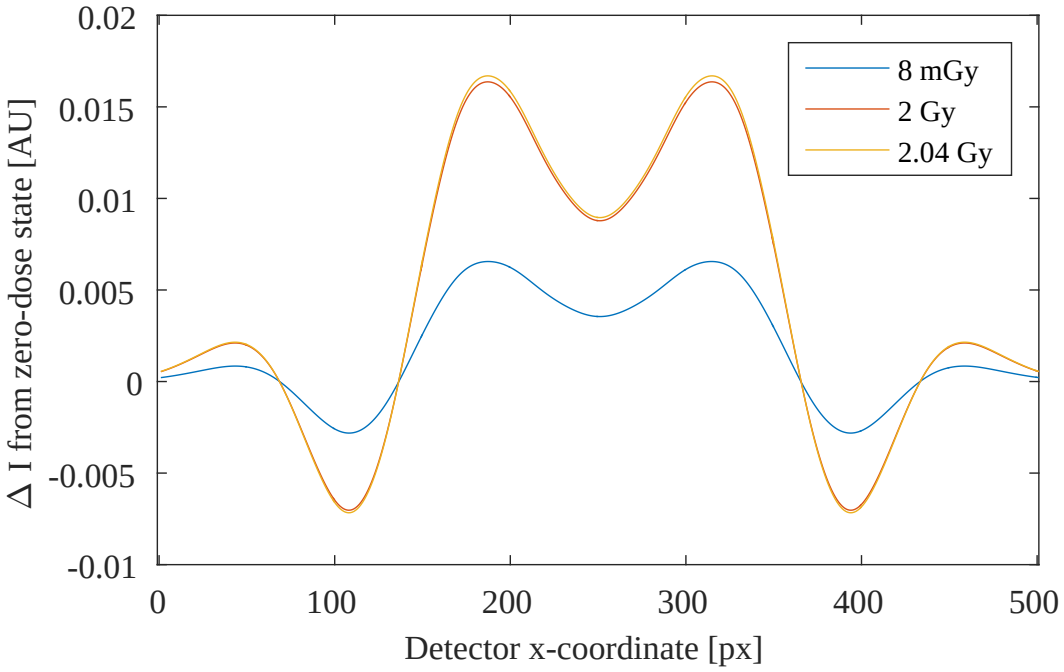

FIGURE 4.5: Differences between the zero-dose interference pattern and the pattern collected for each mirror translation corresponding to the OPL generated by the specified dose.

4.2 Simple LFTDH Model

In the Michelson interferometer trials, we verified that FRED was able to adequately model interference effects and resolve optical path length changes on the scales relevant to clinical DHI radiation dosimetry. With this confirmed, the process of modelling the prototype LFTDH dosimeter created by Cavan and Meyer was begun.

4.2.1 Model Configuration

Model Geometry

The initial simulation of the prototype dosimeter was configured as simply as possible, as per the diagram in Figure 4.6. To circumvent the beamsplitter and beam-expanding optics, the reference and object beams were initialised as two separate sources. The object beam was configured as a collimated plane wave with a semi-aperture of 10 mm, to represent a laser beam of radius 0.5 mm magnified by the 20-times maginfication beam expander. The reference beam was configured as a spherical wave emanating from a point source, replicating the reference beam after focusing by the plano-convex

lens. The CMOS was placed at 260 mm from the focal plane, which was the default object-to-camera distance cited in Cavan's thesis [25].

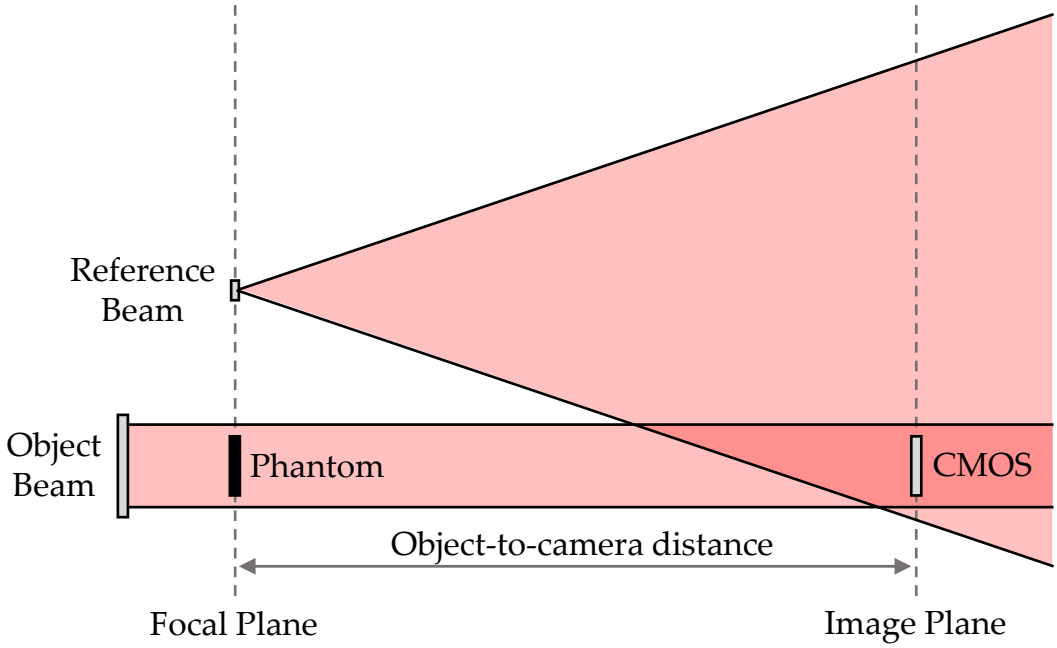

FIGURE 4.6: Schematic of the simplest FRED model initially used to represent the LFTDH dosimeter.

Several different phantoms were configured and added to the simulation so that different imaging tests could be conducted. Each of these is described in detail in the relevent section. All of the phantoms were centred on the optical axis of the object beam in the x-y plane, and on the z-coordinate of the reference beam focal point. Each phantom was then assigned the general keyword 'Phantom' and a second unique keyword identifier, such that its identity could be obtained programmatically.

Although greatly simplified, the basic geometry of this simple LFTDH interferometer is the same as that of the experimental prototype dosimeter, so the reconstruction algorithms used by Cavan et al. were able to be adapted to later reconstruct the holograms generated by this system.

Hologram Export Code

A FRED subroutine, 'ExportHolograms' was created in order to capture holograms from the simulation and export them in a tab-delimited format so that they could be easily imported into MATLAB. The code for this subroutine is included in Appendix B.1.

'ExportHolograms' has four user-specified parameters. The save directory and experiment name are specified by the user to construct the path and file names of the reference and object holograms. The name of the analysis surface being used to collect the holograms and the unique keyword attached to the phantom object being imaged are also specified by the user.

This script uses the 'Phantom' keyword to find the node number of every phantom object and set each of them to be untraceable, placing the interferometer in its reference state. The model is then raytraced, and the interference pattern between the object and reference beams is sampled using FRED's inbuilt 'Irradiance Spread Function'. Each element in this numeric matrix is then written to a .dat file and saved to the user-specified file name and directory.

The unique keyword identifier is then used to find the node number of the phantom object being imaged and set it to be traceable. The above process is then repeated and an object hologram is exported in the same manner, to the same directory. The reference and object hologram files are distinguished by the suffixes 'Ref' and 'Obj'.

4.2.2 Initial Hologram Reconstruction

Initial object reconstruction trials were carried out on a completely absorbing black square with an edge length of 2 mm. This trial was analogous to early tests conducted by Cavan on the prototype dosimeter, where letters printed on transparent sheets were imaged and reconstructed interferometrically [26].

The first hologram pair produced by this simulation is displayed in Figure 4.7, alongside a hologram pair captured experimentally by Cavan during her research. It can be seen that the simulated and experimental images have a similar underlying structure, with both exhibiting the concentric ring pattern which is expected from using a spherical reference beam. However, the simulated holograms are considerably less noisy, and the attenuating object is more easily visible in the simulation compared to the experimental data.

Despite the superficial similarities in the holograms, attempting the image reconstruction process described in Section 2.2.2 immediately revealed a problem. The first reconstructed interferogram produced by our simulation

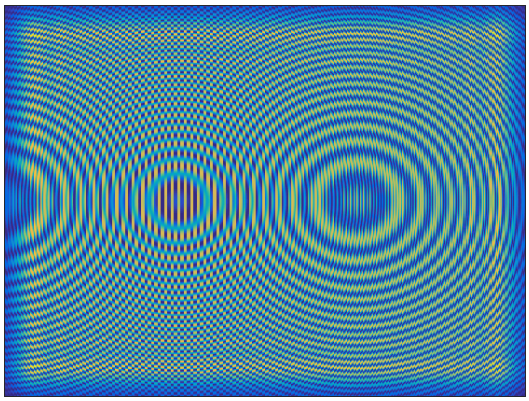

(a) Simulated reference hologram.

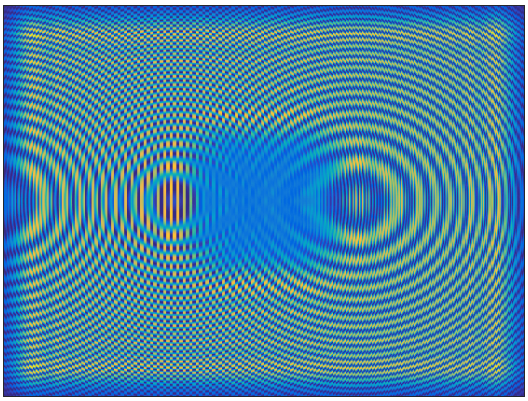

(b) Simulated object hologram.

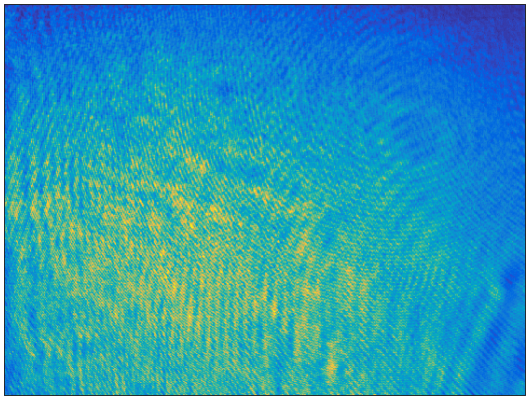

(c) Experimental reference hologram.

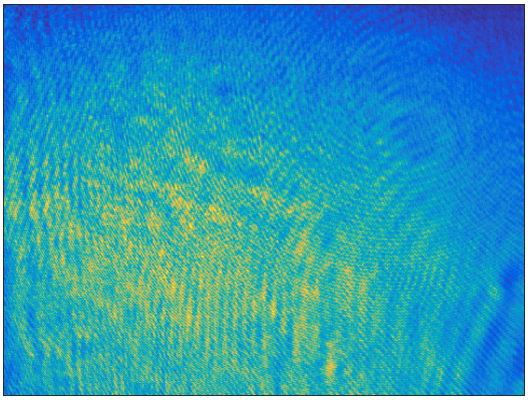

(d) Experimental object hologram.

FIGURE 4.7: Comparison between simulated and experimental holograms obtained from Cavan [26].

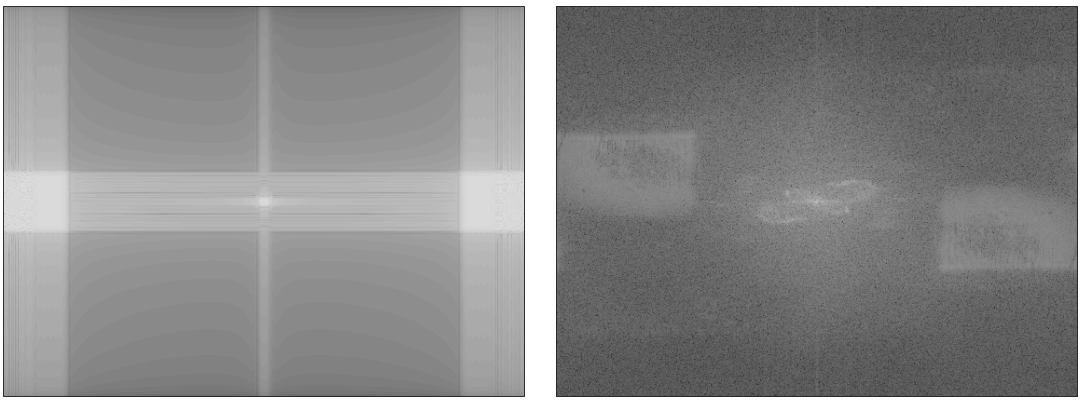

(a) Simulated interferogram. (b) Experimental interferogram.

FIGURE 4.8: Comparison between interferogram generated by simulated holograms and interferogram generated by experimental holograms obtained from Cavan [26].

(shown in Figure 4.8a) was quite dissimilar from that produced experimentally by the prototype dosimeter (shown in Figure 4.8b), to the extent that it was unclear whether the real and virtual image regions were present at all in the simulated interferogram.

Strong vertical and horizontal artefacts were observed in the simulated interferogram, but were not present in the experimental hologram reconstruction. These artefacts were hypothesised to be caused by the lack of atmospheric and vibrational fluctuation between the simulated reference and object holograms. Because the reconstructed interferograms are displayed in the frequency domain, the environmental noise in the experimental holograms causes a flattening of the background relative to the DC and image terms. This makes identifying the regions of interest in the experimentally derived interferogram considerably easier than in the simulated interferogram.

To solve this problem, Gaussian white noise was introduced to our simulated reference and object holograms in order to flatten the background of the interferogram and allow the image regions to be more readily observed. The resultant interferogram is shown in Figure 4.9a, and is much more similar to the reconstruction of the experimentally-derived holograms. From this reconstruction, it is apparent that the virtual and real images are present, but truncated due to poor interferometer alignment. The image regions are also affected by a new type of artefact, with regions of concentric circles appearing at the edge of the interferogram (shown in Figure 4.9b).

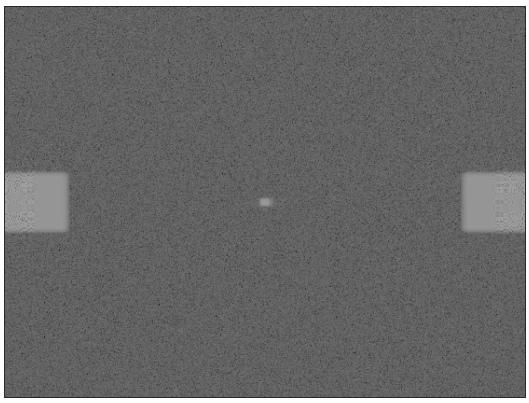

(a) Simulated interferogram with added Gaussian white noise.

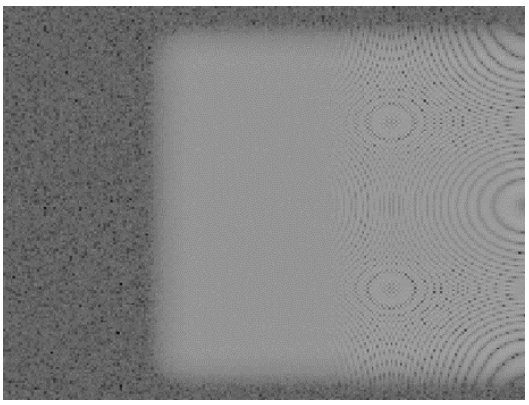

(b) Close-up of image region from Figure 4.9a showing edge artefacts.

FIGURE 4.9: Simulated interferogram after addition of white noise to holograms.

The image reconstruction GUI created by Cavan displays the interferogram generated by the selected holograms and allows the user to select the region of interest (ROI) containing the image to be reconstructed. In order to allow the user to select the correct ROI from within the artefact-free interferogram, the GUI was modified to temporarily add noise. This enabled easy visualisation of the correct ROI. Noise-free data are then passed to the reconstruction algorithm, such that the results are not affected by the added white noise. The modified image reconstruction code is included in Appendix A.3.

Figure 4.10d shows the final reconstruction of the first holograms obtained from the simulation. It shows the 2 mm attenuating square, partially distorted by the ring artefacts which appeared in the interferogram. To confirm that this square was in fact a reconstruction of our phantom object, the phantom was changed to a triangle pointing towards the top of the CMOS detector. The holograms are shown in Figures 4.11a and 4.11b. They were reconstructed by the same method, yielding the interferogram in Figure 4.11c and the reconstructed image in Figure 4.11d, showing that the reconstruction indeed reflected the phantom object, although distortions were caused by the edge artefacting in the image region.

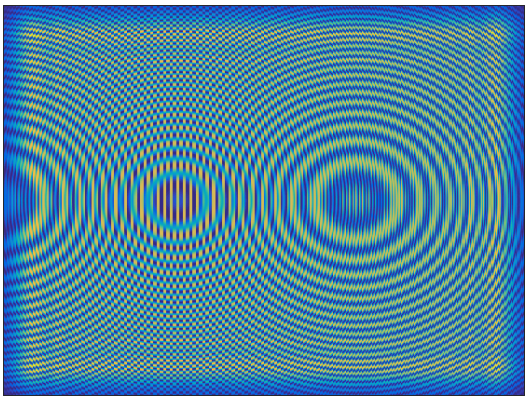

(a) Simulated reference hologram.

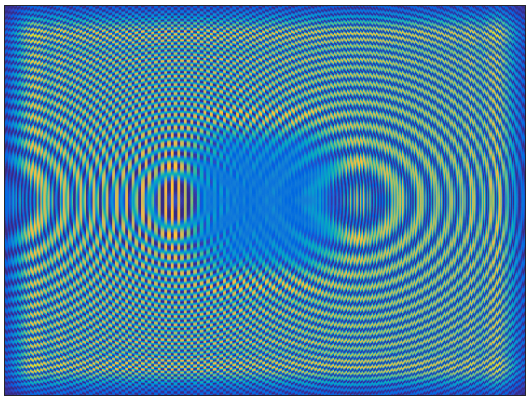

(b) Simulated object hologram with square phantom.

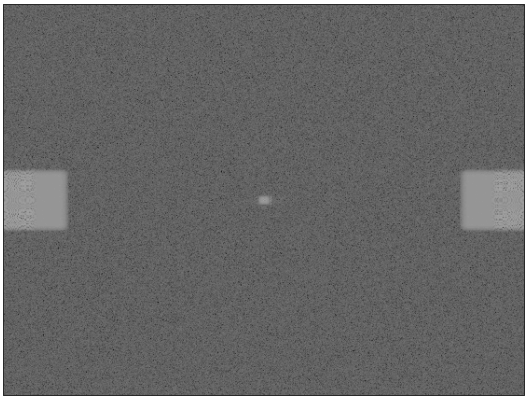

(c) Interferogram generated by the above holograms.

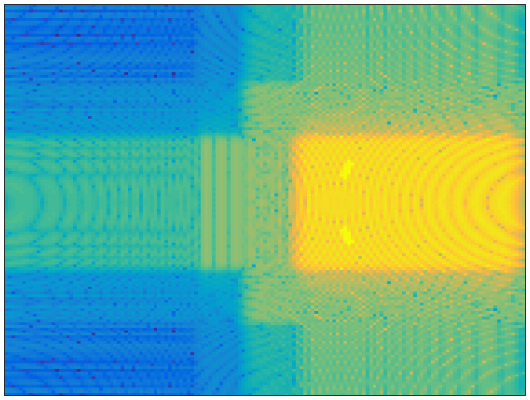

(d) Reconstruction of the phase difference map generated by the introduction of a square phantom object.

FIGURE 4.10: Image series showing the reconstruction process for the attenuating square phantom.

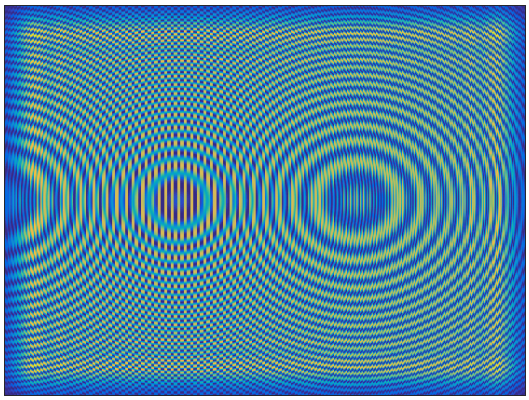

(a) Simulated reference hologram.

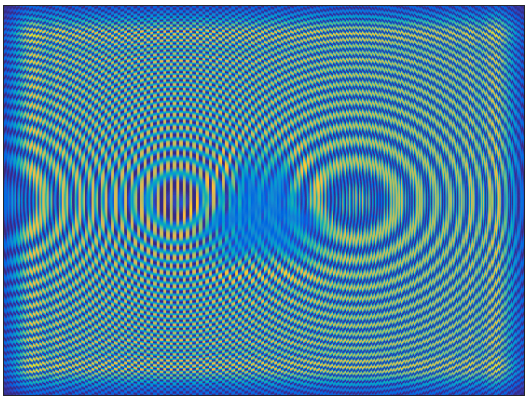

(b) Simulated object hologram with triangle phantom.

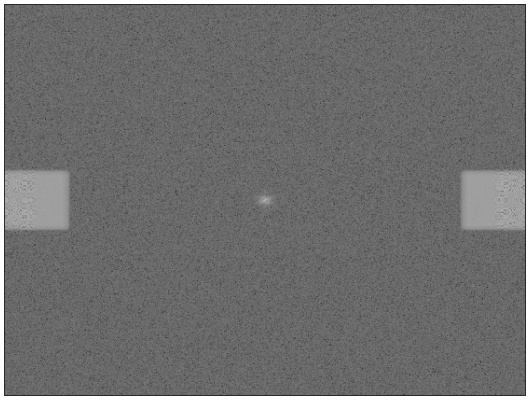

(c) Interferogram generated by the above holograms.

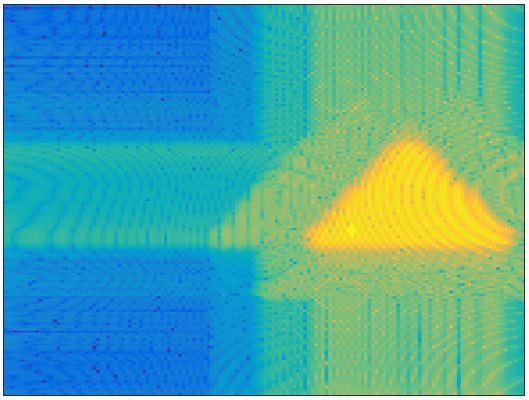

(d) Reconstruction of the phase difference map generated by the triangle phantom object.

FIGURE 4.11: Image series showing the reconstruction process for an attenuating triangle phantom.

4.2.3 Aligning and Optimising the Simulation

Following the partial success of our initial hologram reconstruction, the FRED model needed to be aligned and optimised. Optimising the lensless Fourier transform interferometer is a compromise between two goals. The first goal is to maximise the size of the twin and virtual images, such that the reconstruction area is of as high a resolution as possible. The second is to maintain sufficient separation in Fourier space between the bright central term and the images, such that reconstruction is not compromised by the DC term. Thus an ideal interferometer alignment will yield a reconstructed interferogram similar to the one shown in Figure 4.8b, obtained from Cavan's thesis.

There are two specific parameters in the model configuration which govern the geometry of the interferogram in frequency space. First, the distance between the focal plane of the reference beam and the camera is inversely proportional to the magnification of the real and virtual images. Second, the transverse separation between the object and reference beams in the plane parallel to the imaging surface, designated the x-y plane in our FRED simulation, governs the position of the image components of the interferogram. If the object and reference beams are co-incident in the x-y plane, the DC term and both images will be coincident in frequency space. Increasing their separation in the x-y plane will separate the images from one another and from the DC term.

Object-to-Camera Distance

To find a suitable object-to-camera distance, the z-coordinate of the analysis plane representing the CMOS chip was varied, and a hologram pair was collected at each distance. The reconstructed interferograms corresponding to object-to-camera distances of 125 mm, 250 mm, 375 mm, 500 mm, and 1000 mm are shown in order in Figures 4.12a through 4.12f.

It is apparent that the simulation obeys the magnification rule, and the image component increases in magnification with decreasing object-to-camera distance. Based on these results, a CMOS distance of 375 mm was chosen for the next round of optimisation, as the intrerferogram generated at this distance (shown in Figure 4.12c) had suitably magnified image components without being truncated.

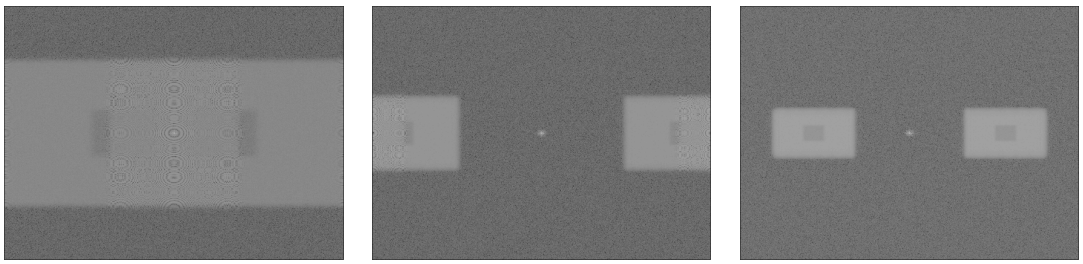

(a) Object-to-camera distance of 125 mm (b) Object-to-camera distance of 250 mm (c) Object-to-camera distance of 375 mm

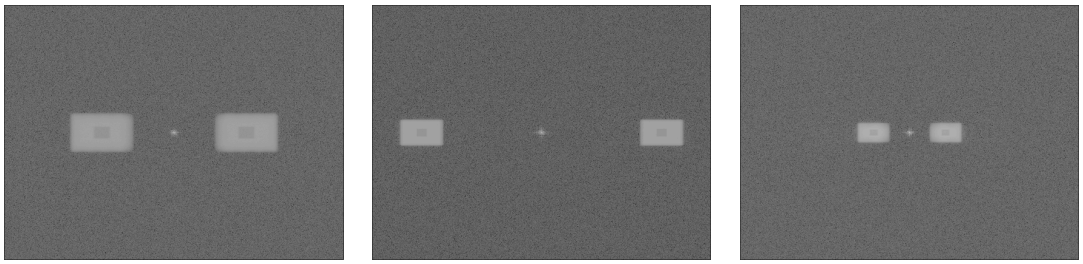

(d) Object-to-camera distance of 500 mm (e) Object-to-camera distance of 750 mm (f) Object-to-camera distance of 1000 mm.

FIGURE 4.12: Comparison of interferograms with varying object-to-camera distance.

In addition, the magnification trials revealed the source of the ring artefacts observed in the image regions of the first interferogram, displayed in Figure 4.9b. It can be seen in Figure 4.12a that when the image regions are magnified to the extent that they overlap in the centre of the interferogram, the same ring artefacts are observed in the areas of overlap. The pattern on the initial reconstruction in Figure 4.9b is thus presumed to be the result of overlap of the image regions on their outside edges, due to the cyclic nature of fequency space.

Reference Beam Focus Position

With a suitable CMOS distance selected, the x and y coordinates of the reference beam's focal position were adjusted in order to optimise the position of the images within the frequency domain of the interferogram. Separations of 10 mm, 7.5 mm, and 5 mm between the centre of the object beam and the reference beam were tested. The results are displayed in Figure 4.13

Using a smaller separation between the reference and object beams created a larger buffer between the edge of the interferogram and the image components. This meant a greater magnification of the image components

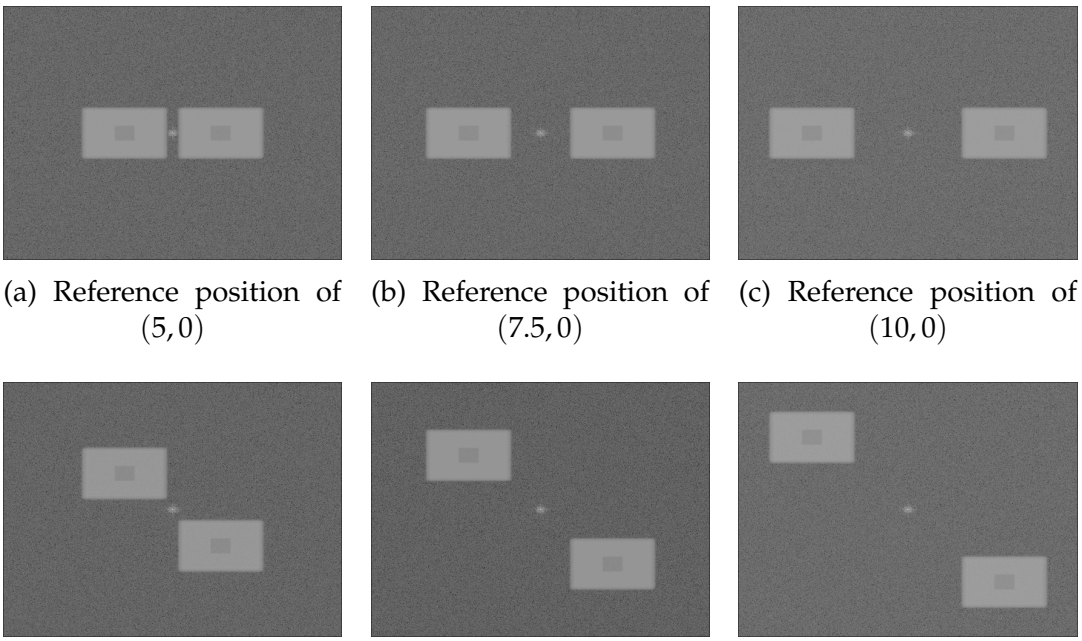

(a) Reference position of $(5, 0)$ (b) Reference position of $(7.5, 0)$ (c) Reference position of $(10, 0)$

(d) Reference position of $(5, 5)$ (e) Reference position of $(7.5, 7.5)$ (f) Reference position of $(10, 10)$

FIGURE 4.13: Comparison of interferograms with varying reference beam position.

could be achieved. To facilitate this, the CMOS was shifted closer to the image plane, with a final reference position of $(x, y) = (6, 6)$ and an object-to-camera distance of 250 mm selected. The interferogram and reconstruction of the square from this final configuration is shown in Figure 4.14

This successful reconstruction marked the completion of our simple LFTDH model and the successful adaptation of Cavan et al's reconstruction algorithms to process the simulated results.

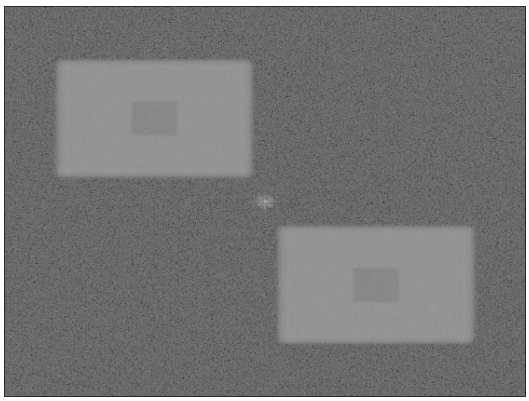

(a) Interferogram generated from final alignment.

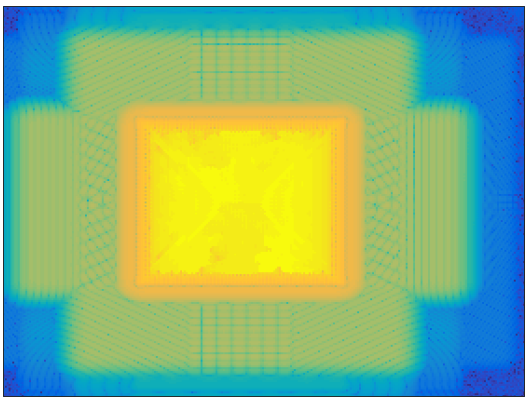

(b) Log display of the phase difference map generated by the attenuating square phantom.

FIGURE 4.14: Final interferogram and reconstructed phase difference ($\Delta\Phi$) map showing the attenuating square phantom.

4.2.4 Characterisation Tests

The bulk of the analysis in this thesis will be confined to the more complex LFTDH model, the development of which is described in Section 4.3 below. However it was important to ensure that the simple LFTDH simulation conformed to expected performance parameters before building on it to create more complex configurations. To this end, the spatial resolving power of the system was characterised, and it was tested that that the simple simulation was capable of resolving clinically relevant dose distributions.

Spatial Resolving Power

The most common metric of an imaging system's spatial resolving power is its MTF, or modulation transfer function. A system's MTF is effectively a plot of the contrast of a line pair imaged by the system against the spatial frequency of the line pair being imaged [79]. It is therefore used in many fields, from photography to medical imaging, to quantify how well small features are resolved by a given imaging system and assign a limit to the system's spatial resolving power. MTF measurement can be undertaken using several methods, and for a more thorough review of these, an imaging theory text such as Bushberg's *The Essential Physics of Medical Imaging* should be consulted [79]. In our case, to calculate the MTF of the virtual simple LFTDH dosimeter, a fully attenuating slanted-edge phantom was created in FRED and placed at the same location as the attenuating square from earlier trials.

Reference and object holograms were collected and reconstructed using the methodology outlined in Section 4.2.1.

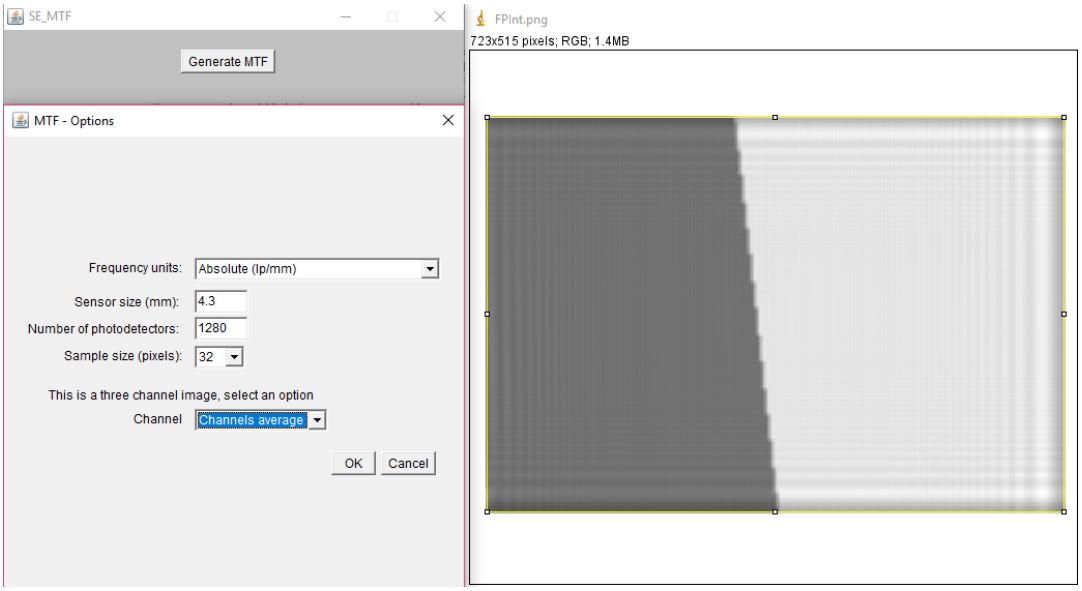

FIGURE 4.15: ImageJ plugin GUI used for MTF calculations.

The image processing software ImageJ, created at the National Institutes of Health in Bethesda Maryland, was then used to find the system's MTF from the image it acquired of the slant-edged phantom. An MTF processing plugin, created by Mitja et al. at the Polytechnic University of Catalonia, was used to carry out the MTF calculations [80]. A screenshot of the MTF calculation GUI is shown in Figure 4.15. To find the MTF, a region of interest was selected on the greyscale image of the phantom, and the detector size and resolution along one axis were entered so that an absolute MTF (expressed in cycles per mm) could be obtained. Detector size and resolution could also be omitted, and the resulting system MTF would be expressed in relative terms of cycles per pixel.

As described in Section 2.2.2, the algorithms which reconstruct our holograms into two-dimensional dose maps do so first by creating an interferogram (representing the interference phase between the reference and object states) and then by virtually re-illuminating this interferogram with the reference beam via an adapted Fresnel diffraction algorithm (Equation 2.31) in order to reconstruct the complex amplitude of the object wave in the image plane. The phase of this object wave ($\phi(x_I, y_I)$) can then be extracted and transformed from a discontinuous zero-to-2π phase map to a map of absolute phase difference ($\Delta\Phi(x_I, y_I)$) via aphase unwrapping algorithm created by Herráez et al. based on Equation 2.34 [81].

The first attempt to find the MTF of the interferometer was carried out using the two-dimensional $\Delta\Phi$ map obtained via the Herráez phase unwrapper (shown in Figure 4.16a). This attempt failed to produce a usable MTF, but examining the image immediately revealed the likely cause. The Herráez phase unwrapper is optimised for unwrapping continuous, gradual phase changes, rather than strong discontinuities with extremely high phase gradients [81]. The resultant phase-unwrapped image is therefore strongly artefacted, with blocky regions divided by jagged lines of phase change.

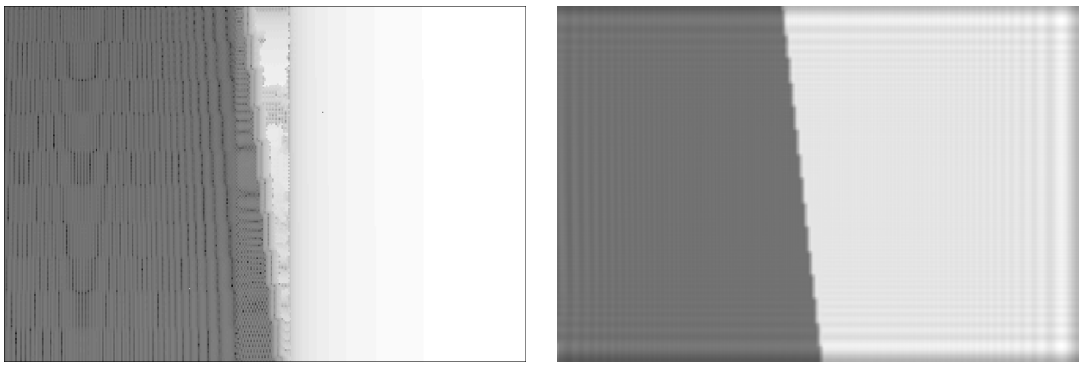

(a) The phase unwrapped reconstruction which failed to produce an MTF.

(b) The cropped image from the interferogram used in the MTF calculations.

FIGURE 4.16: Comparison between the two images used for MTF calculations.

Calculating MTF from a slanted edge relies on finding the edge spread function (ESF) of the image, converting this to a line spread function (LSF), and taking the Fourier transform in order to find the MTF [79]. The calculations assume a roughly sinusoidal and continuous LSF. It is therefore hypothesised that the MTF calculation failed for the phase-unwrapped image shown in Figure 4.16a because a continuous LSF of this nature could not be found. To solve this problem, the cropped image region of the interferogram (shown in Figure 4.16b) was used to calculate the MTF instead of the unwrapped phase map.

Using the interferogram image region to calculate the system MTF does not give an entirely complete picture of the dosimeter's spatial resolution. The phase unwrapper introduces artefacts, the nature of which vary depending on the phantom geometry and the steepness of the phase gradients in the reconstruction, and these artefacts will impact the spatial resolution beyond what the interferogram MTF will show. However, calculating the MTF based on the interferogram image region is sufficient to provide a point of comparison between the different interferometer configurations modelled over

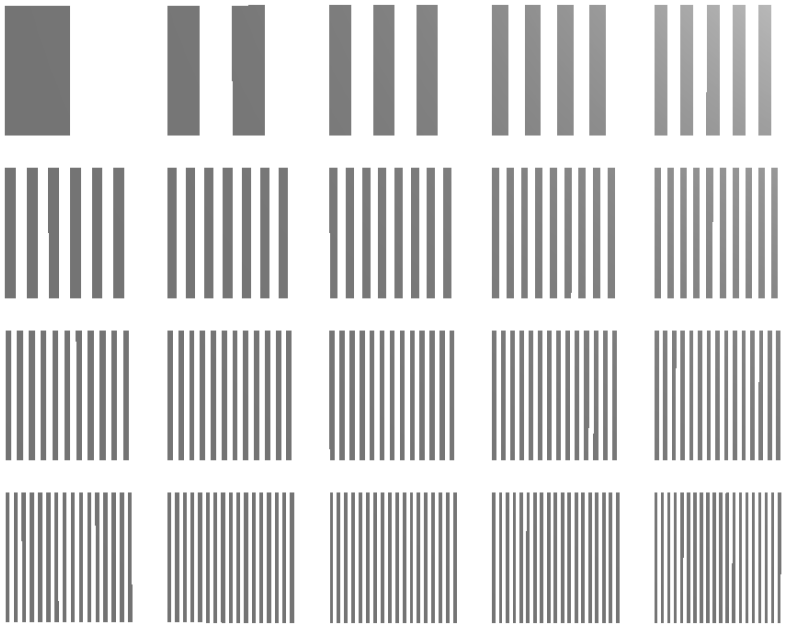

FIGURE 4.17: Screenshot of the fencepost phantom as configured in FRED.

the course of this research. This was thus the approach used from this point forward.

A more subjective measure of the system's spatial resolution was also carried out in order to quantify the impact of the reconstruction algorithms, in particular the phase unwrapper. A fencepost phantom was created in FRED in accordance with the image shown in Figure 4.17. It was configured as a plane with x and y dimensions of 6.5 mm and 5.25 mm respectively, and was divided into twenty 1 mm square regions. Each of these regions was populated with line pairs of a different spatial frequency from 1 lp/mm to 20 lp/mm.

This fencepost phantom was then imaged using the procedure described in Section 4.2.1 and the holograms were reconstructed and phase unwrapped. The unwrapped image was divided into its constituent regions and an average profile across each region was collected. These average profiles were examined subjectively to assess the spatial resolution limit of the system, where the number of line pairs in the region could no longer be clearly counted.

Dose Resolving Power

The ability of the simple LFTDH system to detect variations in dose across the test cell was then assessed. To achieve this, a contrast-detail test phantom was created in FRED. The phantom was configured as shown in Figure 4.18 with circular areas of varying refractive index arranged in a grid according to the amount of dose to water they represent in the x-axis (A through E) and their spot diameter in the y-axis (1 through 4). Columns A through E represent doses of 1 , 0.5 , 0.1 , 0.05 and 0.01 Gy respectively. The regions from rows 1 through 4 have diameters of 1 , 0.5 , 0.25 ,and 0.1 mm respectively. These dose areas were embedded in a block of room-temperature water.

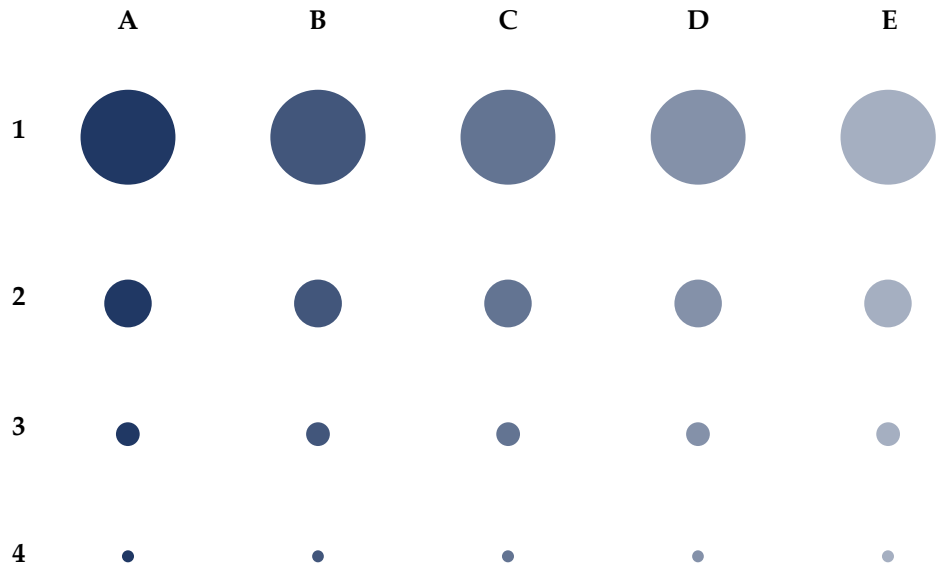

FIGURE 4.18: Schematic of the contrast-detail phantom created to test the dose resolution of our interferometer. Columns A through E represent doses of 1 , 0.5 , 0.1 , 0.05 and 0.01 Gy respectively. Rows 1 through 3 have diameters of 1 , 0.5 , 0.25 ,and 0.1 mm respectively.

An enitity's refractive index in FRED is determined by the "Material" parameter which is assigned to it. Thus several new materials were created in FRED to represent water after irradiation by each of the five doses listed above. The induced temperature change, final water temperature and resulting refractive indices were calculated for each dose using the methodology outlined in Section 4.1.2, using a polynomial fit to estimate the refractive index for water of each given temperature. The values for the modelled dose

Dose (Gy)	Water Temperature (°C)	Refractive Index
1	20.00024	1.332074501513100
0.5	20.00012	1.332074511828834
0.1	20.000024	1.332074520081388
0.05	20.000012	1.332074521112955
0.01	20.0000024	1.332074521938208

TABLE 4.2: Parameters calculated with 'DoseToOPL' to establish the mirror translation necessary to model each dose.

deposited, the post-irradiation temperature and the resulting refractive index of the water are shown in Table 4.2. These calculations assume an initial cell temperature of 20 °C, taken to be room temperature for the purposes of this research.

The contrast-detail phantom was added to the simulation and imaged. A reference hologram was acquired of the room-temperature water block with no added dose areas. The dose regions were then added to the phantom and an object hologram was acquired. An image of the contrast-detail phantom was then reconstructed as per the methodology previously outlined in Section 4.2.2. The reconstruction of the contrast-detail phantom was then examined to assess which voxels could be discerned.

4.2.5 Simple LFTDH Model Characterisation Results

Spatial Resolution

Figure 4.19 shows the MTF calculated from the interferogram image region. Conventionally, the spatial resolution limit of the system is taken to be the point at which $MTF(f) = 0.1$. The simple LFTDH simulation therefore has a spatial resolution limit of 47 lp/mm according to these MTF measurements. Since this neglects the impact of the hologram reconstruction process, this can be taken only as an upper estimate of the spatial resolution limit.

The phase-unwrapped reconstruction of the fencepost phantom, shown in Figure 4.20, was divided into its constituent regions to collect the average line profiles for each spatial frequency. The average profile collected for the 19 lp/mm and 20 lp/mm regions are shown in Figures 4.21a and 4.21b respectively. These are included to give an indication of the appearance of the line profiles just before and after the spatial resolution limit. in the first, 19

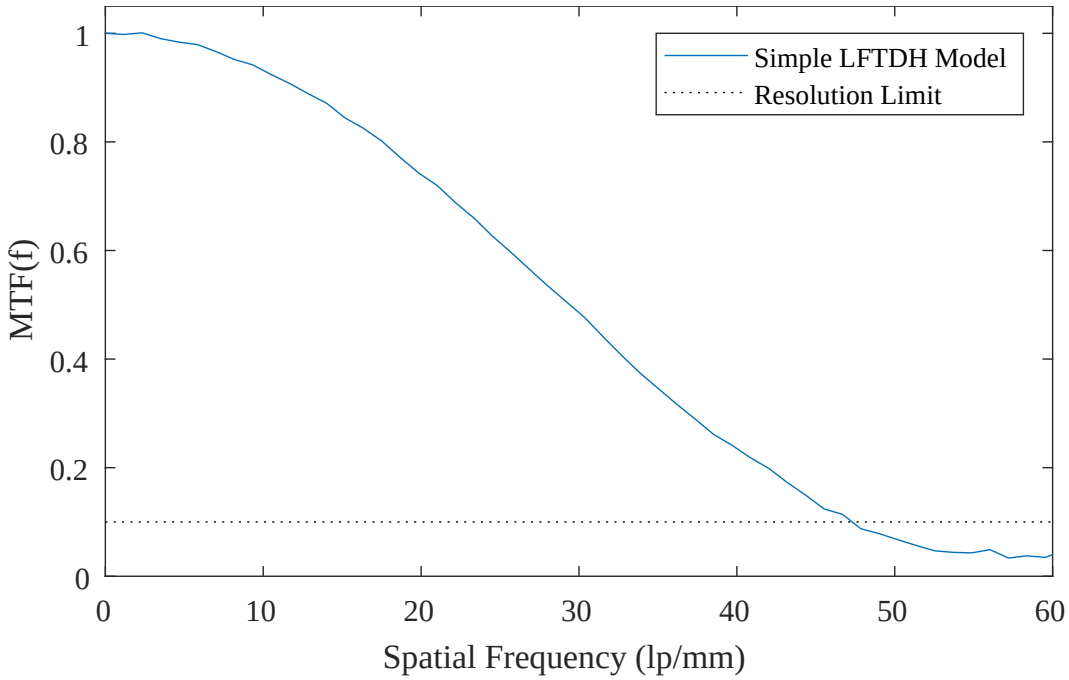

FIGURE 4.19: MTF of the simple LFTDH interferometer simulation.

peak-trough pairs can be clearly distinguished. In the second, the 20 peaks that should be present are not clearly defined. The spatial resolution limit of the system was therefore found to be 19 lp/mm. This is significantly lower than the spatial resolution limit given by the MTF in Figure 4.19, which is as expected since the fencepost test also accounts for the impact of the phase unwrapper.

Contrast-Detail Resolution

Examining the contrast-detail map shown in Figure 4.22a shows that every dose region except for the three smallest radius and lowest dose voxels can be resolved. As expected, the contrast drops as the dose decreases. This demarcation line between the visible and invisible voxels is plotted on the contrast-detail curve in Figure 4.22b. This result appears as expected, and the wide dynamic range between the highest and lowest dose voxels indicates that the phantom is suitably chosen to characterise our system.

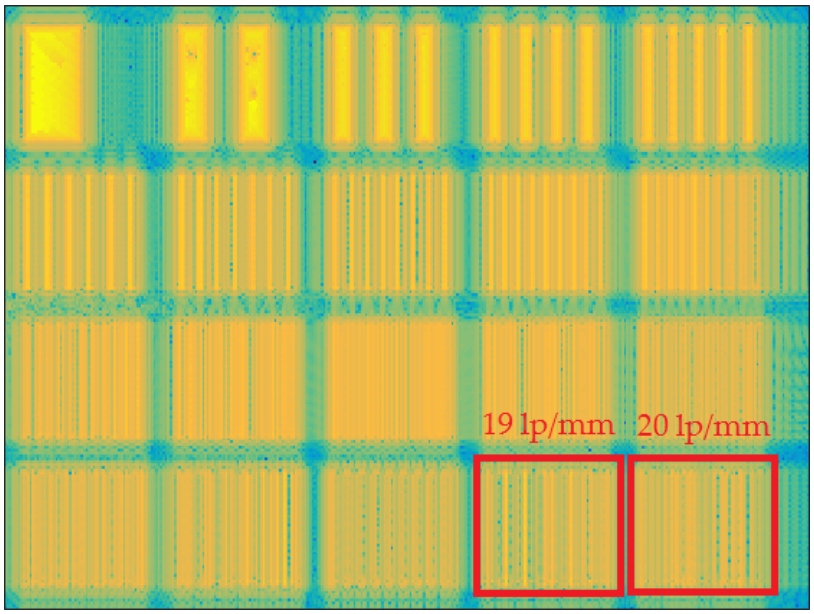

FIGURE 4.20: Reconstruction of the fencepost phantom for the simple LFTDH system.

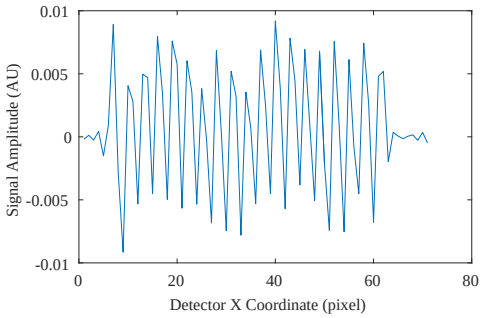

(a) Profile of the 19 lp/mm region.

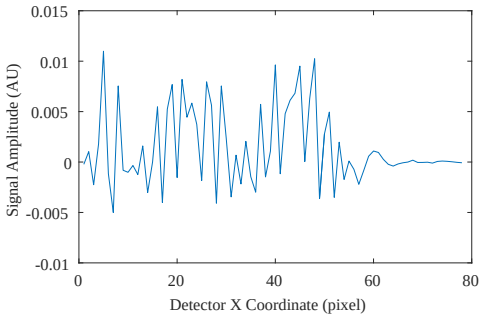

(b) Profile of the 20 lp/mm region.

FIGURE 4.21: Line profiles showing the spatial resolution limit of the simple LFTDH dosimeter.

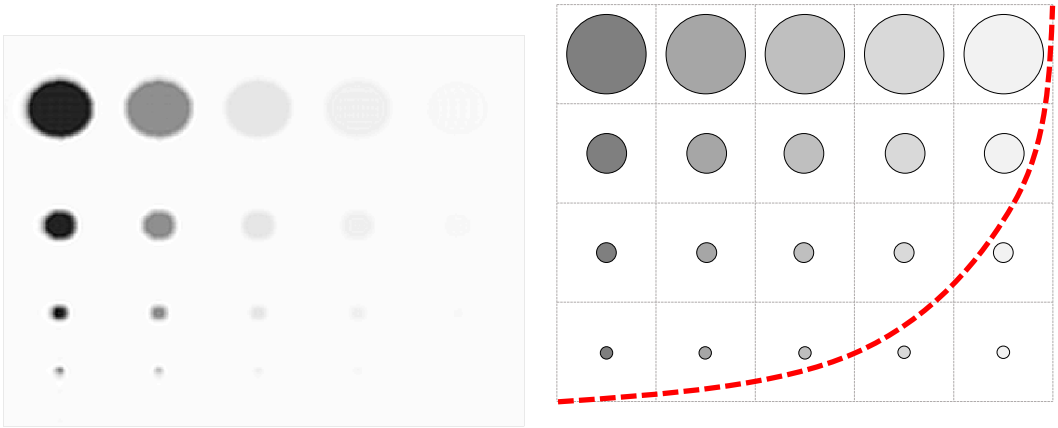

(a) Reconstruction of the contrast-detail phantom.

(b) Plot indicating visible voxels.

FIGURE 4.22: Contrast-detail results for the simple LFTDH model.

4.3 Full LFTDH Interferometer

The simple LFTDH model provided a proof of concept that interferometers of this configuration could be modelled in FRED, and their output could be reconstructed by the same algorithms applied to the experimental interferometer. With this assumption verified, we could proceed to modelling Cavan's full LFTDH interferometer configuration. The spatial and dose resolution meausurements of the simple LFTDH model were also used as a baseline to test the degree to which inclusion of the intermediate optics and longer beamlines caused the interferometer measurements to degrade.

4.3.1 Model Configuration

This model was created to more closely mirror the configuration used in Cavan's research and therefore included many more optical components. A schematic of this configuration is shown in Figure 4.23a, with a screenshot of the completed FRED model for comparison in Figure 4.23b.

The source for this model was configured as a Gaussian He-Ne laser beam with a waist semi-aperture of 1.25 mm. A cubic 50:50 beamsplitter was configured to have a side length of 10 mm and added to the model to generate the coherent reference and object beams. The reference beam was then passed through a plano-convex expander lens to fall upon the CMOS surface. The object beam passed through the beam expander and two pairs of turning mirrors, centring it on the water test cell. It then passed through the cell before falling on the CMOS plane where it interfered with the reference beam. Finally, an absorbing plane was created to stand in for the CMOS detector chip used in the prototype, and an analysis surface with the same resolution as our CMOS detector (sourced from Pixelink in Ottowa, Canada) was attached to it.

The exact lens parameters of the beam expander used in the prototype are unknown, as the full design is a Thorlabs intellectual property. In place of a detailed schematic, a simple two-lens Galilean telescope was created to achieve the same 20-times magnification factor. The apertures of the input and output lenses and the spacing between them were measured, and the virtual Galilean telescope was created to match these parameters.

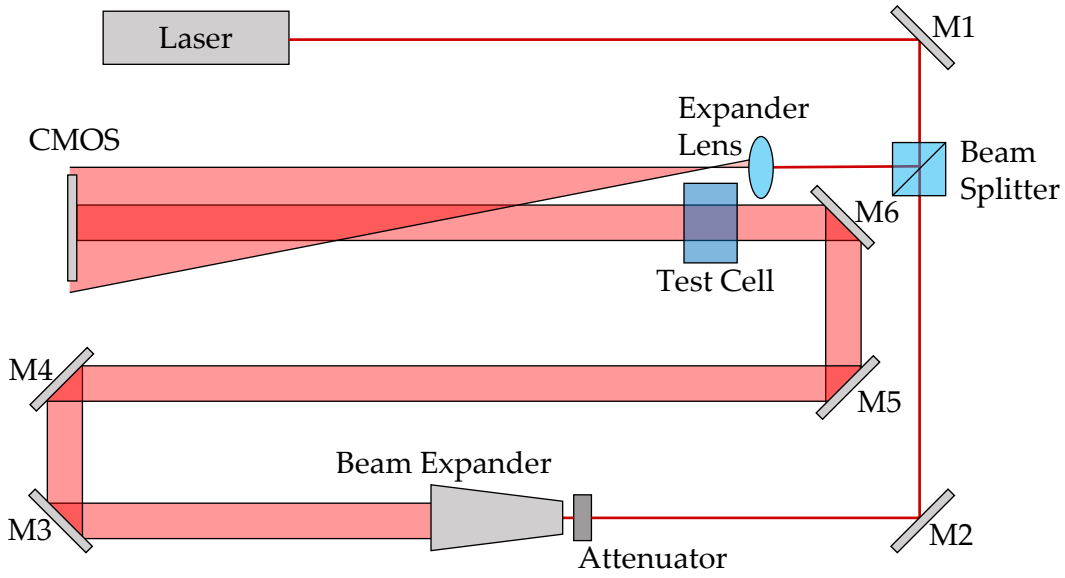

(a) Schematic of the full LFTDH interferometer.

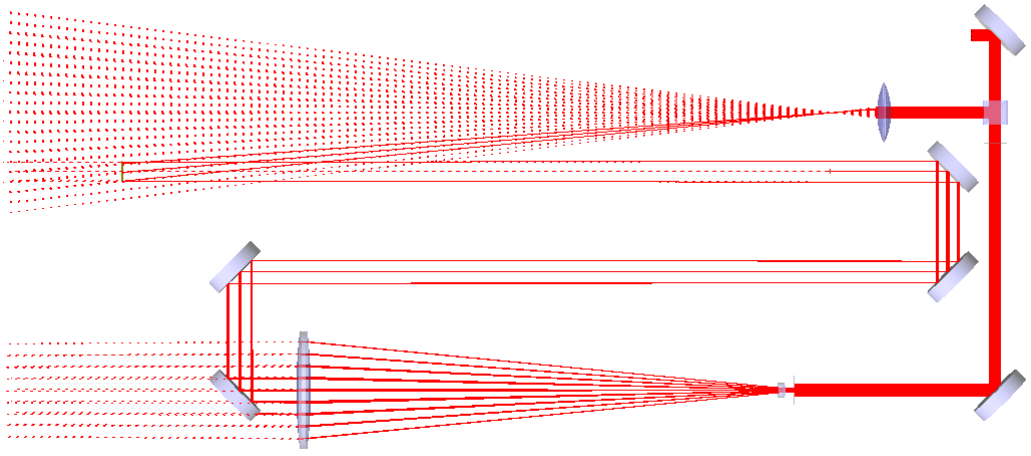

(b) FRED model of the full LFTDH interferometer.

FIGURE 4.23: The full LFTDH model.

4.3.2 Field Resampling Protocol

Once the new model was initialised, the spatial resolution and detector contrast of the full LFTDH simulation were characterised in the same way as the simple interferometer model, as per the methodology described in Section 4.2.4. However, examining the image of the contrast-detail phantom acquired with this system (Figure 4.24a) immediately revealed a problem.

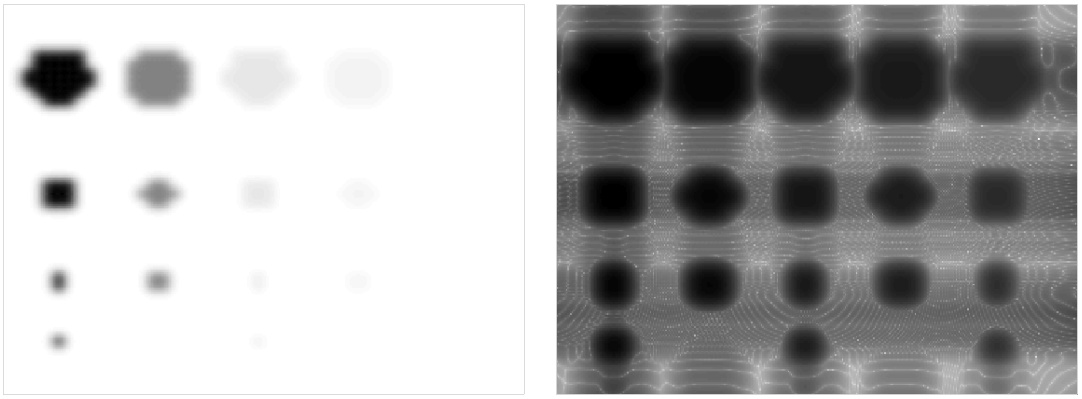

(a) Linear scale. (b) Log scale.

FIGURE 4.24: Undersampled contrast-detail phantom plots.

The dose-equivalent regions in the phantom should be most indistinguishable in the bottom-right corner and become steadily more visible towards the left, as the dose increases, or towards the top, as the spot radius increases. However, the bottom row of this image does not adhere to this pattern. This is illustrated more clearly in Figure 4.24b which shows the contrast-detail reconstruction on a log-display. On the log-intensity image, it can be seen that the regions of smallest radius representing 1 Gy, 0.1 Gy and 0.01 Gy are visible, but those equivalent to 0.5 Gy and 0.05 Gy are completely absent from the image.

In addition, the visible dose areas are clearly distorted. Some of the dose regions, for example A2 and B3, appear square instead of round. Others exhibit pinched borders and flattened sections on their extreme edges, as seen in the A1 and B2 voxels.

The source of this problem was hypothesised to be a poor distribution of rays modelling the laser beam as it propagated through the model. To test this theory, analysis surfaces were placed at the laser source, phantom entrance, and reference expander lens, and these surfaces were used to collect Gaussian Spot Size Diagrams (GSSDs). As discussed in Section 3.2.3, the GSSD analysis visualises each ray incident on the analysis surface as a point

with a ring around it representing the $1/e^2$ amplitude of the Gaussian beamlet. Comparison of these rings to their size at the laser source indicates the amount of divergence undergone by each beamlet. GSSDs collected at the laser source, phantom entrance, reference lens and CMOS are compared in Figures 4.25a through 4.25d respectively.

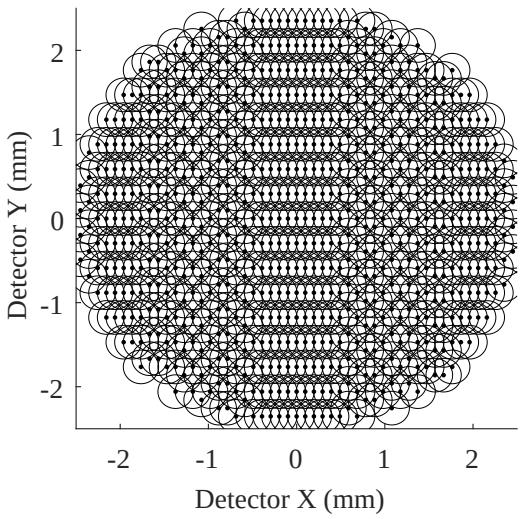

(a) Source GSSD.

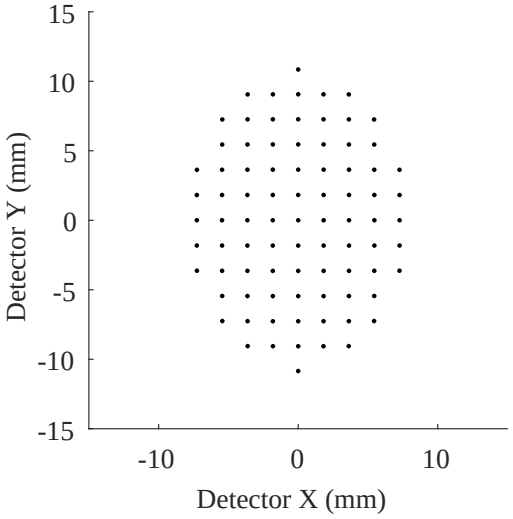

(b) Object beam GSSD at phantom entrance.

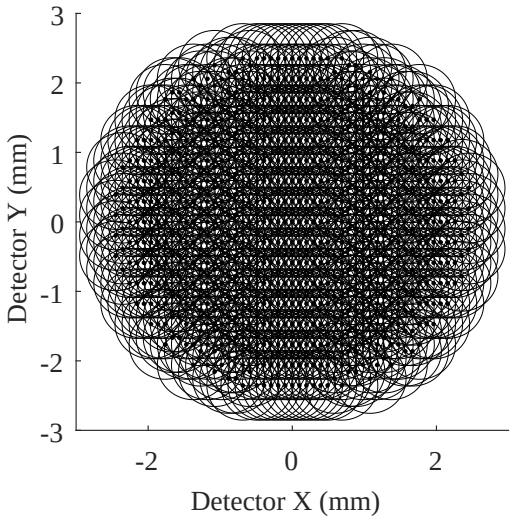

(c) Reference beam GSSD at beam expansion lens.

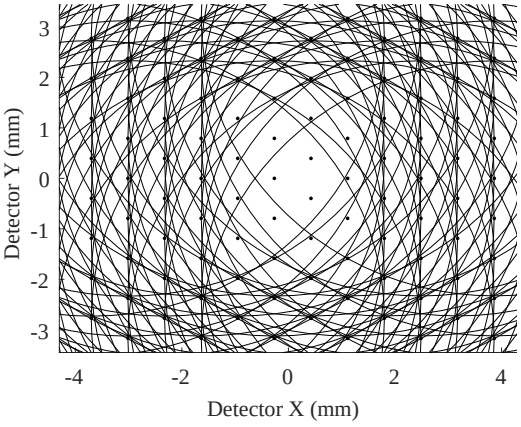

(d) Reference beam GSSD at CMOS.

The first GSSD appears as expected. The rays are clearly aligned along the grid within the circular boundary of the laser, and each is encircled by a small $1/e^2$ amplitude circle. In sharp contrast, the GSSD collected at the phantom entrance shows only points, with no $1/e^2$ amplitude circles visible inside the 20 mm^2 analysis region. This indicates that the beams have diverged so

much that their $1/e^2$ radii are larger than 20 mm, which obviously does not accurately represent the physical laser beam. Far fewer rays also appear in the GSSD acquired at the phantom; 85 rays are present at the phantom entrance, compared to 2053 in the GSSD acquired at the laser source.

This indicates that as the rays comprising the object beam traversed the many optics and long optical path in this interferometer model, the Gaussian beamlets diverged to the extent that they no longer provided an accurate representation of the object beam's wave field. This is corroborated by Figure 4.25c, the GSSD acquired of the reference beam at the focusing lens. Since this beam has traversed a much smaller path and only interfaced with one optical element, the low divergence of the original source beam is much better preserved.

The severe reduction in the ray count from the source to the phantom is responsible for the anomalous results in the object reconstruction. Examining the ray history reveals that none of the rays from the object beam interacted with either the 0.5 Gy or the 0.05 Gy dose areas during the simulation. This meant that these voxels did not appear in the reconstructed image, since they were not encoded in the hologram by any of the rays. The low number of rays traversing the phantom is also likely to be responsible for the distortion of some the visible dose areas. The geometric undersampling in these regions means that they appear in the reconstruction, but their borders are poorly represented.

Solving this problem necessitated the development of a field resampling protocol, configured as per the dialogue in FRED's 'Raytrace > Spatially Resample Field' menu GUI. The principles of field resampling are more fully discussed in Section 3.2.2. In brief, this technique entails resampling a wave field incident on an analysis surface and then generating a new ray from every pixel on the surface. In this way, the divergence of beams traversing long distances or interacting with optics can be controlled. Using this ray tracing technique, the object beam was resampled using analysis surfaces positioned at two problematic points, which are indicated as RSP1 and RSP2 in Figure 4.26 .

Although the reference beam was better-behaved throughout the optical system, it also required resampling. Since the reference rays diverged spherically from the focal point of the expansion lens, the number of rays incident on the CMOS was greatly reduced from the number leaving the beamsplitter. This is illustrated in the final GSSD, shown in Figure 4.25d, which plots the

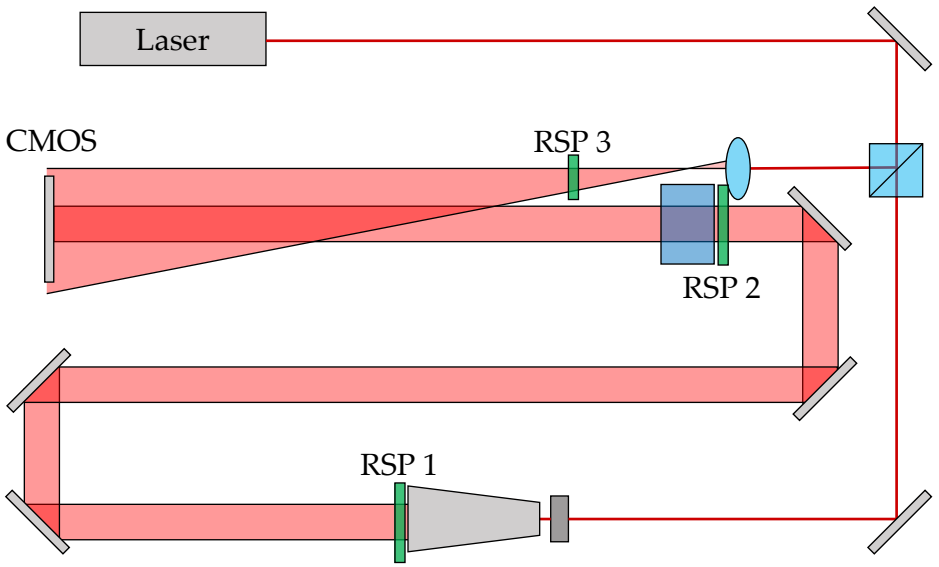

FIGURE 4.26: Log display of the phase unwrapped reconstruction of the contrast detail phantom.

distribution of reference beam rays incident on the CMOS. Out of the 2053 rays leaving the expansion lens, fewer than 100 reached the CMOS surface, and their $\frac{1}{e^2}$ amplitude radii increased dramatically from 0.5 mm at the lens to over 5 mm at the CMOS. Therefore, a single field resampling point (RSP3) was also added to the reference beam between the focus and CMOS. This resampling point was used to redirect the field, such that a higher density of rays in the field envelope around the CMOS were traced, while the rays in field regions which propagated away from the CMOS were halted.

Although field resampling can be conducted entirely through FRED's built-in GUI dialogues, doing so is prohibitively time consuming, especially for repeated trials. As such, the process was automated via FRED's scripting functionality.

4.3.3 Full LFTDH Model Characterisation Results

With the field resampling protocol implemented, the MTF, fencepost, and contrast-detail tests were re-conducted on the full LFTDH model. These trials were carried out as per the methodology described in Section 4.2.4 where the characterisation of the simple model was described.

Spatial Resolution

The MTF calculated for the full LFTDH configuration is plotted against MTF of the simple model. It can be seen that the MTF drops off considerably faster for the complex model, with a resolution limit of 34 lp/mm, compared to 47 lp/mm for the simple configuration. The MTF plot of the full system also contains more noise, particularly in the low-amplitude shoulder region. This is likley to be the result of aliasing effects or periodic noise in the interferogram.

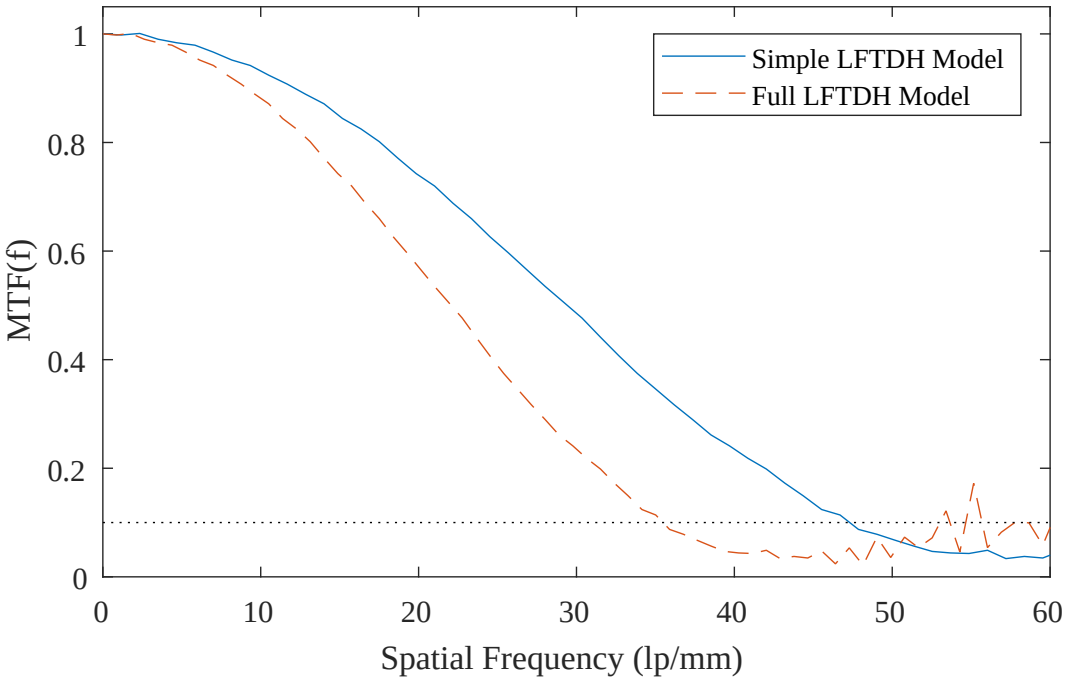

FIGURE 4.27: MTF of the full LFTDH Dosimeter.

A fencepost test was also conducted to assess the spatial resolution of the system, accounting for the phase unwrapping and other reconstruction algorithms. A pair of line profiles extracted from the reconstructed image of the fencepost phantom are shown in Figures 4.28a and 4.28b. From these profiles, it can be seen that the spatial resolution of the full LFTDH dosimeter including reconstruction steps was limited to 14 lp/mm.

The results of the contrast-detail test following the field resampling, shown in Figures 4.29a and 4.29b, indicate the success of the field resampling protocol when compared to the undersampled contrast-detail phantom shown in Figure 4.24a. The smallest 0.5 Gy dose region is once again visible, and the expected trend of continuous decrease in contrast with lower dose

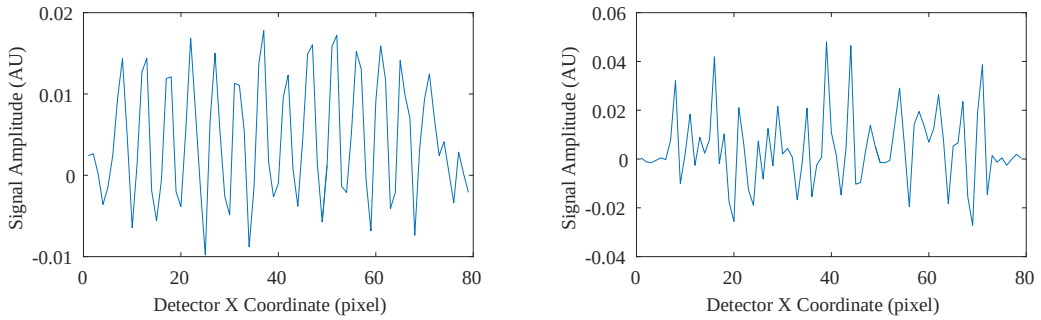

(a) 14 lp/mm region. (b) 15 lp/mm region.

FIGURE 4.28: Line profiles from full LFTDH dosimeter.

has been restored. In addition, the geometric distortions observed in Figure 4.24a have been eliminated.

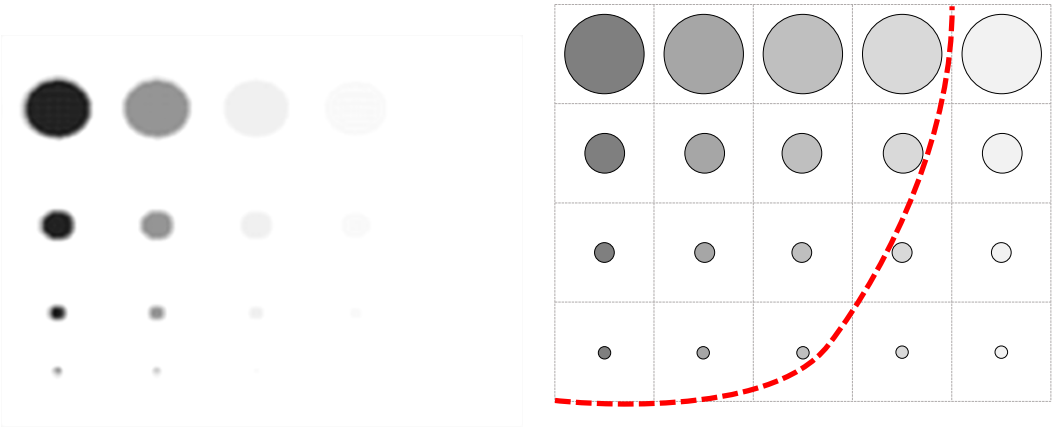

(a) Reconstructed contrast-detail phantom. (b) Plot indicating visible voxels.

FIGURE 4.29: Contrast detail plots from full LFTDH dosimeter.

Overall, the results of these characterisation tests are as expected. Due to the inclusion of more optics and a greater beamline length, the full LFTDH model performs slightly worse than the simple configuration in all respects, with a lower spatial resolution and a slightly lower contrast response. However, following implementation of the field resampling protocol, the full model has been shown to be capable of resolving clinically relevant dose distributions and geometric patterns. This configuration therefore represents a successful proof of concept that a realistic LFTDH model can be created in FRED. With this accomplished, this full LFTDH model can be used to assess whether FRED is capable of quantifying the impact of the uncertainties intrinsic to the prototype dosimeter.

Chapter 5

Case Studies in Modelling Environmental Perturbations

With a detailed model of the DHI dosimeter initialised and verified against existing experimental data, the aim of the next stage of research was to verify that FRED could be utilised to quantify major sources of uncertainty in the dosimeter. Although the scope of this project did not allow time to construct a detailed and holistic environmental model, several sources of uncertainty were chosen as case studies and measured to verify that such investigations could be undertaken in FRED.

As discussed in Section 2.4, Cavan and Meyer identified major sources of uncertainty in the prototype dosimeter to be atmospheric turbulence, mechanical vibration, heat expansion and heat diffusion [26].

Although heat diffusion was deemed to be a significant contributor to dosimetric uncertainty, the numerical methods for modelling it in the test cell are complex and can be computationally expensive [26]. Therefore, they are most effectively handled either via a commercial software package like COMSOL's Multiphysics Heat Transfer Module, or by creating a separate MATLAB or C++ module. In either case, a sensible and computationally efficient approach to including heat diffusion in the interferometer model will involve importing the results of external heat diffusion calculations into FRED, rather than implementing them within FRED's scripting environment. Due to the time investment required to accomplish this, investigating heat diffusion was deemed to be outside the scope of this research, and is recommended as future work for a longer-term project.

For each of the three uncertainty case studies, the virtual LFTDH dosimeter was altered to model the physical perturbations to the system as a result of

each uncertainty source. Next, holograms were captured across the parameter space of the variable or variables being perturbed in order to quantify their impact on the measured dose value or the system's spatial resolution, depending on which metric was more relevant to the uncertainty source being modelled.

5.1 Atmospheric Fluctuations

The refractive index of air is dependent on atmospheric temperature, pressure and relative humidity, all of which are prone to measurement error and spatio-temporal fluctuations. The prototype dosimeter is not airtight, so these fluctuations can cause changes in the refractive index of the air within the interferometer beamline. Since the reconstruction algorithms assume that the path length of the reference beam is constant and any change to the OPL of the object beam is due to dose administered within the test cell, these fluctuations in atmospheric refractive index can create significant error in the amount of dose measured by the interferometer.

Fluctuations in atmospheric pressure, temperature and humidity can stem from many sources. First, temperature and humidity within a building vary throughout the day, due to solar heating of the building surfaces and the daily dew cycle [82]. A human presence in the room, which is necessary during experimental preparation and for the administration of some source types, will also cause a steady increase to the local temperature and humidity. Movement of people or machinery in the room will cause air currents, generating pressure fluctuations on short timescales. Finally, many hospital environments, where most dosimetry is performed, are fitted with air conditioning or climate control units which cannot be disabled. These cause significant atmospheric fluctuations which occur on short timescales.

Although any fluctuation in the atmospheric refractive index is undesirable, in general those which occur on shorter timescales are more deleterious. For example, if the refractive index of the air within the interferometer beamline fluctuates in between reference and object hologram acquisitions, the assumptions underlying the reconstruction algorithms are compromised, so uncertainty is added to the dose due to errors in the reconstruction step, but the intrinsic noise of the measurement remains low. Contrastingly, if the atmospheric fluctuations occur on a timescale comparable to the camera's

exposure time, the interference pattern will be blurred, increasing noise to the point that the spatial and dose resolution of the system may be compromised. If uncontrolled, these small, short-timescale fluctuations can render the hologram reconstruction completely erroneous, and no object can be reconstructed.

5.1.1 Calculating the Refractive Index of Air

Currently, there is no analytical relationship between atmospheric parameters and the refractive index of air. Instead, there exist two equations, the Edlén and Ciddor models, which have been developed empirically using existing refractive index data [83, 84]. Outside extremes of atmospheric parameters, such as below freezing or very high humidity environments, there is little difference between the refractive indices produced by these equations. For the range of atmospheric conditions in which our dosimeter will be operated, the defect between the refractive indices produced by the Edlén and Ciddor equations is less than 10^{-10} [85]. For this reason, the Edlén equation was selected to calculate the refractive index for our model, since it is the simpler option. The version of the Edlén equation used here was updated most recently by Birch and Downs in 1993, with significant revision in 1994 [86, 87].

A MATLAB script, included in Appendix A.2, was created to carry out the Edlén calculations of atmospheric refractive index for given values of air pressure, temperature and humidity. This equation is evaluated in three stages. First, the refractivity of standard air at 15 °C and 1 atmosphere is calculated for the specified wavelength using the equation

$$(n-1)_s \times 10^8 = 8342.54 + \frac{2406147}{130-\sigma^2} + \frac{15998}{38.9-\sigma^2}, \tag{5.1}$$

where σ is the wavenumber of the light in micrometres, equal to the reciprocal of the wavelength $\frac{1}{\lambda}$.

The next stage calculates the defect in atmospheric refractivity due to non-standard temperature (T) and pressure (P):

$$(n-1)_{tp} = \frac{P(n-1)_s}{96095.43} \times \frac{1+10^{-8}(0.601-0.0972T)P}{1+0.0036610T}. \tag{5.2}$$

Lastly, the defect due to humidity (f) is factored into the final refractive index, n_{tpf}:

$$n_{tpf} - n_{tp} = -f \left[3.7345 - 0.0401\sigma^2\right] \times 10^{-10}. \tag{5.3}$$

The Edlén equation can also calculate the defect in refractive index due to the amount of carbon dioxide in the atmosphere [82]. However, this calculation was omitted from our model, since the defect due to this term is less than 10^{-9} across the reasonable range of carbon dioxide expected in a laboratory setting [85].

5.1.2 Simulating Long-timescale Atmospheric Fluctuations

The first experiments on atmospheric uncertainties measured the impact of long-timescale changes to each atmospheric property. In these trials, the refractive index of the atmosphere was adjusted homogeneously, and the impact of small-scale fluctuations was not considered.

Model Configuration

The average values and uncertainties of each parameter were set via a combination of measurements undertaken in our laboratories and literature research. These averages and their uncertainties are shown in Table 5.1.

Parameter	Mean Value	Uncertainty
Temperature	20 °C	1 °C
Pressure	101.325 kPa	0.01 kPa
Humidity	50%	2%

TABLE 5.1: Atmospheric parameters being adjusted and their uncertainties.

The MATLAB script created in the previous section was then used to calculate refractive index values across the parameter space of each of the above variables, while the other two were held constant at their average values. The results of these calculations are plotted in Figures 5.1a through 5.1c. It can be seen that over the selected uncertainty windows, the relationships are all close to linear and symmetric about the mean value. Therefore, a simple analysis could be conducted by selecting the refractive index values from each end of the range.

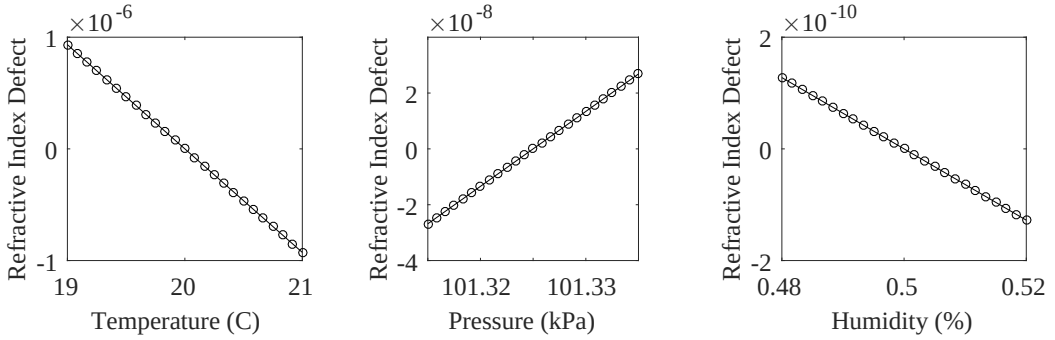

(a) Refractive index defect with ΔT.

(b) Refractive index defect with ΔP.

(c) Refractive index defect with ΔH.

In order to test the impact of each of these uncertainties on the dose detected by our interferometer, the refractive index values corresponding to the maximum and minimum of each atmospheric variable were taken from the above datasets. Maximum and minimum refractive index values were also calculated for the case where temperature, pressure and humidity were all allowed to vary. Finally, a reference atmospheric refractive index value was calculated for the case where all the values were set to their averages. These refractive index values are displayed in Table 5.2.

The results of the refractive index calculations are listed in Table 5.2. The parameter being changed is given in the first column, along with its value for each test and the calculated refractive index.

Parameter		Parameter Value	Refractive Index
Temperature	Min	19 °C	1.000272731479275
	Max	21 °C	1.000270871377762
Pressure	Min	101.315 kPa	1.000271771425499
	Max	101.325 kPa	1.000271825097028
Humidity	Min	48%	1.000271798388954
	Max	52%	1.000271798133571
All	Min	—	1.000270697986413
	Max	—	1.000271898261263
None (Reference)	—	—	1.000271798261263

TABLE 5.2: Atmospheric refractive index for the maximum and minimum values of each atmospheric parameter.

A new phantom, shown in Figure 5.2, was configured to represent a circular 1 Gy dose region of radius 1 mm. Using the full LFTDH dosimeter initialised in the last chapter, a hologram was collected of this phantom with

the refractive index of the 'Air' material set to the unperturbed atmosphere value. Next, the refractive index value of the 'Air' material was changed in turn to the minimum and maximum refractive index values associated with each of the the atmospheric parameters. A reference hologram of the unirradiated water phantom, and an object hologram of the 1 Gy dose region were then collected for each of these atmospheric refractive indices using the 'ExportHologram' FRED subroutine.

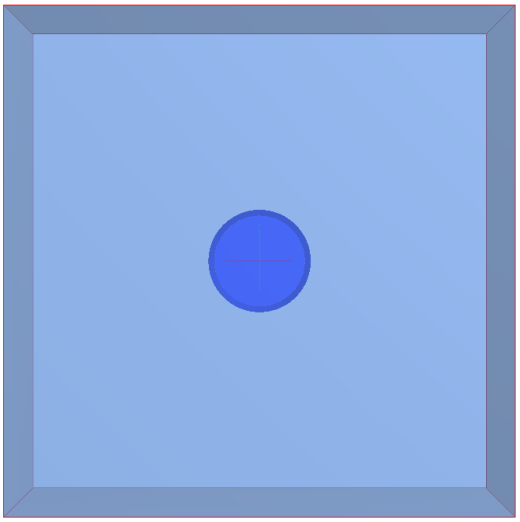

FIGURE 5.2: FRED model of the flat dose phantom used in uncertainty analysis tests. The centre volume is 1 mm in radius and represents a dose of 1 Gy, while the surrounding cube has the refractive index of water at room temperature (20 °C).

Each of the object holograms was reconstructed against the reference state to obtain a two-dimensional map of the dose measured across the test cell. Each perturbed-state dose map was subtracted from the unperturbed reference dose measurement, yielding a dose-defect map for each perturbed state. The values inside the circular dose region in each perturbed-state map were then averaged to obtain an overall dose-defect measurement corresponding to each perturbed refractive index. The average dose defects were then compared as percentage uncertainties of the actual 1 Gy dose and the percentage uncertainties corresponding to the maximum and minimum values of each parameter were averaged to yield the final percentage uncertainty induced in the dose measurement by each parameter. This final step was taken in order to account for possible asymmetries in the relationship between atmospheric refractive index and measured dose.

The above procedure was repeated using the maximum and minimum refractive index values corresponding to the system with three degrees of

freedom, where all atmospheric parameters were allowed to vary. This gives a final worst-case estimate for the total uncertainty due to all the atmospheric parameters.

5.1.3 Simulating Short-timescale Atmospheric Fluctuations

The impact of short-timescale fluctuations on the doses measured by the interferometer were also quantified. Fluctuations of this nature are typically induced by draughts, people moving about the laboratory, and air conditioning units. In contrast to the larger fluctuations explored in the previous section, these perturbations occur on small length scales, such that different parts of the beamline are affected unevenly, and they occur on millisecond timescales, quickly enough to cause blurring in the holograms as they are captured.

Model Configuration

The dosimeter used in the previous section was updated to include a voxel-based atmosphere. Populating the entire atmosphere uniformly with voxels was the simplest method, so it was the approach initially taken. However, this methodology led to two problems. First, it was inefficient, as it resulted in many unused voxels being created far outside the beam path, which rays would never traverse. Second, raytracing errors occurred at points where the voxels clipped inside the optical elements, as shown in Figure 5.3. This was due to the discrepancy between the material comprising the voxel (perturbed air), and the immersion material of the optic (unperturbed air). When this occurred, FRED's raytrace function encountered a critical error, causing a failure of the 'ExportHologram' subroutine.

In order to avoid these issues, a more nuanced approach was taken. The beamline of the interferometer was roughly demarcated with element primitive blocks, as shown in the schematic displayed in Figure 5.4a. These blocks were added using the FRED graphical design environment, and were assigned the coating property of 'Transmit' and the 'Allow All' raytrace control property, such that they had no optical effect on the source rays being traced. These bounding volumes were assigned the keyword 'AtmosphereBounds' so that they could be easily retrieved using FRED's keyword search function in the scripting interface.

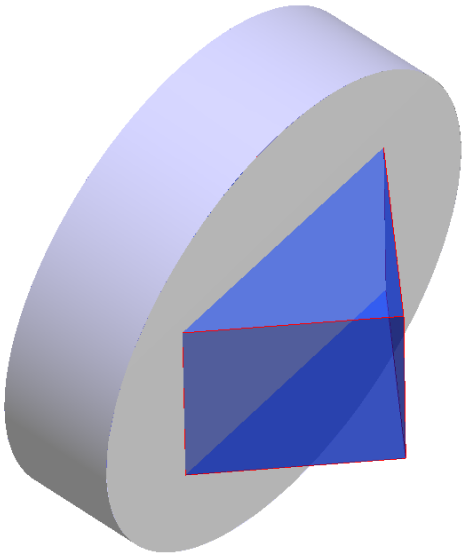

FIGURE 5.3: Example of error-inducing voxel clipping.

Once the atmospheric bounds were configured, the 'PopulateAtmosphere' script, included in Appendix B.2, was used to populate each of them with cubic voxels. The voxel size and the inter-voxel buffer width were specified by the user. Each of the atmospheric bounding boxes was then filled with voxels as per its outer length, width and height dimensions, such that none of the voxels protruded beyond the bounding boxes, as shown in Figure 5.4b. Each voxel was assigned the 'Voxel' keyword so that their node numbers could be retrieved in order to programmatically assign their refractive indices.

It is important to note that inclusion of a small buffer between voxels was necessary to avoid the raytracing errors discussed above with respect to air voxels clipping into optical elements. The atmospheric voxels could be configured without a separation buffer, but each face would need to be initialised with the correct glass and immersion materials to avoid these raytracing errors.

As part of the voxel creation step, the refractive index of each cube was perturbed with the 'PerturbVoxel' FRED script, included in Appendix B.3. This script allowed the user to specify average values for each atmospheric parameter (temperature, pressure and humidity) and the uncertainty of each parameter. Each voxel was assigned a random air pressure, temperature and humidity using a Gaussian probability model for the parameter value,

$$Pr(x) = \frac{1}{\sqrt{2\pi\sigma^2}} e^{\frac{(x-\mu)^2}{2\sigma^2}} \tag{5.4}$$

where the standard deviation, σ, was equal to the uncertainty in the parameter and the mean μ was equal to the average parameter value. The randomly assigned temperature, pressure and humidity values were used as inputs in the 'RefIndCalc' FRED function, and the refractive index of the voxel was returned by the script. A new material was programmatically created for each voxel to store this refractive index value, and the material was assigned to its corresponding voxel.

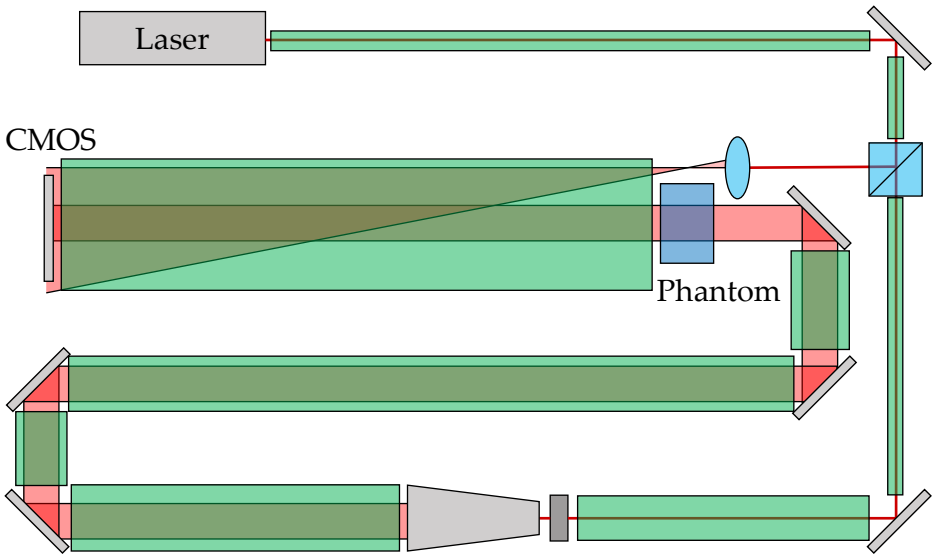

(a) Schematic of the LFTDH dosimeter, where the green boxes indicate the atmosphere bounding boxes to be filled with air voxels.

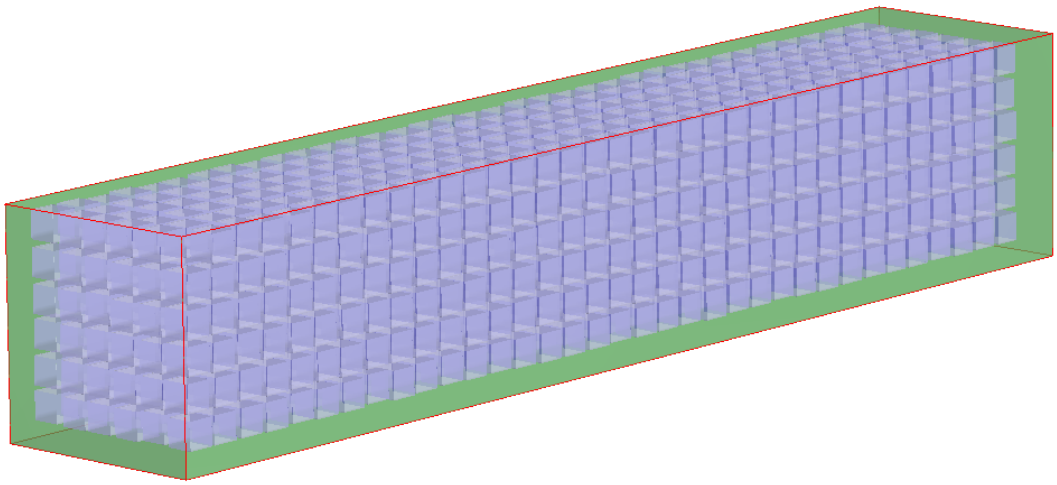

(b) FRED screenshot of one of the bounding boxes filled with air voxels. Each voxel has a different refractive index value.

FIGURE 5.4: Diagrams illustrating the air voxel creation methodology used in the final iteration of the 'PopulateAtmosphere' script.

Hologram Acquisition

With the atmospheric voxels initialised, hologram acquisition in a draughty environment with short-timescale atmospheric fluctuations was modelled. In order to mimic these perturbations over the Pixelink camera's minimum exposure time of 40 ms, a time-average hologram capture subroutine was implemented in FRED.

This hologram capture code was similar in structure to the 'ExportHolograms' subroutine discussed in Chapter 4. In addition to the basic hologram export functionality, however, it also implemented the 'PerturbAtmosphere' function described above to randomise the refractive index of all the atmospheric voxels prior to measuring the interference pattern. An integer 'expTime' equal to the exposure time of the simulated hologram in milliseconds was specified by the user and the voxel perturbation, irradiance measurement, and export steps were executed in a loop incremented 'expTime' times, and a hologram pair for each perturbation was exported. Each of these image sets was then averaged using MATLAB to yield the final time-averaged reference and object holograms. This time-averaging process was implemented to approximate the blurring of the intensity pattern captured by the CMOS due to the simulated atmospheric fluctuations.

This time-average methodology was used to capture hologram sets of the fencepost, slant-edge, and contrast-detail phantoms. These images were reconstructed and used to compare the spatial and dose resolution of the system to that of the unperturbed full LFTDH system.

5.2 Heat Expansion

Heat expansion was also factored into the model to account for discrepancies in the spacing of the optical components due to changes in the ambient temperature. Similar to the homogeneous refractive index changes discussed above, heat expansion occurs on a timescale considerably longer than the CMOS acquisition time, so it is unlikely to cause blurring in the holograms. However, it can cause errors in the measured dose when an object hologram is being compared to a reference taken at a different time, or a significant amount of time elapses over the course of a measurement series.

5.2.1 Model Configuration

In order to incorporate heat expansion into the full LFTDH model, each of the optical components, including the laser and the phantom were assigned the keyword 'OpticalElement' so that their node numbers could be recalled programmatically. A new FRED function, 'HeatExpandOptic' was created which recalled these node numbers and edited their 'Position/Orientation' property by appending a new 'Shift' operation which translated the optic along the x, y, and z axes by an amount corresponding to the amount of heat expansion undergone.

Calculating the translation distances for each optic was simplified by the fact that the optical board and posts upon which the interferometer components are mounted are all made of aluminium. Therefore, for a given temperature perturbation, ΔT, the amount of translation, ΔL, in each dimension is given by

$$\frac{\Delta L}{L} = 23.1 \Delta T \tag{5.5}$$

where $23.1 \times 10^{-6}\,\mathrm{K}^{-1}$ is the thermal expansion coefficient of the aluminium and L is the linear dimension the expanding material [88].

Finally, the heat expansion induced in the water phantom itself had to be calculated. As the path length traversed by the object beam through the phantom is an integral part of the dose calculation, the amount of expansion induced in the perspex cell by our selected temperature range of 15 °C to 25 °C was also included in the model. The alteration of the water block dimensions were achieved exactly as for the translation distance calculated above, except that the thermal expansion coefficient of Perspex, $69\,\mathrm{K}^{-1}$, was used in place of that for aluminium [88].

To test the impact of heat expansion upon the measured dose, a reference hologram was collected of the same flat 1 Gy dose region used in Section 5.1.2 with the optics at their default positions, which were considered to occur at 20 °C. An object hologram was then collected of the same phantom with the optic positions modified by heat expansion corresponding to temperatures of 15 °C ($\Delta T = -5$) and 25 °C ($\Delta T = 5$), which were taken as the upper and lower extremes of expected indoor temperatures.

5.3 Mechanical Vibration

Mechanical vibrations were the final uncertainty source examined in this case study. They can be induced by any source of vibration occurring in the vicinity of the dosimeter, including mechanical equipment, computer exhaust fans, traffic and construction. These factors are all common in university and hospital laboratory environments, so these vibrations were identified as a serious source of uncertainty in the dose measurements by Cavan et al. [26]. These vibrations minutely alter the position and orientation of each of the optical components, and occur on extremely short timescales. They therefore have the potential to cause blurring in the acquired holograms, similar to the short-timescale atmospheric fluctuations discussed in Section 5.1.3.

The amplitude and frequency of these mechanical vibrations was estimated via figures obtained from literature [89]. Table 5.3 reviews the vibration types which were deemed relevant to locations where our interferometer was likely to be operated. Each vibration source is tabulated with the amplitude and frequency of the oscillations it induces.

Source	Amplitude	Average Frequency
Machinery	1×10^{-2} mm	105 Hz
Traffic	1×10^{-1} mm	50 Hz
Acoustic	1×10^{-3} mm	75 Hz
Building Resonance	1 mm	10 Hz
Building Sway	1 mm	1 Hz
Motors	1×10^{-2} Hz	275 Hz

TABLE 5.3: Sources of vibrational noise and their estimated amplitudes and uncertainties.

5.3.1 Model Configuration

A new FRED subroutine, 'VibrateOptics' was created in order to introduce mechanical vibrations to the full LFTDH dosimeter model. The code for this subroutine is included in Appendix B.5. This function takes two inputs, 'opticH' and 'amplitudes'. The 'opticH' variable is set to the height of the posts on which the optics are mounted, and 'amplitudes' is a vector in which the amplitude of every vibration being investigated is stored. If 'amplitudes' is left unassigned, it will default to a vector containing the vibrational amplitudes listed in Table 5.3.

In order to account for the worst possible scenario of mechanical vibration, in which all optics are vibrating randomly with respect to one another, the 'VibrateOptic' function was applied to each element with the 'OpticalElement' keyword separately, and a random translation distance between zero and the total vibration amplitude was assigned to the optic for each axis. A final rotation operation was then calculated, in which the orientation of the optic in the x-y, x-z and y-z planes was perturbed according to its height and its translation distance along the relevant axis. Each optical element therefore had six degrees of freedom over which the mechanical vibrations were modelled. These translations and rotations were applied to each optic by appending a 'Shift' and 'Rotate' operation to each of their Position/Orientation parameters respectively.

The time-averaged hologram acquisition code developed in Section 5.1.3 was then used to mimic the blurring of the interference pattern due to these short-timescale mechanical vibrations. Hologram sets were captured of the system in its reference state, the contrast-detail phantom, the fencepost phantom and the slant-edge phantom. Forty holograms were captured in each set to simulate a 40 ms exposure time. These were analysed as per the methodology outlined in Section 4.2.4 in order to assess the spatial resolution and contrast detection of the system under mechanical vibration so that it could be compared to other simulation states.

5.4 Results

The results of the above uncertainty investigations were compared to one another and to the full LFTDH dosimeter in its unperturbed state in order to assess the relative impact of each uncertainty type. The long-timescale fluctuations (homogeneous atmosphere change and heat expansion) and the short-timescale fluctuations (turbulent atmospheric changes and vibration) are grouped together respectively for analysis, since each pair produced similar effects on the dosimeter.

5.4.1 Long-timescale Fluctuations

The reconstruction of the 1 Gy dose area with no atmospheric perturbation is shown in Figure 5.5a and dose-defect maps corresponding to each of the

atmospheric parameters are shown in Figures 5.5b through 5.5d.

The holograms of each of the perturbed atmospheric refractive index states were reconstructed using the unperturbed state as a reference. The average absolute error measured from each of the dose-defect maps and the resulting final uncertainties for each parameter are listed in Table 5.4.

Parameter		Dose Defect (Gy)	Uncertainty (%)
Temperature	Min	1.4048×10^{-4}	1.3996×10^{-2}
	Max	1.3943×10^{-4}	
Pressure	Min	4.0306×10^{-6}	4.0296×10^{-4}
	Max	4.0286×10^{-6}	
Humidity	Min	1.3803×10^{-8}	1.4986×10^{-6}
	Max	1.6169×10^{-8}	
All	Min	1.6549×10^{-4}	1.5799×10^{-2}
	Max	1.5048×10^{-4}	

TABLE 5.4: Dose defects and percentage uncertainties generated by each atmospheric parameter.

It can be seen that fluctuations in air temperature were the most significant source of error, contributing roughly 0.014 % uncertainty to the dose measurement. Next, the fluctuations in atmospheric pressure were found to contribute an uncertainty of 4×10^{-4} % and fluctuations in humidity were found to contribute an uncertainty of 1.5×10^{-6} % to the dose measured by our interferometer. Combined, the uncertainty due to all the atmospheric parameters amounts to less than 0.016 % error in the dose measurement. According to our simulations, long-timescale atmospheric changes are therefore a relatively insignificant source of uncertainty in the dosimeter. Temperature is the most significant contribution to the uncertainty by two orders of magnitude, so controlling the ambient temperature during trials should be the highest priority out of these atmospheric variables. Geometric adjustments, addressed in Chapter 6, can also be undertaken to reduce the impact of these atmospheric fluctuations.

The same flat-dose hologram pairs were acquired using the interferometer subject to heat expansion. They were reconstructed into dose-defect maps, and the same averaging process was applied to yield the extracted dose defects and percentage uncertainties listed in Table 5.5. An example of the dose defect map is shown in Figure 5.5e, alongside those from the atmospheric analyses.

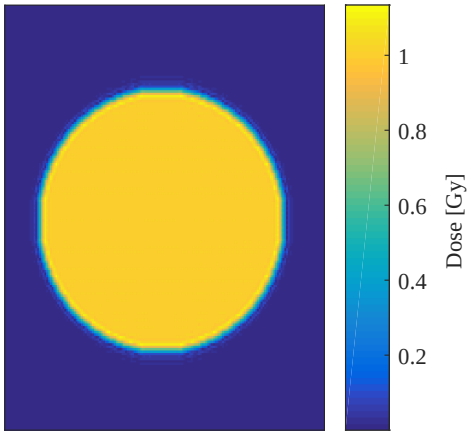

(a) Reconstruction of 1 Gy flat dose phantom.

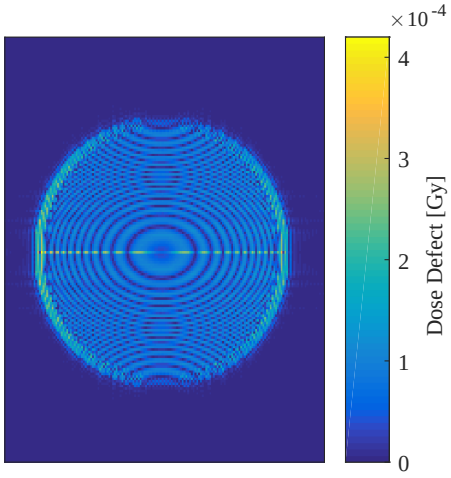

(b) Dose-defect map for the maximum temperature state.

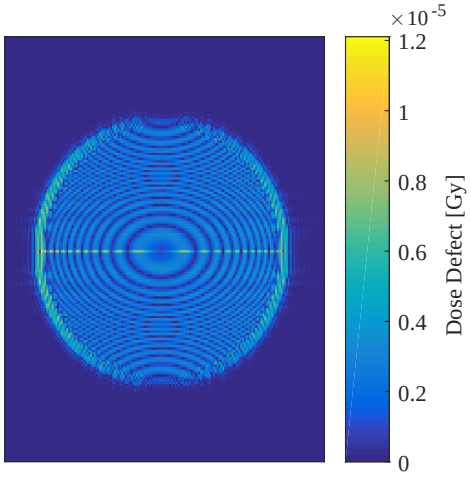

(c) Dose-defect map for the maximum pressure state.

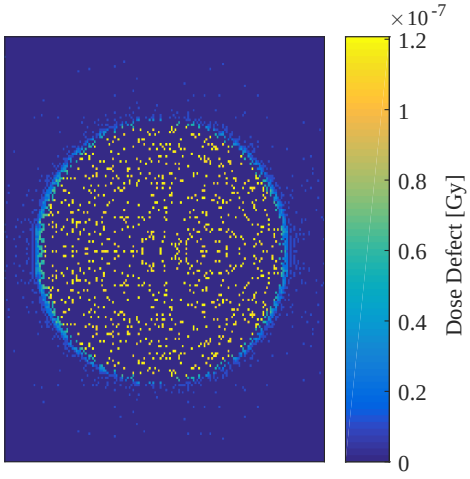

(d) Dose-defect map for the maximum humidity state.

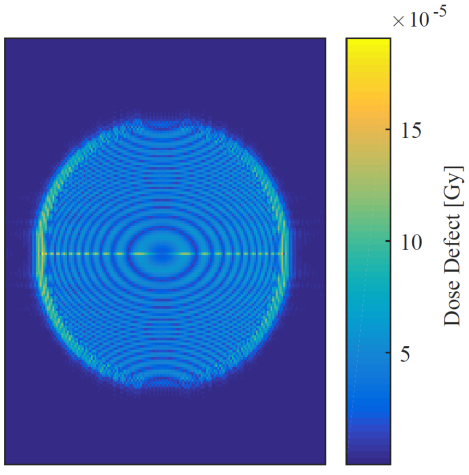

(e) Dose-defect map for the heat-expanded state.

FIGURE 5.5: Dose and dose defect reconstructions from perturbations to the full LFTDH model.

Temperature	Change	Dose Defect (Gy)	Uncertainty (%)
15 °C	5 °C	3.0028×10^{-5}	3.0245×10^{-3}
25 °C	−5 °C	3.0462×10^{-5}	

TABLE 5.5: Dose defects and percentage uncertainties generated by heat expansion.

According to our simulations, heat expansion contributed far less error to the final dose measurement than atmospheric uncertainty. Heat expansion was found to generate a roughly 0.003 % error in the average measured dose. This means that the uncertainty contribution of heat expansion is a full order of magnitude lower than the uncertainty induced by the combined action of all the atmospheric parameters.

Dose-defect maps from the heat-expanded state and the perturbed-atmosphere states are shown in Figure 5.5. This shows that, as predicted, these sources of uncertainty manifested in similar ways in the results of these trials. Both exhibit symmetric, circular interference fringes, consistent with an unaccounted-for phase shift in one or both of the interfering beams. This is a sensible result, since both perturbations cause a drift in the optical path length being traversed by the reference and object beams.

The prototype dosimeter is currently configured with the priority of fitting all the optical components onto a 250 ×750 mm breadboard, resulting in very unequal reference and object beams path lengths. It is important to note that as per Equation 5.6

$$\Delta OPL = n_1 d_1 - n_2 d_2 \tag{5.6}$$

the amount of drift between the reference and object optical path lengths due to atmospheric refractive index change and heat expansion is proportional to this geometric path length differential. Therefore equalising these beam path lengths is a potential method of mitigating these uncertainties, which will be discussed in the next chapter.

5.4.2 Short-timescale Fluctuations

Figure 5.6a shows an example of a time-averaged hologram obtained using the methodology created in Section 5.1.3. This image is contrasted with a

hologram collected in the previous chapter using the unperturbed dosimeter (Figure 5.6c) and a hologram collected experimentally by Cavan et al. (Figure 5.6e). This comparison shows that the atmospheric perturbation and averaging process produced a blurred hologram which is more similar to the experimental image than the noiseless simulation. This was taken to be an indication that the time-averaged hologram collection procedure successfully approximated environmental noise.

This comparison is reinforced by examining the interferograms produced by each of these methods. Each of the displayed holograms was reconstructed against its reference pair with no Gaussian noise added to produce the interferograms shown in Figures 5.6b, 5.6d and 5.6f. The interferogram produced under simulated atmospheric perturbation is much closer in appearance to the experimental hologram than the highly artefacted interferogram obtained using an unperturbed simulation.

Once the hologram averaging process was completed, modulation transfer functions were calculated as per the methodology outlined in Section 4.2.4 for the dosimeter system using the images of slant-edged phantoms acquired during the atmospheric turbulence and mechanical vibration simulations respectfully. These MTFs are shown in Figure 5.7, plotted alongside the MTF obtained for the uncertainty-free interferometer of the same configuration. This plot shows that the upper estimate of the unperturbed dosimeter's resolution limit was 34 lp/mm. Simulating mechanical vibrations reduced this limit to 22 lp/mm, and introducing atmospheric noise further reduced it to 17 lp/mm, half of its original best-case value.

The fencepost image series collected under each uncertainty regime were also averaged and reconstructed using the same methodology outlined in the previous Chapter. These images were separated into their different spatial frequency sectors, to provide a subjective measure of the spatial resolving power of the system including phase unwrapper and reconstruction algorithms. Average dose profiles from just under and over these spatial resolution limits are shown for the atmospheric uncertainties in Figures 5.8a and 5.8b, and for the mechanical vibrations in Figures 5.8c and 5.8d. The spatial resolving power of the system including phase unwrapping decreased dramatically, from 14 lp/mm for the uncertainty-free dosimeter to 7 lp/mm for the dosimeter undergoing mechanical vibrations and 5 lp/mm when atmospheric turbulence is included.

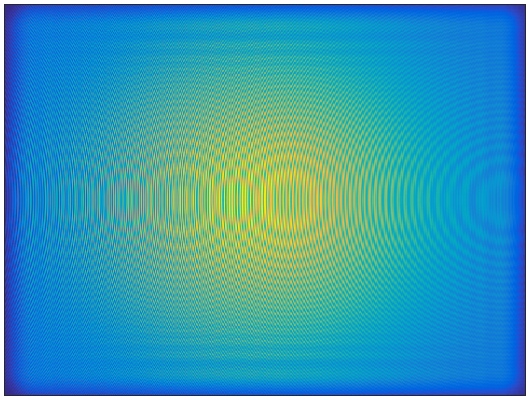

(a) Time-averaged simulated hologram.

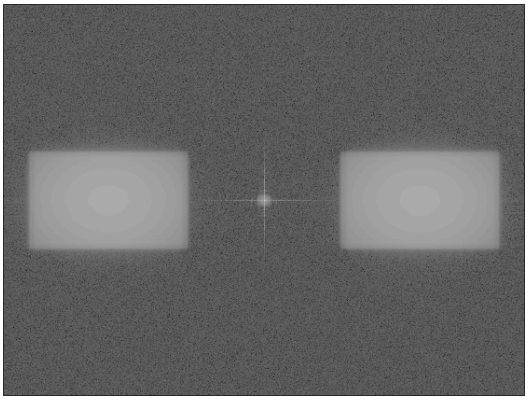

(b) Time-averaged simulated interferogram.

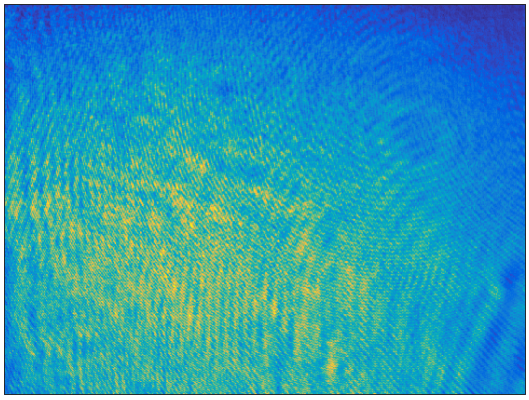

(c) Experimentally acquired hologram.

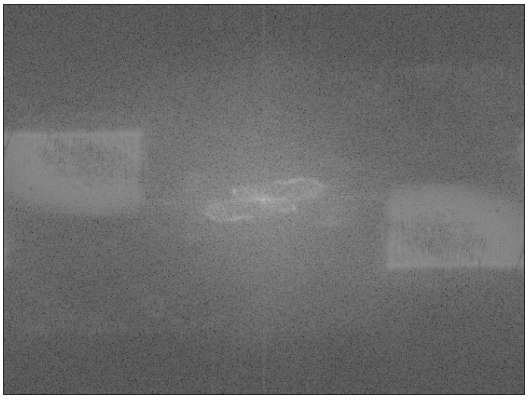

(d) Experimentally acquired interferogram.

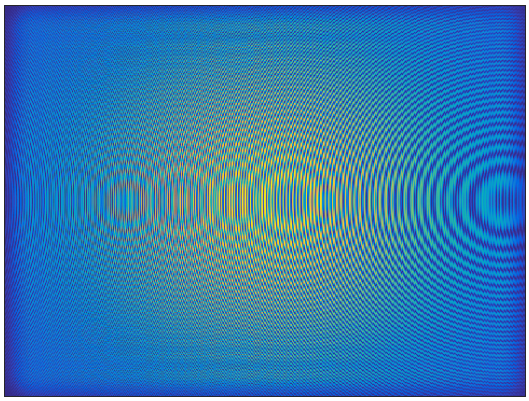

(e) Simulated noiseless hologram.

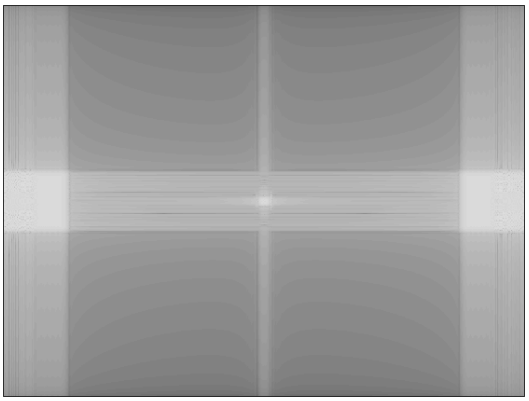

(f) Simulated noiseless interferogram.

FIGURE 5.6: Comparison of holograms and interferograms acquired under different conditions.

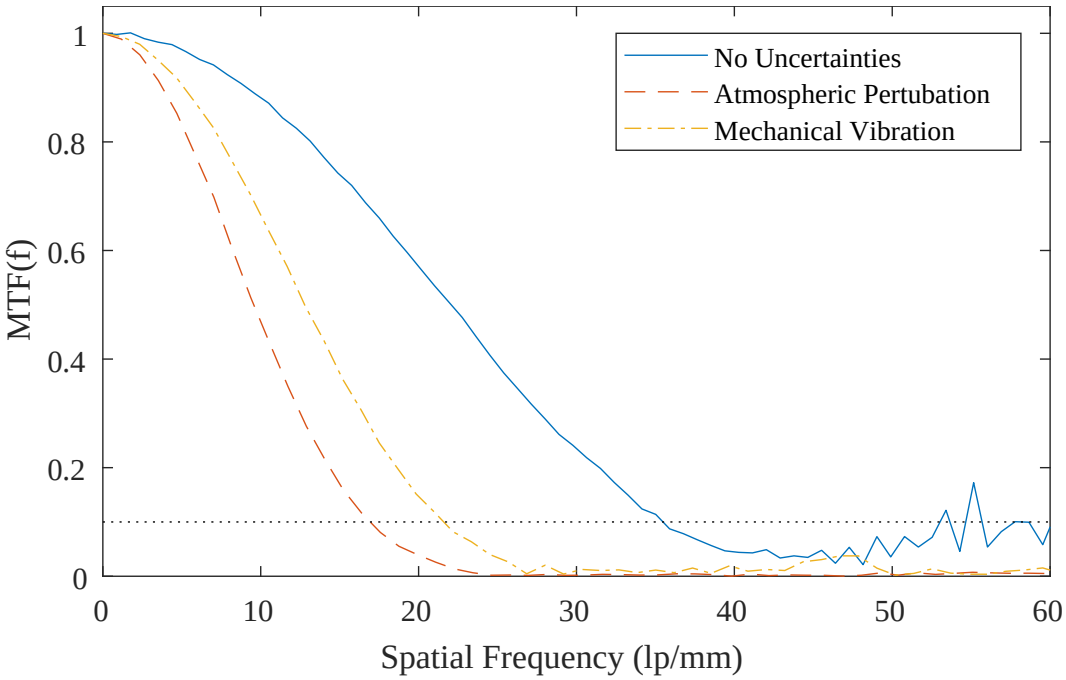

FIGURE 5.7: MTF of the full LFTDH dosimeter under different conditions.

Finally, the contrast-detail images were unwrapped and plotted. These showed a similar degradation in signal, which can be seen on the contrast-detail plots for atmospheric (Figure 5.9b) and vibrational (Figure 5.9d) uncertainties. None of the 0.05 Gy dose voxels are visible when atmospheric uncertainties are factored in and although more voxels are visible when vibrational uncertainties are applied instead, contrast-detail resolution is considerably worse than for the full LFTDH system with no uncertainties.

These results are as expected based on the theory of interferometers and Cavan's observations. Mechanical vibration and atmospheric turbulence were observed to be the two most challenging obstacles to accurate dosimetry during the experimental work conducted on the prototype dosimeter [26]. Introducing vibrations and atmospheric uncertainties into our model has decreased the spatial resolving power of the system by at least half and has severely compromised the contrast-detail resolution of our model. However, this definitive negative impact upon the image quality of our dosimeter is a success for this research. Our research aim is to verify that FRED is capable of modelling the DHI dosimeter and show that it is possible to model experimental uncertainties which pose barriers to refinement of the prototype. This aim has been achieved, and FRED has been shown to be capable of simulating experimental uncertainty sources via its scripting interface.

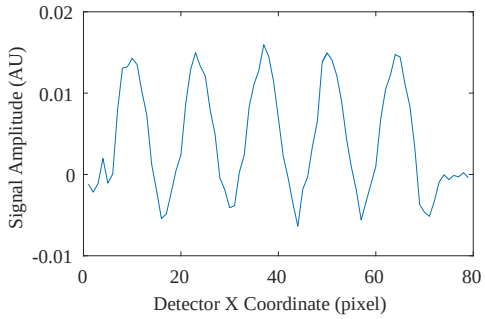

(a) 5 lp/mm region from atmospheric uncertainty simulation.

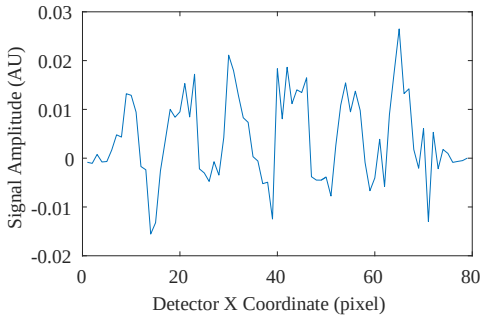

(b) 6 lp/mm region from atmospheric uncertainty simulation.

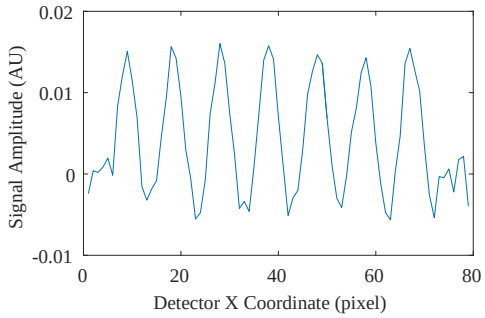

(c) 7 lp/mm region from mechanical uncertainty simulation.

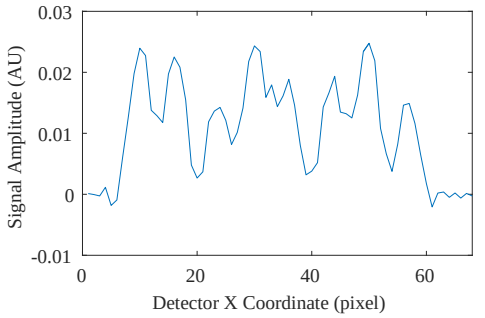

(d) 8 lp/mm region from mechanical uncertainty simulation.

FIGURE 5.8: Comparison of line profiles from atmospheric and mechanical uncertainty simulations.

(a) 5 lp/mm from atmospheric uncertainty simulation.

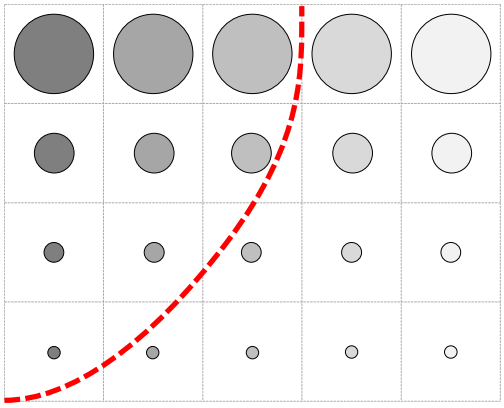

(b) 6 lp/mm from atmospheric uncertainty simulation.

(c) 7 lp/mm from mechanical uncertainty simulation.

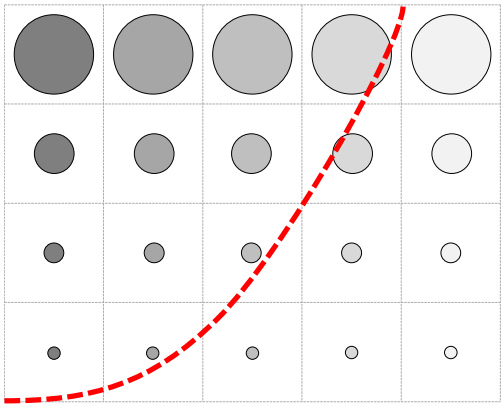

(d) 8 lp/mm from mechanical uncertainty simulation.

FIGURE 5.9: Comparison of contrast-detail results from atmospheric and mechanical uncertainty simulations.

Chapter 6

Case Studies in Virtual Dosimeter Refinement

Our final requirement for FRED was that it be capable of handling virtual refinement of the prototype dosimeter. This is a broad condition, as optimisation can be accomplished in a myriad of ways. Due to time constraints, the research aims for this project are limited to assessing the viability of FRED as a modelling tool. Completely optimising the system was thus outside the scope of the research.

In lieu of fully optimising the system, a case study was conducted in optimising the dosimeter's geometry. First, the path lengths of the object and reference beams were equalised, and the impact of atmospheric and mechanical uncertainty on the dosimetric error were retested. The dosimeter was then miniaturised and the impact of these uncertainties on the spatial resolution and contrast-detail tests were remeasured. The results were compared to those obtained in the previous chapter in order to gauge the degree of improvement in uncertainty due to these geometric changes.

6.1 Path Length Equalisation

One of the simplest techniques for improving interferometer performance is to equalise the path lengths of the reference and object beams. Figure 6.1 shows the schematic of the current interferometer configuration, from which the highly unequal reference and object path lengths can be observed. This large path inequality will increase the error from long-timescale atmospheric fluctuations and heat expansion, since both of these phenomena change the

OPL of a beam proportional to the length of its path. Therefore, equalising the object and reference beam path lengths will reduce the extra ΔOPL between the object and reference beams, reducing the error in the final measured dose.

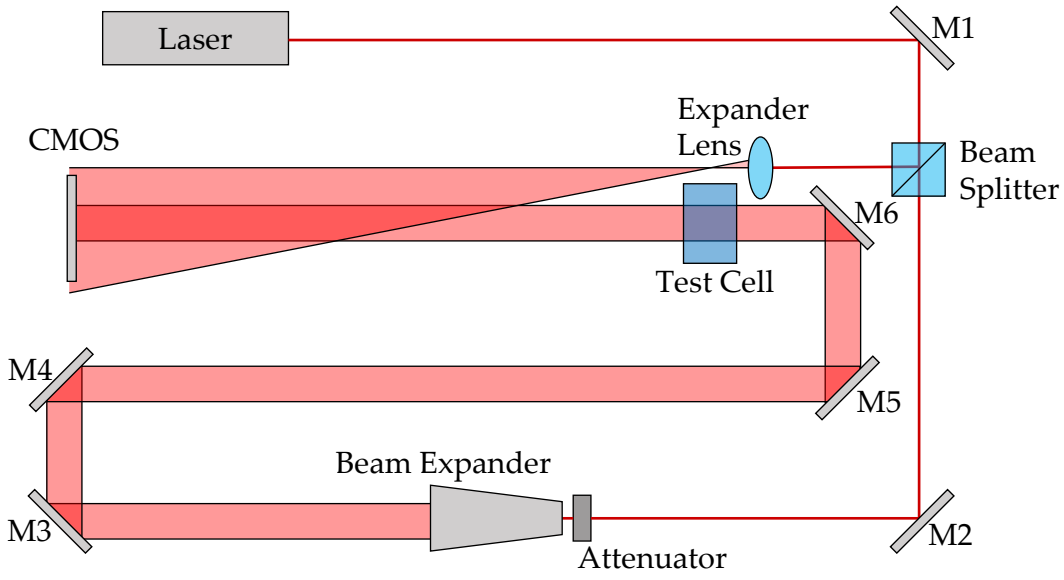

FIGURE 6.1: Schematic of the prototype interferometer design.

6.1.1 Model Configuration

First, the 'MeasurePathLengths' function was created in FRED to measure the path lengths of the beamlines. This was accomplished using the single-ray trace command in order to trace a ray on the optical axis and query the distance travelled between every surface it interfaced with. The total geometric path length was totalled from each of these measurements in turn.

The dosimeter model was manually altered to a configuration with more equal object and reference beamline lengths, as shown in Figure 6.2. The reference and object path lengths were then equalised using FRED's merit function optimisation tools. Merit function optimisation in FRED is conducted by defining an aberration function which specifies the quantity being evaluated, a weighting factor to determine its significance in the optimisation, and the target value for the evaluated quantity. Any number of aberration scripts can

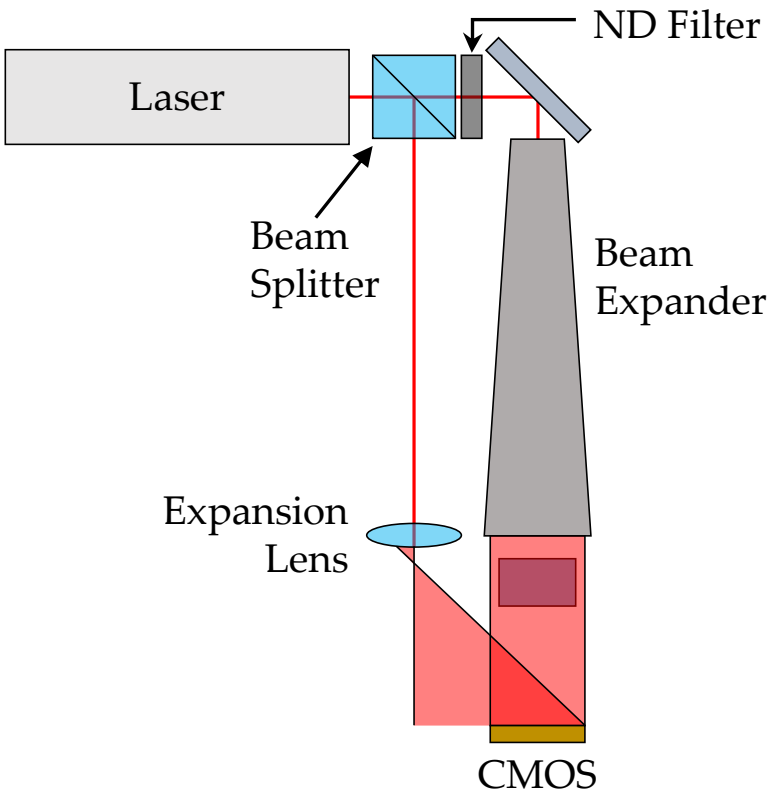

FIGURE 6.2: Schematic of the reconfigured dosimeter with equalised object and reference arm lengths.

then be combined to calculate a merit function as per the equation

$$MF = \sum w_n(A_n - T_n)\,, \tag{6.1}$$

where w_n is the weighting factor, A_n is the calculated value of the aberration, and T_n is the target value for the aberration. By this equation, it can be seen that a lower merit function indicates a better-optimised system.

In order to equalise the path lengths of the object and reference beams, several merit functions were used to control critical inter-optic distances. For example, a function was used to ensure that the spacing between the test cell and the object mirror was always greater than the length of the beam expander. In this way, crucial parameters were held fast while the beam paths were equalised using a custom user-scripted aberration function which calculated the path length difference ΔPL between the object and reference beams using the 'MeasurePathLengths' script.

The independent variables for the merit function optimisation were the coordinates of the turning mirrors. These were adjusted for each iteration of the optimisation, and the positions of the beam expander, lens and phantom

were set such that they remained centred on the optical axes of each beam.

6.1.2 Hologram Acquisition and Processing

Holograms were collected to verify that equalising the object and reference path lengths reduced the error caused by large-scale changes in atmospheric refractivity and heat expansion. To this end, a selection of the dosimeter characterisation tests from the previous chapter were repeated.

First, a reference hologram of the un-irradiated water cell and an object hologram of the 1 Gy flat dose region were collected. The atmospheric refractive index was then set to its maximum perturbed value from Table 5.2, as calculated in Section 5.1, and the irradiated region was re-imaged. Finally the atmospheric refractive index was reset to its reference value and the 'HeatExpandOptic' subroutine was executed to model the amount of heat expansion induced by a 5 °C temperature increase and the irradiated region was imaged once more.

Each of these hologram pairs was reconstructed to yield a map of the measured dose for each interferometer state. The dose-defect map of each perturbed state was then extracted from these maps using the methodology outlined in Section 5.1.2. The average defects were expressed as percentage uncertainties and compared with those measured in the previous chapter to assess the impact of reference and object path length equalisation.

6.1.3 Results

The un-optimised dosimeter was found to have object and reference beam path lengths of 401.28 mm and 1235.19 mm respectively. After optimisation, these path lengths were equalised to 610.25 mm for rays in each beam incident upon the centre of the CMOS detector chip.

Figures 6.3a and 6.3b show the defect maps for the atmospherically-perturbed and heat-expanded states. The average dose defect extracted from each of these was 4.8632×10^{-6} Gy and 7.5003×10^{-7} Gy respectively, which corresponded to 4.8×10^{-4} % and 7.5×10^{-5} % percent uncertainties in the 1 Gy dose. For comparison, on the un-optimised dosimeter, the error introduced by atmospheric change was 1.6×10^{-2} %, and the uncertainty introduced by heat expansion was 3.0×10^{-3} %.

Uncertainty	Dose Defect (Gy)	Uncertainty (%)
Atmospheric	4.8632×10^{-6}	4.8632×10^{-4}
Heat Expansion	7.5003×10^{-7}	7.5003×10^{-5}

TABLE 6.1: Dose defects and percentage uncertainties generated by each atmospheric parameter.

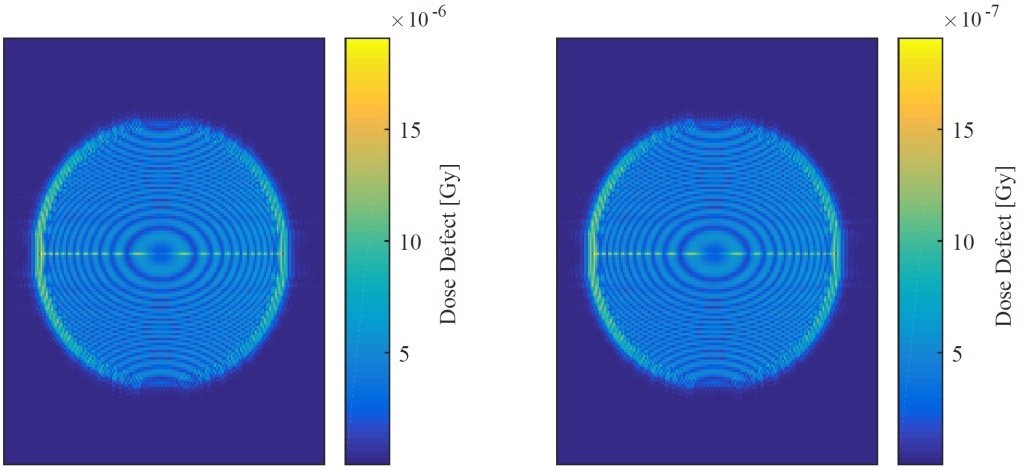

(a) Dose-defect map resulting from atmospheric perturbation on the equalised interferometer.

(b) Dose-defect map resulting from heat expansion on the equalised interferometer.

FIGURE 6.3: Dose-defect maps generated by different uncertainty sources on the interferometer with equalised object and reference beams.

These results indicate that, as hypothesized, equalising the path lengths of the reference and object beams has reduced the simulated uncertainty in dose due to large-scale atmospheric perturbations and heat expansion of the optical board. As expected, a configuration with more equal beamlines is more robust to these types of environmental instability.

6.2 Miniaturisation

Although equalising the object and reference path lengths made the dosimeter more robust against homogeneous fluctuations in optical path length, this equal-armed configuration was still very large. The long beam paths in this unsealed interferometer hold a great deal of air mass, making the dosimeter very susceptible to short-timescale atmospheric fluctuations. Vibrations

in such a large interferometer will also be more profound, as the sections of long free-space propagation magnify the effect of small centring errors.

In order to make the dosimeter less vulnerable to these types of fluctuations, miniaturisation is the most cost-effective and simplest solution available to us. It was therefore chosen to be the second case study in optimising the dosimeter.

6.2.1 Model Configuration

Achieving a miniaturised dosimeter while keeping the beam path lengths equal required a different beam expansion method to be used for the object beam. The Thorlabs beam expander included in the current model was 267 millimetres long, meaning that the object beam could not be much further reduced in length.

Two new lenses were created using FRED's graphical design environment. These lenses had focal lengths of 7.5 mm and 37.5 mm respectively. They were combined to create a much shorter 5-times magnification beam expander with a length of just over 30 mm. One of these expanders was placed between the beam splitter and the first turning mirror in the object beam, and another was placed between the turning mirror and the phantom, for a total beam expansion factor of 25 times over a combined length of just over 60 mm. With these new optics in place, the configuration was made as small as possible, with side lengths of just over 30 mm. The full schematic of this configuration is shown in Figure 6.4.

This interferometer configuration was aligned and optimised according to the protocol developed in Section 4.2.3, and field resampling planes were repositioned in the new simulation at three points in the beamlines which are indicated as resampling planes (RSP) on the diagram in Figure 6.4.

The impact of short-timescale fluctuations on this miniaturised dosimeter was then tested. First, the voxel-based atmosphere perturbation tests described in Section 5.1.3 were repeated, and hologram pairs were acquired of the slant-edge phantom, fencepost phantom, and contrast-detail phantom. The atmosphere was then returned to its default state and the simulation of mechanical vibrations was carried out as described in Section 5.3 and the same sets of holograms were obtained once more.

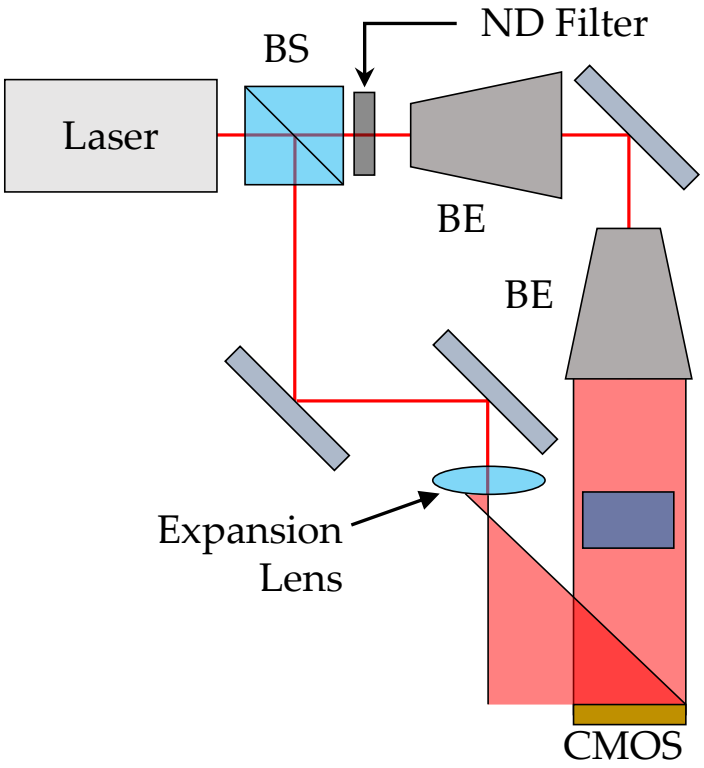

FIGURE 6.4: Schematic of the miniaturised dosimeter.

All holograms collected during these trials were obtained using the time-average methodology, where many images are acquired with randomised perturbations and added together to simulate blurring of the fringe pattern. The time-average method is fully outlined in Section 5.1.3, and the acquisition subroutine is included in Appendix B.5.

6.2.2 Results

The slant-edge phantom hologram was reconstructed against the reference image of the water block, and an MTF was obtained from the interferogram image as a point of comparison between previous system iterations. The MTF plot of the miniaturised dosimeter is shown in Figure 6.5, from which it can be seen that the miniaturised interferometer's with no simulated uncertainties has a resolution limit of 44 lp/mm. This is considerably better than the MTF obtained of the large interferometer configuration, which had a resolving limit of 34 lp/mm under the same conditions.

Uncertainty sources still had a dramatic impact upon the system MTF,

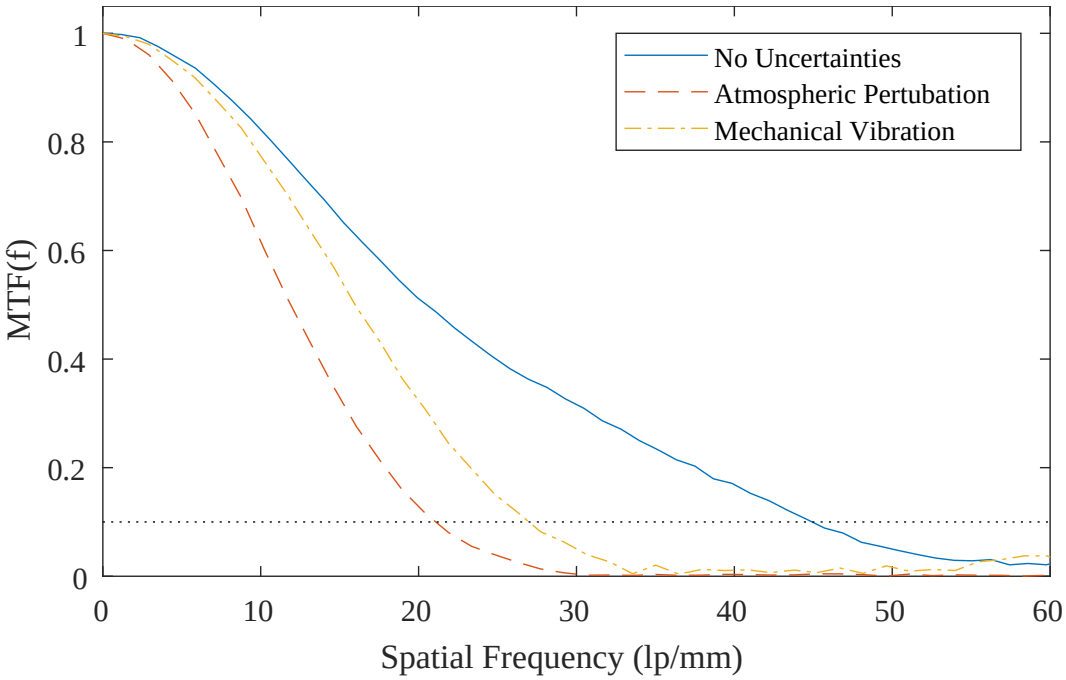

FIGURE 6.5: MTF for the unperturbed system, compared to MTFs collected from the system under the influence of mechanical vibration and atmospheric turbulence.

with the spatial resolution dropping to 28 lp/mm under the mechanical vibrations, and 22 lp/mm when the atmospheric fluctuations were applied. However these values were considerably higher than those collected under the same uncertainty conditions using the larger LFTDH configuration. Overall, these MTF results show that the performance of the interferometer was dramatically improved by miniaturisation. This is further corroborated by the results of the fencepost trials as shown in Figure 6.6. and the reconstructed image of the contrast-detail phantom shown in Figure 6.7.

The results of the fencepost tests show that the miniaturised system still has a much better spatial resolution than the large LFTDH dosimeter. The spatial resolution of the miniature LFTDH dosimeter as given by these trials is 18 lp/mm for the unperturbed system, 12 lp/mm for the system undergoing mechanical vibrations, and 11 lp/mm for the system with applied atmospheric turbulence.

Analysis of the contrast-detail phantom reconstructions also shows marked improvement. The miniaturised dosimeter with no perturbations is capable of visualising most of the 0.01 Gy dose column, and even with applied atmospheric and vibrational uncertainties, it is still able to resolve doses an order of magnitude smaller than those measured by the large

LFTDH simulation under similar conditions.

These results are promising. Although conducting a full system optimisation was outside the scope of this project, two case studies in optimisation have been attempted. It has been confirmed that FRED's scripting interface is a suitable tool for prototyping virtual refinements to our model. In addition, the results from these ventures agree with the observations of Cavan in her work on the prototype dosimeter, and with the theory of best practice in interferometry.

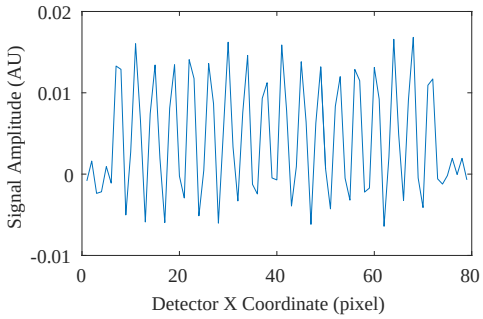

(a) 18 lp/mm region from unperturbed dosimeter.

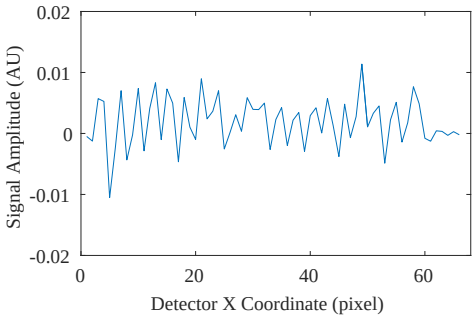

(b) 19 lp/mm region from unperturbed dosimeter.

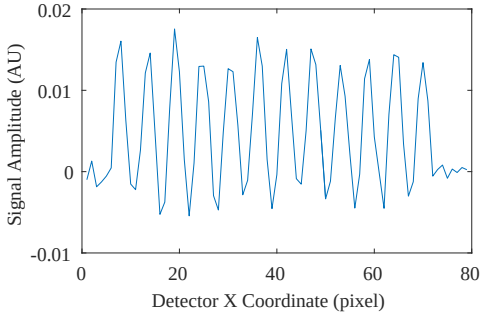

(c) 12 lp/mm region from dosimeter undergoing vibration.

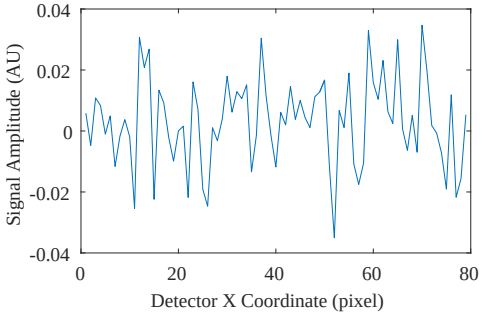

(d) 13 lp/mm region from dosimeter undergoing vibration.

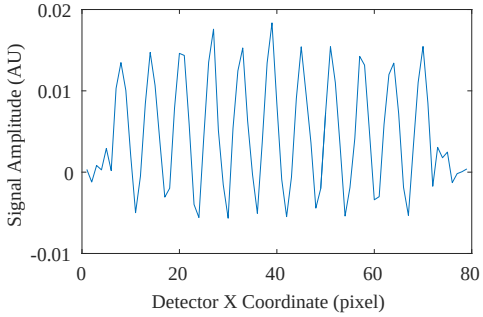

(e) 11 lp/mm region from dosimeter with turbulent atmosphere.

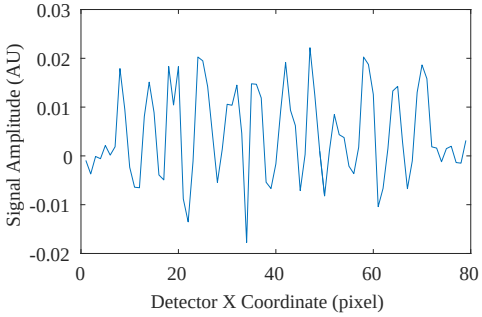

(f) 12 lp/mm region from dosimeter with turbulent atmosphere.

FIGURE 6.6: Comparison of line profiles collected with the miniaturised dosimeter under different simulated environmental conditions.

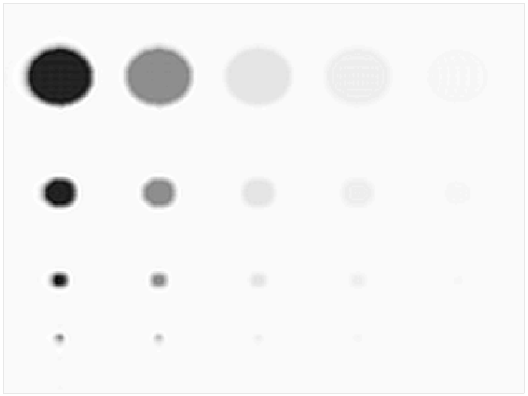

(a) CD plot collected with unperturbed miniature dosimeter.

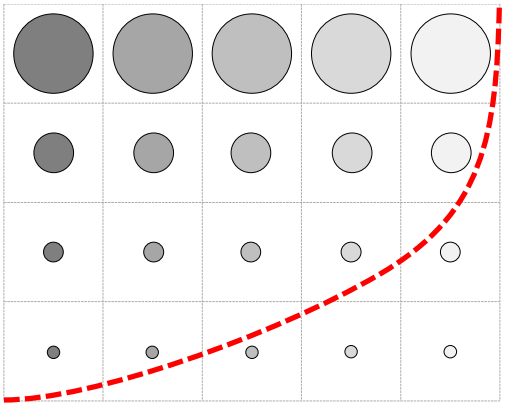

(b) CD plot collected with unperturbed miniature dosimeter.

(c) CD plot collected with miniature dosimeter under atmospheric perturbation.

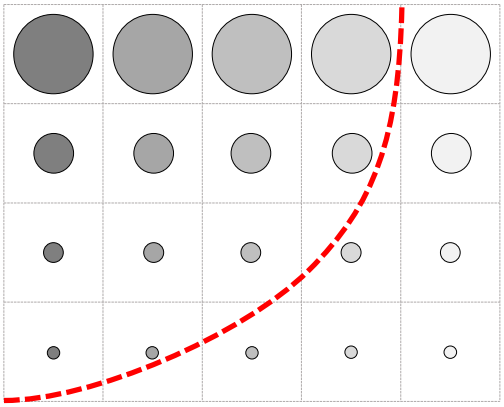

(d) CD plot collected with miniature dosimeter under atmospheric perturbation.

(e) CD plot collected with miniature dosimeter under mechanical vibration.

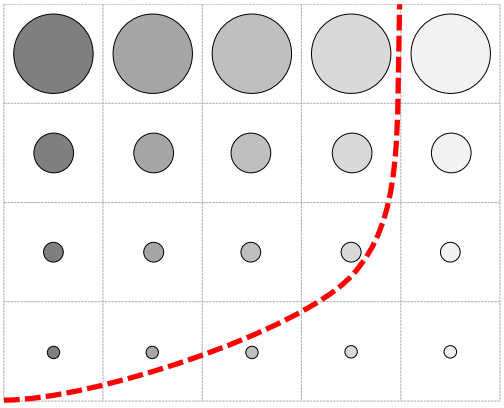

(f) CD plot collected with miniature dosimeter under mechanical vibration.

FIGURE 6.7: Contrast detail plots acquired by the miniature dosimeter under different simulated environmental conditions.

Chapter 7

Discussion

7.1 Evaluation of Project Aims

This research was conducted to ascertain whether the FRED optical modelling program could be used to virtually prototype improvements to our research group's DHI radiation dosimeter. In order to be a suitable candidate for this work, FRED must be able to adequately model the output of an LFTDH dosimeter, accurately model sources of environmental uncertainty and quantify their impact on hologram acquisition. It must also be capable of modelling changes to the prototype dosimeter, and verifying that these changes improve the dosimeter's response to environmental fluctuations and other uncertainties.

7.1.1 Suitability of FRED for Modelling DHI Dosimetry

In order to adequately represent the prototype DHI dosimeter, FRED had to be able to produce an output which matched that produced by the experimental dosimeter, and it also had to be able to resolve dose distributions on the order of clinical significance.

Tests conducted on the FRED model of the Michelson interferometer, described in Section 4.1 showed the software to be capable of accurately modelling interferometric effects at very small scales, and proved it to be capable of resolving doses as low as 8 mGy. These results showed that FRED was generally suitable for modelling interferometric sensors, and verified that it was capable of resolving variations in optical path length smaller than those expected in clinical dosimetry.

FRED was also shown to be capable of reproducing the results of our group's LFTDH dosimeter. Several LFTDH interferometer configurations were created over the course of this research, and the geometry and underlying structure of the holograms generated by each one were in accordance with theoretical expectations. The lower limits of spatial and dose resolution for these systems were not extensively probed, but favourable configurations of the LFTDH dosimeter were shown to be capable of resolving doses as low as 10 mGy. These results therefore show that FRED is capable of modelling the clinical application of an LFTDH dosimeter.

Finally, it is noteworthy that the algorithms developed by Cavan during her research were able to be used to process the output of the FRED LFTDH interferometer models. All changes to this code were simple quality-of-life and user interface changes which did not affect the underlying mathematical reconstruction being applied. The fact that this is the case further reinforces our conclusion that FRED was accurately simulating the experimental prototype, since the same reconstruction code accurately reproduced the object wave from both the experimental and simulated holograms.

7.1.2 Modelling Sources of Dosimetric Uncertainty

FRED was also shown to be capable of modelling the primary sources of uncertainty affecting the prototype dosimeter, and the impact of beam geometry and optical configuration on the amount of dosimetric uncertainty observed. Implementation of different environmental fluctuations affected the holograms in ways that were consistent with experimental observations, as in the case of mechanical vibration and atmospheric turbulence which caused blurring in the collected holograms, seen in Figure 5.6 from Section 5.1.3.

The first uncertainty modelled was the addition of beam expanding and steering optics to transition between the simple and full LFTDH interferometer models. As expected, the inclusion of additional optics caused a measurable decline in the quality of images recorded with the dosimeter. The simple model had a spatial resolution of 47 lp/mm, or 19 lp/mm when phase unwrapping effects were included, whereas for the full model these values changed to 34 lp/mm and 14 lp/mm respectively. The contrast-detail resolution was also better for the simple model, which could detect 0.01 Gy dose voxels, which were not resolvable with the full system.

The results of the uncertainty case studies were also consistent with expectations based on theoretical and experimental background. In every case, perturbing the system to mimic a source of environmental noise or fluctuation increased the dosimetric uncertainty and reduced the contrast-detail and spatial resolving power of the system.

Cavan and Meyer observed the main sources of uncertainty to be mechanical vibration and atmospheric turbulence. They also noted a contribution to dosimetric error from heat expansion and large-scale atmospheric changes [26]. These assumptions were tested in Chapter 5 and generally found to hold true.

Under mechanical vibration, the spatial resolution of the modelled dosimeter as measured by the MTF test dropped to 22 lp/mm and under atmospheric turbulence it was reduced further to 17 lp/mm. When phase unwrapping effects were measured, the spatial resolution under each of these uncertainty paradigms was 7 lp/mm and 5 lp/mm respectively. The contrast-detail resolution of the system also followed the same trend, where the unperturbed system resolved the most voxels in the contrast-detail phantom, followed by the system under mechanical perturbation and finally under atmospheric turbulence.

Heat expansion and whole-atmosphere fluctuations were also found to behave as expected. They did not introduce additional noise into the system, but created a defect in the measured dose when compared to the unperturbed system. For atmospheric fluctuations, this defect was measured to be 0.016 % whereas for heat expansion it was measured to be 0.003 %.

7.1.3 Modelling Improvements to the Prototype Dosimeter

Finally, FRED was shown to be capable of modelling refinements to the prototype and quantifying their impact on the system's robustness to environmental fluctuations and sources of uncertainty.

The utility of FRED's merit function optimisation tool was demonstrated by conducting a case study of equalising the arm length of the dosimeter, and this improvement was shown to reduce its susceptibility to long-timescale atmospheric fluctuations and heat expansion. The uncertainties induced in the path length equalised dosimeter were found to be 4.8×10^{-4} % from atmospheric changes and 7.5×10^{-5} % from heat expansion.

Finally, a miniaturisation of the dosimeter was attempted in order to mitigate the effects of short-timescale environmental fluctuations, and these were shown to be successful, increasing the MTF-measured spatial resolution of the system to 44 lp/mm, 28 lp/mm and 22 lp/mm for system under the influence of no uncertainties, mechanical vibration, and atmospheric fluctuation respectively. Similarly, when the phase unwrapper and other processing effects were taken into account, the spatial resolution for each of these tests was found to be 18 lp/mm, 12 lp/mm, and 11 lp/mm. The spatial resolution of the dosimeter was therefore shown to improve by approximately 30% due to system miniaturisation. The contrast-detail tests exhibited similar results which can be viewed in Figure 6.7.

The successful completion of these case studies indicated that FRED was a suitable candidate for virtual refinement of the prototype dosimeter. It was found to be capable of accurately modelling uncertainties in the dosimetric system and quantifying the impact of systemic changes on the total dosimetric uncertainties.

7.1.4 Advantages and Drawbacks of FRED

The graphical element creation interface in FRED was extremely useful in creating a wide variety of phantoms and masks, such that different tests could be easily carried out to assess and compare image quality of our interferometric systems. The flexibility of these creation tools allows for detailed plane, polygon and curve creation, and the software also supports import of Zemax files storing optical elements and catalogues. As Zemax LLC (based in Kirkland, Washington) is the industry standard for optical simulation, used by most optics vendors, this is an important capability. Finally, FRED is also capable of importing geometric data, such as AutoCAD files (a filetype used in programs from Autodesk Inc, based in San Rafael, California), in order to create more complex solid structures to simulate lens housings, optomechanical components, and detector casings. However, it is worth noting that the import of certain proprietary filetypes is not supported, and certain manufacturer lens catalogues were thus unavailable in FRED outside creation by hand.

FRED's scripting interface was also a powerful tool, allowing its different

analysis functions to be integrated. This allowed for the creation of complex merit functions and other system metrics in order to quantify the performance of our dosimeter.

One drawback is that FRED is a licensed software platform, offering gratis licenses only to graduate students working on optical design projects. Therefore, its utility to a group operating on a limited budget is potentially reduced.

Overall, FRED seems to be entirely capable of modelling the optical phenomena required to simulate interferometric radiation dosimetry. It operates on complex-ray tracing algorithms which are easily robust enough to model our prototype interferometer. FRED is also priced competitively compared to the market-leading optical design programs such as Zemax, although there may be cheaper or open-source alternatives which have not been explored.

7.2 Recommendations for Future Work

7.2.1 Voxel-based Test Cell

One of the foremost changes that could be made to increase the utility of FRED analyses is the implementation of a voxel-based test cell. The complexity of patterns which were visualised in this research was severely limited by the fact that they had to be initialised as a collection of element primitives in FRED.

Inclusion of a voxel-based cell would also allow us to import Monte Carlo generated dose distributions across the volume of our test cell, subject these to heat diffusion calculations similar to those carried out by Cavan in her doctoral research, and then import the final results of these analyses into FRED for imaging. This would allow a much more detailed and accurate reconstructions of physical dose distributions, rather than the highly idealised cylindrical and square cross-sections created in this research.

7.2.2 Unified Uncertainty Model

Time constraints in this research limited our focus to the investigation of FRED and assessment of its suitability as a modelling tool. Therefore the

uncertainty analyses conducted were carried out as case studies in FRED's capabilities, rather than as earnest attempts to fully quantify the sources of dosimetric uncertainty.

Unifying the sources of uncertainty investigated in this thesis into a more cohesive model, ideally under the banner of a single FRED function, would make it much easier to investigate the dosimetric uncertainties being wrought by environmental fluctuations. This would also allow them to be more definitively quantified, rather than each being calculated separately.

7.2.3 Experimental Work

Additional experimental work needs to be undertaken in concert with further simulations. As the aim of this project was to assess FRED as a modelling tool, very little experimental work was undertaken, and none was conducted to assess the validity of our later investigations.

Potential avenues of further experimental work include attempting the geometric refinements proposed in Chapter 6 and measuring different refractive index gradients in order to assess the degree of improvement in dosimetric uncertainty. The FRED model should be improved in concert with experimental testing in order to ensure that its output remains consistent with the actual results of the physical dosimeter.

Chapter 8

Conclusion

8.1 Conclusion

Optical modelling programs have been used in the past to to model complex phenomena involving coherent light, from diffraction effects [28], to laser interference [27], to holography [29]. However, no precedent exists for using an optical modelling package of this nature to model interferometry for the purposes of radiation dosimetry. The goal of this research was to assess whether such software in general, and FRED specifically was suitable for this modelling task, and whether it could be used to model and refine our research group's experimental interferometric dosimeter.

After extensive analysis of FRED's coherent light handling capabilities, and the completion of several case studies in modelling and optimising our prototype dosimeter, FRED was found to be suitable for the proposed tasks.

Dosimeters reproduced in FRED, from a simple Michelson interferometer to a full model of our LFTDH dosimeter, were capable of resolving doses on the order of relevance for clinical dosimetry, and dose distributions modelled in FRED were able to be reconstructed using the same algorithms utilised by the experimental radiation dosimeter.

Perturbation of the full model of our prototype dosimeter also yielded results according to the expected trends. Vibrational and short-timescale atmospheric perturbations yielded large increases in hologram noise and therefore much lower spatial and dose resolution. Comparing the results of the full LFTDH model under uncertainty perturbation with those acquired from the unperturbed system yielded approximately a 50% decrease in spatial resolution compared to the unperturbed system, with a corresponding decrease in dose resolution.

Finally, FRED was shown to be capable of virtually prototyping refinements to the dosimeter system through two case studies in geometrical optimisation. The reference and object path lengths in the dosimeter were equalised, and this alteration was successfully shown to reduce the susceptibility of the dosimeter to large-scale environmental changes. The dosimeter was then miniaturised, which was shown to make the dosimeter more robust against short-timescale environmental noise.

These case studies in modelling the prototype, investigating its uncertainties, and virtually refining the dosimeter suffice to show that FRED is capable of being used to test improvements to our radiation dosimeter. With the development of more holistic uncertainty models and more quantitative measures of system performance, optical modelling has the potential to be an enormously powerful tool in refining dosimetric systems of this nature.

Bibliography

[1] Gerard J Tortora and Bryan H Derrickson. *Principles of anatomy and physiology*. John Wiley & Sons, 2008.

[2] Carol Bernstein et al. "DNA damage, DNA repair and cancer". In: *New Research Directions in DNA Repair*. InTech, 2013.

[3] Errol C Friedberg et al. *DNA repair and mutagenesis*. American Society for Microbiology Press, 2005.

[4] Cristian Tomasetti, Lu Li, and Bert Vogelstein. "Stem cell divisions, somatic mutations, cancer etiology, and cancer prevention". In: *Science* 355.6331 (2017), pp. 1330–1334.

[5] Ahmedin Jemal et al. "Global cancer statistics". In: *CA: a cancer journal for clinicians* 61.2 (2011), pp. 69–90.

[6] Statistics New Zealand. *New Zealand cohort life tables: March 2018 update*. Annual report. Mar. 5, 2018.

[7] Ministry of Health Analytical Services. *New cancer Registrations 2015*. Annual report. Dec. 14, 2017.

[8] Ministry of Health Analytical Services. *Cancer: Historical summary 1948–2013*. Annual report. Sept. 9, 2016.

[9] Ministry of Health Analytical Services. *Cancer: New registrations and deaths 2013*. Annual report. Sept. 9, 2016.

[10] Ministry of Health. *New Zealand Cancer Plan: Better, faster cancer care 2015–2018*. Annual report. May 13, 2014.

[11] Ministry of Health. *Cancer patient survival 1994–2011*. Annual report. Apr. 14, 2016.

[12] Kimberly D Miller et al. "Cancer treatment and survivorship statistics, 2016". In: *CA: a cancer journal for clinicians* 66.4 (2016), pp. 271–289.

[13] Drew M Pardoll. "The blockade of immune checkpoints in cancer immunotherapy". In: *Nature Reviews Cancer* 12.4 (2012), p. 252.

[14] E B Podgorsak and International Atomic Energy Agency. *Radiation oncology physics: a handbook for teachers and students*. Vienna: International Atomic Energy Agency, 2005.

[15] Michael C Joiner and Albert Van der Kogel. *Basic clinical radiobiology*. Vol. 1. CRC press, 2016.

[16] Eric J Hall, Amato J Giaccia, et al. *Radiobiology for the Radiologist*. Vol. 6. Lippincott Williams & Wilkins Philadelphia, 2006.

[17] Leo E Gerweck et al. "Tumor cell radiosensitivity is a major determinant of tumor response to radiation". In: *Cancer research* 66.17 (2006), pp. 8352–8355.

[18] Harrison H Barrett et al. "Objective assessment of image quality VI: Imaging in radiation therapy". In: *Physics in Medicine & Biology* 58.22 (2013), p. 8197.

[19] INTERNATIONAL ATOMIC ENERGY AGENCY. *Radiation Dose in Radiotherapy from Prescription to Delivery*. IAEA-TECDOC-896. Vienna: INTERNATIONAL ATOMIC ENERGY AGENCY, 1996. URL: http://www-pub.iaea.org/books/IAEABooks/5545/Radiation-Dose-in-Radiotherapy-from-Prescription-to-Delivery.

[20] ICRU. "Prescribing, recording and reporting photon beam therapy". In: *Report* 50 (1993).

[21] ICRU. "Recording and reporting photon beam therapy (supplement to ICRU Report 50)". In: *Report* 62 (1999).

[22] Indra J Das, George X Ding, and Anders Ahnesjö. "Small fields: nonequilibrium radiation dosimetry". In: *Medical physics* 35.1 (2008), pp. 206–215.

[23] Oliver Jäkel. "Heavy ion radiotherapy". In: *New Technologies in Radiation Oncology*. Springer, 2006, pp. 365–377.

[24] Vincent Favaudon et al. "Ultrahigh dose-rate FLASH irradiation increases the differential response between normal and tumor tissue in mice". In: *Science translational medicine* 6.245 (2014), 245ra93–245ra93.

[25] Alicia Cavan and Juergen Meyer. "Digital holographic interferometry: A novel optical calorimetry technique for radiation dosimetry". In: *Medical physics* 41.2 (2014).

[26] Alicia Emily Cavan. "Digital Holographic Interferometry for Radiation Dosimetry". In: (2015).

[27] Simonas Indrišiūnas et al. "Two complementary ways of thin-metal-film patterning using laser beam interference and direct ablation". In: *Journal of Micromechanics and Microengineering* 23.9 (2013), p. 095034.

[28] Quan Liu, Jianhong Wu, and Chaoming Li. "Design of beam sampling grating and study on its diffraction action". In: *ICO20: Optical Information Processing*. Vol. 6027. International Society for Optics and Photonics. 2006, p. 60273C.

[29] Patrick Wissmann, Se Baek Oh, and George Barbastathis. "Simulation and optimization of volume holographic imaging systems in Zemax®". In: *Optics express* 16.10 (2008), pp. 7516–7524.

[30] AJ Fresnel. "Diffraction of light". In: *A. Mem. de l'Acad. Sci* 5 (1826), p. 339.

[31] Thomas Young. "II. The Bakerian Lecture. On the theory of light and colours". In: *Philosophical transactions of the Royal Society of London* 92 (1802), pp. 12–48.

[32] James Clerk Maxwell. *A treatise on electricity and magnetism*. Vol. 1. Clarendon press, 1881.

[33] Max Planck. "On the law of distribution of energy in the normal spectrum". In: *Annalen der physik* 4.553 (1901), p. 1.

[34] Raymond A Serway, Clement J Moses, and Curt A Moyer. *Modern physics*. Cengage Learning, 2004.

[35] Paul Adrien Maurice Dirac. "On the theory of quantum mechanics". In: *Proc. R. Soc. Lond. A* 112.762 (1926), pp. 661–677.

[36] E. Schrödinger. "Quantisierung als Eigenwertproblem". In: *Annalen der Physik* 384.4 (1926), pp. 361–376.

[37] Hans A Bethe. "The electromagnetic shift of energy levels". In: *Physical Review* 72.4 (1947), p. 339.

[38] Richard Phillips Feynman. "Space-time approach to quantum electrodynamics". In: *Physical Review* 76.6 (1949), p. 769.

[39] Dave3457. *Circularly Polarised Light and Linearly Polarised Light Comparison*. Image license: public domain. 2010. URL: https://commons.wikimedia.org/wiki/File:Circular.Polarization.Circularly.Polarized.Light_With.Components_Right.Handed.svg.

[40] Oleg Alexandrov. *Illustration of Snell's Law*. Image license: public domain. 2007. URL: https://commons.wikimedia.org/wiki/File:Snells_law2.svg.

[41] Thomas Kreis. "Holographic interferometry: principles and methods". In: *Simulation and Experiment in Laser Metrology: Proceedings of the International Symposium on Laser Applications in Precision Measurements Held in Balatonfüred/Hungary*. Vol. 2. 1996, p. 323.

[42] Albert A Michelson and Edward W Morley. "On the Relative Motion of the Earth and of the Luminiferous Ether". In: *Sidereal Messenger, vol. 6, pp. 306-310* 6 (1887), pp. 306–310.

[43] AA Michelson, FG Pease, and F Pearson. "Repetition of the Michelson-Morley experiment". In: *JOSA* 18.3 (1929), 181_1–182.

[44] Albert A Michelson and Francis G Pease. "Measurement of the diameter of Alpha-Orionis by the interferometer". In: *Proceedings of the National Academy of Sciences* 7.5 (1921), pp. 143–146.

[45] John D Monnier. "Optical interferometry in astronomy". In: *Reports on Progress in Physics* 66.5 (2003), p. 789.

[46] MV Mantravadi and D Malacara. "Newton, Fizeau, and Haidinger interferometers". In: *Optical shop testing* 59 (1992), pp. 1–45.

[47] HR Carleton and WT Maloney. "A balanced optical heterodyne detector". In: *Applied optics* 7.6 (1968), pp. 1241–1243.

[48] Bing Pan et al. "Two-dimensional digital image correlation for in-plane displacement and strain measurement: a review". In: *Measurement science and technology* 20.6 (2009), p. 062001.

[49] Dipankar Bhattacharyya et al. "Direct measurement on transparent plates by using Fizeau interferometry". In: *Optics & Laser Technology* 34.1 (2002), pp. 93–96.

[50] R South and BM Hayward. "Temperature measurement in conical flames by laser interferometry". In: *Combustion Science and Technology* 12.4-6 (1976), pp. 183–195.

[51] Astrid Aksnes Dyrseth and Rudie Spooren. "Measuring mixing dynamics of transparent fluids with electronic speckle pattern interferometry". In: *Applied optics* 36.25 (1997), pp. 6171–6177.

[52] Masanobu Maeda, Tatsuya Kawaguchi, and Koichi Hishida. "Novel interferometric measurement of size and velocity distributions of spherical particles in fluid flows". In: *Measurement Science and Technology* 11.12 (2000), p. L13.

[53] Dennis Gabor. *A new microscopic principle*. 1948.

[54] Dennis Gabor et al. "Microscopy by reconstructed wave-fronts". In: *Proc. R. Soc. Lond. A* 197.1051 (1949), pp. 454–487.

[55] Dennis Gabor. "Microscopy by reconstructed wave fronts: II". In: *Proceedings of the Physical Society. Section B* 64.6 (1951), p. 449.

[56] Theodore H Maiman et al. "Stimulated optical radiation in ruby". In: (1960).

[57] Yuri N Denisyuk. "On the reflection of optical properties of an object in a wave field of light scattered by it". In: *Doklady Akademii Nauk SSSR* 144.6 (1962), pp. 1275–1278.

[58] A Graube. "Advances in bleaching methods for photographically recorded holograms". In: *Applied optics* 13.12 (1974), pp. 2942–2946.

[59] David W Robinson. "Automatic fringe analysis with a computer image-processing system". In: *Applied Optics* 22.14 (1983), pp. 2169–2176.

[60] Robert L Powell and Karl A Stetson. "Interferometric vibration analysis by wavefront reconstruction". In: *JOSA* 55.12 (1965), pp. 1593–1598.

[61] EK Hussmann. "A holographic interferometer for measuring radiation energy deposition profiles in transparent liquids". In: *Applied optics* 10.1 (1971), pp. 182–186.

[62] Arne Miller, EK Hussmann, and WL McLaughlin. "Interferometer for measuring fast changes of refractive index and temperature in transparent liquids". In: *Review of Scientific instruments* 46.12 (1975), pp. 1635–1638.

[63] Arne Miller and William L McLaughlin. "Imaging and measuring electron beam dose distributions using holographic interferometry". In: *Nuclear Instruments and Methods* 128.2 (1975), pp. 337–346.

[64] Arne Miller. "Holography and interferometry in dosimetry". In: *Nukleonika* 24.9 (1979), pp. 907–925.

[65] Eugene V Malyarenko et al. "High-resolution ultrasonic thermometer for radiation dosimetry". In: *The Journal of the Acoustical Society of America* 124.6 (2008), pp. 3481–3490.

[66] T Ackerly et al. "High resolution optical calorimetry for synchrotron microbeam radiation therapy". In: *Journal of Instrumentation* 6.03 (2011), P03003.

[67] Everardo Flores-Martinez, Martha J Malin, and Larry A DeWerd. "Development and characterization of an interferometer for calorimeter-based absorbed dose to water measurements in a medical linear accelerator". In: *Review of Scientific Instruments* 87.11 (2016), p. 114301.

[68] AM Beigzadeh, MR Rashidian Vaziri, and F Ziaie. "Modelling of a holographic interferometry based calorimeter for radiation dosimetry". In: *Nuclear Instruments and Methods in Physics Research Section A: Accelerators, Spectrometers, Detectors and Associated Equipment* 864 (2017), pp. 40–49.

[69] Herbert John Pain. *THE PHYSICS OF VIBRATIONS AND WAVES Sixth Edition*. John Wiley & Sons Ltd, 2017.

[70] Anthony Gerrard and James M Burch. *Introduction to matrix methods in optics*. Courier Corporation, 1994.

[71] A.E. Siegman. *Lasers*. University Science Books, 1986. ISBN: 9780935702118. URL: https://books.google.com.au/books?id=1BZVwUZLTkAC.

[72] Willem Brouwer. "Matrix methods in optical instrument design". In: *Matrix Methods in Optical Instrument Design, by Willem Brouwer New York, NY: WA Benjamin, INC., 1964* (1964).

[73] Rüdiger Paschotta. *Field guide to lasers*. Vol. 12. SPIE press, 2008.

[74] Jacques Arnaud. "Representation of Gaussian beams by complex rays". In: *Applied optics* 24.4 (1985), pp. 538–543.

[75] MA Alonso and GW Forbes. "Using rays better. II. Ray families to match prescribed wave fields". In: *JOSA A* 18.5 (2001), pp. 1146–1159.

[76] GW Forbes. "Using rays better. IV. Theory for refraction and reflection". In: *JOSA A* 18.10 (2001), pp. 2557–2564.

[77] Alexey N Bashkatov and Elina A Genina. "Water refractive index in dependence on temperature and wavelength: a simple approximation". In: *Saratov Fall Meeting 2002: Optical Technologies in Biophysics and Medicine IV*. Vol. 5068. International Society for Optics and Photonics. 2003, pp. 393–396.

[78] Photon Engineering. *Scripting Basics in FRED*. Software Manual. Accessed: 2017-05-21.

[79] Jerrold T Bushberg and John M Boone. *The essential physics of medical imaging*. Lippincott Williams & Wilkins, 2011.

[80] Carles Mitja et al. *Slanted Edge MTF*. https://imagej.nih.gov/ij/plugins/se-mtf/index.html. Accessed: 2018-05-21. 2011.

[81] Miguel Arevallilo Herráez et al. "Fast two-dimensional phase-unwrapping algorithm based on sorting by reliability following a noncontinuous path". In: *Applied optics* 41.35 (2002), pp. 7437–7444.

[82] KP Birch and MJ Downs. "The results of a comparison between calculated and measured values of the refractive index of air". In: *Journal of Physics E: Scientific Instruments* 21.7 (1988), p. 694.

[83] Bengt Edlén. "The refractive index of air". In: *Metrologia* 2.2 (1966), p. 71.

[84] Philip E Ciddor. "Refractive index of air: new equations for the visible and near infrared". In: *Applied optics* 35.9 (1996), pp. 1566–1573.

[85] Jack A. Stone and Jay H. Zimmerman. *Engineering Metrology Toolbox*. https://emtoolbox.nist.gov/Wavelength/Ciddor.asp. Accessed: 2017-09-30.

[86] KP Birch and MJ Downs. "An updated Edlén equation for the refractive index of air". In: *Metrologia* 30.3 (1993), p. 155.

[87] KP Birch and MJ Downs. "Correction to the updated Edlén equation for the refractive index of air". In: *Metrologia* 31.4 (1994), p. 315.

[88] William M Haynes. *CRC handbook of chemistry and physics*. CRC press, 2014.

[89] W Booth. *VIBRATION CONTROL: How to determine your equipment needs*. https://www.laserfocusworld.com/articles/2010/06/vibration-control.html. Accessed: 2017-12-21.

Appendix A

MATLAB Code

A.1 Dose to OPL Calculations

```
function refInd = Temp2RefInd(temp, wavelength)
%TEMP2REFIND Summary of this function goes here
%   Detailed explanation goes here

% Given variables
T = temp; WL = wavelength;
% Tabulate the constants given in Bashkatov and Genina
A0 = 1.3208;    A1 = -1.2325E-5;    A2 = -1.8674E-6;
    A3 = 5.0233E-9;
B0 = 5208.2413; B1 = -0.5179;       B2 = -2.284E-2;
    B3 = 6.9608E-5;
C0 = -2.5551E8; C1 = -18341.336;    C2 = -917.2319;
    C3 = 2.7729;
D0 = 9.3495;    D1 = 1.7855E-3;     D2 = 3.6733E-5;
    D3 = -1.2936E-7;

% Express Cauchy approximation as third order polynomial
    .
E0 = A0 + B0/WL^2 + C0/WL^4 + D0/WL^6;
E1 = A1 + B1/WL^2 + C1/WL^4 + D1/WL^6;
E2 = A2 + B2/WL^2 + C2/WL^4 + D2/WL^6;
E3 = A3 + B3/WL^2 + C3/WL^4 + D3/WL^6;

refInd = E0 + E1 * T + E2*T^2 + E3 * T^3;
end
```

A.2 Edlén Calculations

```
function nTPf = nAtmosCalc(T, p, relH, wavL)
%NATMOSCALC Calculates refractive index of air given
    atmospheric params.
%   Inputs: T       - air temperature (C)
%           P       - air pressure (kPa)
%           relH    - relative humidity (%)
%           wavL    - light wavelength (um)

% Define the values of Edlen equation constants.
        A = 8342.54;
        B = 2406147;
        C = 15998;
        D = 96095.43;
        E = 0.601;
        F = 0.00972;
        G = 0.003661;

    % Convert air pressure to Pa
    P = p * 1000;

    % Calculate the squared wavenumber from laser vacuum
        wavelength.
    S = wavL^(-2);

    % Calculate standard ref ind of the air for the
       given wavelength.
    nS = 1 + 10^(-8) * (A + B/(130-S) + C/(38.9-S));

    % Calculate the temperature and pressure corrected
       refractive index.
    X = (1 + 10^(-8)*(E - F*T)*P)/(1 + G*T);
        nTP = 1 + P*(nS - 1)*X/D;

    % Calculate the vapour pressure of the air.
    pWV = RHtoVP(T, relH);

```

```
%    Calculate the humidity corrected refractive index.
        nTPf = nTP - 10^(-10)*((292.75)/(T + 273.15))
            *(3.7345-0.401*S)*pWV;
end
```

A.3 Reconstruction Code

```
%% Document Cleanup
clear all
close all

%% User input variables.
expName = 'FPSheet'; % Experiment name for stored
    holograms.

lambda = 632.8e-9;  % Wavelength [m] of laser in
    simulation
pixsize = 6.7e-6;   % Pixel size [m] of detector. (6.7e
    -6 for CMOS)
dist = 0.375;       % Object to camera distance [m].
pathL = 0.01;       % Path length of phantom [m].
tInit = 20;         % Initial cell temperature [C].

refName = strcat(expName, 'Ref.dat');
objName = strcat(expName, 'Obj.dat');

ref = importImg(refName);
obj = importImg(objName);

resolution = size(ref); % Set the resolution based on
    image size.

%% Display raw reference/object holograms.
figure()
imagesc(ref)
    set(gca, 'xTick', [], 'yTick', [])
    set(gca,'LooseInset', get(gca,'TightInset'))

```

```
28
29 figure
30 imagesc(obj)
31     set(gca, 'xTick', [], 'yTick', [])
32     set(gca,'LooseInset', get(gca,'TightInset'))
33
34
35 %% Add noise to the holograms and display the
      reconstructed interferogram.
36 %
37 vRef = var(ref(:));
38 vObj = var(obj(:));
39
40 refNoise = imnoise(ref, 'gaussian', 0, vRef/10);
41 objNoise = imnoise(obj, 'gaussian', 0, vObj/10);
42
43 % Calculate the interferogram using the noise-added
      holograms.
44  O3 = SimplifiedFresnelReconstruction(refNoise+objNoise
       ,...
45                                       lambda,pixsize,
                                            resolution,dist
                                            );
46
47 figure
48 imagesc(log(abs(O3)))
49     set(gca, 'xTick', [], 'yTick', [])
50     set(gca,'LooseInset', get(gca,'TightInset'))
51     colormap gray
52
53 % Display the interferogram
54 fr=figure;
55     imagesc(log(abs(O3)));
56         title('Reconstructed Interferogram. Drag to
               select ROI')
57         axis  equal tight
58         colormap gray
59
```

```
60 % Get crop ROI by manually selecting an area on the
       interferogram.
61 rect = getrect(fr);
62 cropROI = round(rect);
63
64 %% Initialise empty containers for reconstruction stages
       .
65 O1 = double(zeros([cropROI(4) cropROI(3)]));%Reference
66 O2 = double(zeros([cropROI(4) cropROI(3)]));%Object
67 O3 = double(zeros([cropROI(4) cropROI(3)]));%Combined
68
69 theta1 = double(zeros([cropROI(4) cropROI(3)])); % Ref
       angle
70 theta2 = double(zeros([cropROI(4) cropROI(3)])); % Obj
       angle
71 theta3 = double(zeros([cropROI(4) cropROI(3)])); % Int
       angle
72
73 UnwrappedPhase2D_Herraez = double(zeros([cropROI(4)
       cropROI(3)]));
74
75 %% Reconstruct the noiseless holograms
76 % Reference reconstruction
77 O1 = SimplifiedFresnelReconstruction(...
78       ref,...
79       lambda,...
80       pixsize,...
81       resolution,...
82       dist,...
83       cropROI);
84
85 % Object reconstruction.
86 O2 = SimplifiedFresnelReconstruction(...
87       obj,...
88       lambda,...
89       pixsize,...
90       resolution,...
91       dist,...
```

```
92      cropROI);
93
94  % Combined reconstruction.
95  O3 = SimplifiedFresnelReconstruction(...
96      (ref + obj),...
97      lambda,...
98      pixsize,...
99      resolution,...
100     dist,...
101     cropROI);
102
103
104
105 %% Extract and unwrap the interference phase between
        these two holograms.
106 theta1(:,:)=angle(O1(:,:));
107 theta2(:,:)=angle(O2(:,:));
108 dtheta(:,:)= InterferencePhase(theta1(:,:),theta2(:,:));
109 UnwrappedPhase2D_Herraez(:,:) = Herraez_2D_unwrapper_M(
        single(dtheta(:,:)));
110
111 angO3 = angle(O3(:,:));
112
113 figure
114 imagesc(dtheta)
115
116 figure
117 imagesc(angO3)
118 %%% Display the unwrapped phase (linear and log)
119 figure
120 imagesc(UnwrappedPhase2D_Herraez)
121     set(gca, 'xTick', [], 'yTick', [])
122     set(gca,'LooseInset', get(gca,'TightInset'))
123     colormap(gray)
124     truesize([420,560])
125
126
127 figure
```

```
128 imagesc(log(abs(UnwrappedPhase2D_Herraez)))
129     set(gca, 'xTick', [], 'yTick', [])
130     set(gca,'LooseInset', get(gca,'TightInset'))
131     colormap(gray)
132     truesize([420,560])
133 %
134 %%% Plot the transects across each row of the phantom.
135 % transect1 = UnwrappedPhase2D_Herraez(30, :);
136 % transect2 = UnwrappedPhase2D_Herraez(80, :);
137 % transect3 = UnwrappedPhase2D_Herraez(130, :);
138 % transect4 = UnwrappedPhase2D_Herraez(190, :);
139 %
140 % figure
141 % plot(transect1)
142 %
143 % figure
144 % plot(transect2)
145 %
146 % figure
147 % plot(transect3)
148 %
149 % figure
150 % plot(transect4)
151 %
152 %
153 %%% Unwrapped phase to dose
154 % OPD = -UnwrappedPhase2D_Herraez*(lambda/(2*pi));
155 % nChange = OPD/pathL;
156 %
157 %% Work out the original refractive index of the water.
158 % nInitial = Temp2RefInd(tInit, lambda*10^9); % lambda
      must be in nanometers
159 %
160 %% Calculate the actual refractive index of the water
      from the change.
161 % nAbsolute = nChange + nInitial;
162 %
```

```
163 %% Calculate the temperature of the cell based on
        absolute refractive index.
164 % temperature = GetTempMap(nAbsolute, lambda*10^9);
165 % tempChange = temperature - tInit;
166 % doseChange = 4181.8*tempChange;
167
168 % figure()
169 % imagesc(OPD)
170 % title('OPD map')
171 %
172 % figure()
173 % imagesc(nChange)
174 % title('refInd change')
175 %
176 % figure()
177 % imagesc(nAbsolute)
178 % title('Absolute refractive index of irradiated cell')
179 %
180 % figure()
181 % imagesc(temperature)
182 % title('Temperature map of irradiated cell')
183 %
184 % figure()
185 % imagesc(doseChange)
186 % title('profile of dose administered to irradiated cell
        ')
187 %
188 %
189 % figure
190 % xx = 1:cropROI(3);
191 % plot(xx,nChange(round(cropROI(4)/2),:))
192 % title('Refractive Index Change')
193 % xlabel('Pixel (x direction)')
194 % ylabel('Refractive Index')
195 %
196 %
197 % figure
198 % xx = 1:cropROI(3);
```

```
199 % plot(xx,tempChange(round(cropROI(4)/2),:))
200 % title('Temperature Change')
201 % xlabel('Pixel (x direction)')
202 % ylabel('Temperature (c)')
203 %
204 %
205 %
206 % figure
207 % xx = 1:cropROI(3);
208 % plot(xx,doseChange(round(cropROI(4)/2),:))
209 % title('Dose')
210 % xlabel('Pixel (x direction)')
211 % ylabel('Dose (Gy)')
```

Appendix B

FRED Code

B.1 Hologram Export Code

```
'#Language "WWB-COM"

Option Explicit

Sub Main

'Document Cleanup
DeleteRays()
ARNDeleteAllNodes()
ClearOutputWindow()

Dim expName As String          'Name of the experiment
    (written into fNames)
Dim saveDir As String          'Name of the directory
    for the data files.
Dim analysisNa As String       'Name of the analysis
    surface being used.
Dim phantomKW As String        'Keyword label on
    phantom to be used as object.

'Set filename and save directory for the exported data
    file.
saveDir = "C:\Documents\MSc Thesis\ThesisData\Exp 03 -
    LFTDH\"
expName = "FP1"
```

```
20
21
22  ' Set the analysis name and phantom name.
23  analysisNa = "Analysis Surface(s).CMOSChip"
24  phantomKW = "FPSheet"
25
26
27  ' Trace rays and save the resulting reference and object
        holograms.
28  ExportRefIrr( saveDir, expName, analysisNa )
29  Print "Reference hologram successfully acquired."
30  ExportObjIrr( saveDir, expName, analysisNa, phantomKW )
31  Print "Object hologram successfully acquired."
32
33
34
35  End Sub
36
37  Function ExportRefIrr( saveDir As String, fName As
       String, anaSurfName As String )
38
39          'Dimension save parameters.
40          Dim saveName As String
41
42          saveName = saveDir & fName & "Ref.dat"
43
44          ' Dimension analysis surface parameters.
45          Dim anaNode As Long
46          Dim ana As T_ANALYSIS
47          Dim noPixX As Long
48          Dim noPixY As Long
49
50          anaNode = FindFullName( anaSurfName )
51          LoadAnalysis(anaNode, ana )
52          noPixX = 1 + ana.Amax - ana.Amin
53          noPixY = 1 + ana.Bmax - ana.Bmin
54
```

```
55          ' Set the beam dumps and all phantom objects to
               be untracable.
56          SetTraceableByKeyWord( "BeamDumps", False )
57          SetTraceableByKeyWord( "Phantoms", False )
58
59          'Ensure the attenuator is traceable
60          SetTraceableByKeyWord( "Attenuator", True )
61
62          ' Dimension ARN node and array to store
               irradiance map.
63          Dim arnNode As Long
64          Dim irrad() As Double
65
66          ' Trace rays and extract irradiance data.
67          EnableTextPrinting(False)
68          TraceCreate
69          IrradianceToARN( anaNode, "IrradMap", arnNode )
70          ARNGetDataAsDoubleArray ( arnNode, irrad() )
71          EnableTextPrinting(True)
72
73          WriteArrayToFile( saveName, irrad, noPixX,
               noPixY )
74
75          Update
76
77  End Function
78
79  Function ExportObjIrr( saveDir As String, fName As
       String, anaSurfName As String, phantomKW As String )
80
81          'Dimension save parameters.
82          Dim saveName As String
83
84          saveName = saveDir & fName & "Obj.dat"
85
86          ' Dimension analysis surface parameters.
87          Dim anaNode As Long
88          Dim ana As T_ANALYSIS
```

```
89          Dim noPixX As Long
90          Dim noPixY As Long
91
92          anaNode = FindFullName( anaSurfName )
93          LoadAnalysis(anaNode, ana )
94          noPixX = 1 + ana.Amax - ana.Amin
95          noPixY = 1 + ana.Bmax - ana.Bmin
96
97          ' Set the beam dumps and all phantom objects to
               be untracable.
98          SetTraceableByKeyWord( "BeamDumps", False )
99          SetTraceableByKeyWord( "Phantoms", False )
100
101         'Ensure the attenuator is traceable
102         SetTraceableByKeyWord( "Attenuator", True )
103
104         ' Set the phantom to traceable.
105         SetTraceableByKeyWord( phantomKW, True )
106
107         ' Dimension ARN node and array to store
               irradiance map.
108         Dim arnNode As Long
109         Dim irrad() As Double
110
111         ' Trace rays and extract irradiance data.
112         EnableTextPrinting(False)
113         TraceCreate
114         IrradianceToARN( anaNode, "IrradMap", arnNode )
115         ARNGetDataAsDoubleArray ( arnNode, irrad() )
116         EnableTextPrinting(True)
117
118         WriteArrayToFile( saveName, irrad, noPixX,
               noPixY )
119
120         Update
121
122 End Function
123
```

```
124 Function WriteArrayToFile( fullFileNa As String, dataArr
    () As Double, arraySizeX As Long, arraySizeY As Long
    )
125
126         Dim m As Long, n As Long
127         Dim row As String
128         Dim xInds As Long, yInds As Long
129
130         yInds = arraySizeY-1
131         xInds = arraySizeX-1
132
133
134         Open fullFileNa For Output As 1
135         For m = 0 To yInds
136                 row = ""
137                 For n = 0 To xInds
138                         row = row & Str(dataArr(xInds-n,
                                yInds-m)) & "    "
139                 Next n
140                 Print #1, row
141         Next m
142         Close #1
143
144 End Function
145
146
147 Function SetTraceableByKeyWord( kwName As String,
    traceFlag As Boolean )
148
149         Dim beamDumpKeyNo As Long
150         Dim beamDumpCount As Long
151         Dim itemType As String
152         Dim itemNodes() As Long
153         Dim kwArray(0) As Long
154         Dim m As Long
155
156         itemType = "ent"
157
```

```
158         beamDumpKeyNo = KeywordFind( kwName )
159
160         If beamDumpKeyNo < 0 Then
161                 Print "ERROR: specified keyword " &
                      kwName & " not found. Exiting
                      function."
162                 Exit Function
163         End If
164         kwArray(0) = beamDumpKeyNo
165
166         beamDumpCount = KeywordsGetAppliedItems(
              itemType, kwArray(), itemNodes() )
167
168         For m = 0 To (beamDumpCount - 1)
169                 SetTraceable itemNodes(m), traceFlag
170         Next
171
172         Update
173
174 End Function
```

B.2 Populate Atmosphere Script

```
1  '#Language "WWB-COM"
2
3  Option Explicit
4
5  Sub Main
6
7           Dim voxSA, bufferSA As Double
8           Dim atmosBounds() As Double
9           Dim atmosBoundName As String
10          Dim atmosNo As Long
11          Dim atmosParams(0) As Double
12          Dim PopAtOutput() As Long
13          Dim coatItems(0) As Long
14
15          ClearOutputWindow
```

```
16
17          atmosParams(0) = 5
18
19          voxSA = 4.5
20          bufferSA = 0.5
21
22
23
24          atmosBounds = GetAtmosBounds( "Geometry.
                BoundingBlock" )
25          atmosNo = CreateAtmosphere()
26          PopAtOutput = PopulateAtmosphere( atmosNo,
                atmosBounds, atmosParams, voxSA, bufferSA )
27
28          coatItems(0) = atmosNo
29          SetSurfsAssignCoating( 4, coatItems, True )
30
31
32          Print ""
33          Print "Atmosphere Bounds"
34          Print atmosBounds(0) & " " & atmosBounds(1)
35          Print atmosBounds(2) & " " & atmosBounds(3)
36          Print atmosBounds(4) & " " & atmosBounds(5)
37
38          Update
39
40  End Sub
41
42  Function PopulateAtmosphere( atmosNo As Long,
        atmosBounds() As Double, atmosParams() As Double,
        voxSA As Double, bufferSA As Double ) As Long()
43          '
                ------------------------------------------------------------------------
44          '
45          '       Fills the atmosphere with air voxels.
                First voxel origin is at the
```

```
46          '       xMin,yMin,zMin coordinate. Fills the
                atmosphere with voxels until the
47          '       voxel origin is greater than the xMax,
                yMax, or zMax coord.
48          '
49          '
                ____________________________________________

50          Dim voxCoord(2) As Double
51          Dim voxNumX, voxNumY, voxNumZ As Long
52          Dim numArr(2) As Long
53          Dim xInd, yInd, zInd As Long
54          Dim voxMatName As String
55
56
57
58          ' Set coordinates of the first voxel equal to
                the minimum atmosphere bounds.
59          voxCoord(0) = atmosBounds(0) - bufferSA
60          voxCoord(1) = atmosBounds(2) - bufferSA
61          voxCoord(2) = atmosBounds(4) - bufferSA
62
63          ' Calculate the number of voxels needed to fill
                atmosphere.
64          voxNumX = (atmosBounds(1) - atmosBounds(0))/((
                voxSA + bufferSA) * 2) + 1
65          voxNumY = (atmosBounds(3) - atmosBounds(2))/((
                voxSA + bufferSA) * 2) + 1
66          voxNumZ = (atmosBounds(5) - atmosBounds(4))/((
                voxSA + bufferSA) * 2) + 1
67
68          Print voxNumX & " " & voxNumY & " " & voxNumZ
69
70          ' Loop over the voxel numbers to create each
                voxel.
71          For xInd = 0 To voxNumX
72                  For yInd = 0 To voxNumY
73                          For zInd = 0 To voxNumZ
```

```
74
75                                  ' Create the voxel at
                                        the right x,y,z
                                        coordinates.
76                                  CreateVoxel( atmosNo,
                                        voxMatName, voxCoord,
                                         voxSA )
77
78                                  voxCoord(0) = (
                                        atmosBounds(0) + (
                                        voxSA + bufferSA) * 2
                                         * xInd) - bufferSA
79                                  voxCoord(1) = (
                                        atmosBounds(2) + (
                                        voxSA + bufferSA) * 2
                                         * yInd) - bufferSA
80                                  voxCoord(2) = (
                                        atmosBounds(4) + (
                                        voxSA + bufferSA) * 2
                                         * zInd) - bufferSA
81
82                              Next
83                          Next
84                  Next
85
86                  PopulateAtmosphere = numArr
87
88
89
90  End Function
91
92
93  Function CreateVoxel( atmosNo As Long, voxMatName As
        String, voxCoord() As Double, voxSA As Double ) As
        Long
94          '
```

```
95          '
96          '       Creates a cubic voxel of the material
            specified by voxMatName using the
97          '       T_LENS type template.
98          '
99          '       INPUTS: atmosNo = the node number of the
             atmosphere subassembly [Long]
100         '                       voxMatName = the name of
             the voxel material [String]
101         '                       voxSA = the semiaperture
             of the cubic voxel [Double]
102         '                       voxCoord() = the x (0),
            y (1), z (2) coords of voxel origin [Double]
103         '
104         '       OUTPUTS: the node number of the voxel.
105         '
106         '
            ------------------------------------------------------------

107         Dim lensTemplate As T_LENS
108         Dim lensEnt As T_ENTITY
109         Dim lensOp As T_OPERATION
110         Dim lensNo As Long
111         Dim lensNoArr(0) As Long
112
113         Dim voxMatNames(8) As String
114         Dim randNum As Double
115         Dim matNum As Integer
116         Dim matID As Long
117
118         voxMatNames(0) = "PerturbedAir0"
119         voxMatNames(1) = "PerturbedAir1"
120         voxMatNames(2) = "PerturbedAir2"
121         voxMatNames(3) = "PerturbedAir3"
122         voxMatNames(4) = "PerturbedAir4"
123         voxMatNames(5) = "PerturbedAir5"
124         voxMatNames(6) = "PerturbedAir6"
125         voxMatNames(7) = "PerturbedAir7"
```

```
126         voxMatNames(8) = "PerturbedAir8"
127
128         ' Select a random perturbed material.
129         randNum = 9 * Rnd()
130         matNum = Int(randNum)
131         Print randNum
132         Print matNum
133
134         lensOp.parent = -1
135         lensOp.Type = "Shift"
136         lensOp.val1 = voxCoord(0)
137         lensOp.val2 = voxCoord(1)
138         lensOp.val3 = voxCoord(2)
139
140         ' Set the voxel to be traceable and parented by
              the atmosphere.
141         lensEnt.parent = atmosNo
142         lensEnt.neverTraceable = "False"
143         lensEnt.traceable = "True"
144
145         ' Set the lens parameters
146         lensTemplate.glassCatalog = "Current"
147         lensTemplate.glassName = voxMatNames(matNum)
148         lensTemplate.immerseCatalog = "Current"
149         lensTemplate.immerseName = "Air"
150         lensTemplate.paramType = "Radii"
151         lensTemplate.param1 = 0
152         lensTemplate.param2 = 0
153         lensTemplate.thickness = voxSA*2
154
155         lensNo = AddLens( lensEnt, lensTemplate )
156         lensNoArr(0) = lensNo
157         AddOperation lensNo, lensOp
158         SetElementEdgeRectangle lensNo, voxSA, voxSA
159
160 End Function
161
```

```
162 Function GetAtmosBounds( boundBoxName As String ) As
    Double()
163         '
              ------------------------------------------------------------------------
164         '
165         ' Finds the x, y, and z bounds of the atmosphere
              from the bounding box object.
166         '
167         ' Returns a 5 element Double array which
              contains:
168         '       bounds(0) = xMin coordinate in global
              system.
169         '       bounds(1) = xMax ...
170         '       bounds(2) = yMin ...
171         '       bounds(3) = yMax ...
172         '       bounds(4) = zMin ...
173         '       bounds(5) = zMax ...
174         '
175         ' The bounding box specified by boundBoxName
              should be an element primitive
176         ' block with only one operation (Shift in X, Y,
              Z) applied.
177         '
178         '
              ------------------------------------------------------------------------
179
180         'Dimesion Parameters
181         Dim boxNo As Long
182         Dim xSA As Double
183         Dim ySA As Double
184         Dim zSA As Double
185         Dim bounds(5) As Double
186         Dim boundOp As T_OPERATION
187
188         ' Find the box and get the shift operation data.
189         boxNo = FindFullName( boundBoxName )
```

```
190         GetOperation boxNo, 1, boundOp
191
192         ' Calculate the bounds of the box.
193         bounds(0) = -1 * ElemGetParmValue( boxNo, "a" )
              + boundOp.val1
194         bounds(1) =      ElemGetParmValue( boxNo, "a" )
              + boundOp.val1
195         bounds(2) = -1 * ElemGetParmValue( boxNo, "b" )
              + boundOp.val2
196         bounds(3) =      ElemGetParmValue( boxNo, "b" )
              + boundOp.val2
197         bounds(4) = -1 * ElemGetParmValue( boxNo, "c" )
              + boundOp.val3
198         bounds(5) =      ElemGetParmValue( boxNo, "c" )
              + boundOp.val3
199
200         ' Return the bounds of the atmosphere.
201         GetAtmosBounds = bounds
202
203 End Function
204
205 Function CreateAtmosphere() As Long
206         '
              ------------------------------------------------------------------
207         '
208         ' Creates a subassembly called "Atmosphere" in
              which to store the air voxels.
209         ' If such a subassembly already exists, this
              function will delete it and
210         ' create a new one in order to avoid doubling up
              on the voxel numbers.
211         '
212         '       INPUTS:         None.
213         '       OUTPUTS:        Node number of the
            atmosphere subassembly As Long.
214         '
```

```
215         '
              ------------------------------------------------------------------------

216
217         'Dimension parameters.
218         Dim atmosNo As Long
219         Dim atmosEn As T_ENTITY
220
221         ' Assign parameter values.
222         atmosEn.parent = FindFullName( "Geometry" )
223         atmosEn.name = "Atmosphere"
224         atmosEn.traceable = True
225
226         ' Look for an existing 'atmosphere' sub-array.
227         atmosNo = FindFullName( "Geometry.Atmosphere" )
228
229         ' If 'atmosphere' already exists, delete it.
230         If atmosNo <> -1 Then
231                 DeleteEntity ( atmosNo )
232                 Print "Deleted existing Atmosphere
                      subassembly."
233         End If
234
235         ' Create a new subassembly called Atmosphere.
              Return its node ID.
236         atmosNo = AddSubassembly ( atmosEn )
237         Print "Created new Atmosphere subassembly."
238         CreateAtmosphere = atmosNo
239
240 End Function
```

B.3 Perturb Atmosphere Script

```
1 '#Language "WWB-COM"
2
3 Option Explicit
4
5 Sub Main
```

```
6
7  'Document Cleanup
8  DeleteRays()
9  ARNDeleteAllNodes()
10 ClearOutputWindow()
11
12 Dim expName As String              ' Name of the experiment
       (written into fNames)
13 Dim saveDir As String              ' Name of the directory
     for the data files.
14 Dim analysisNa As String           ' Name of the analysis
     surface being used.
15 Dim phantomKW As String            ' Keyword label on
     phantom to be used as object.
16
17 ' Set filename and save directory for the exported data
     file.
18 saveDir = "C:\Documents\MSc Thesis\ThesisData\Exp 03 -
     LFTDH\"
19 expName = "FP1"
20
21
22 ' Set the analysis name and phantom name.
23 analysisNa = "Analysis Surface(s).CMOSChip"
24 phantomKW = "FPSheet"
25
26
27 ' Trace rays and save the resulting reference and object
       holograms.
28 ExportRefIrr( saveDir, expName, analysisNa )
29 Print "Reference hologram successfully acquired."
30 ExportObjIrr( saveDir, expName, analysisNa, phantomKW )
31 Print "Object hologram successfully acquired."
32
33
34
35 End Sub
36
```

```
37 Function ExportRefIrr( saveDir As String, fName As
      String, anaSurfName As String )
38
39         'Dimension save parameters.
40         Dim saveName As String
41
42         saveName = saveDir & fName & "Ref.dat"
43
44         ' Dimension analysis surface parameters.
45         Dim anaNode As Long
46         Dim ana As T_ANALYSIS
47         Dim noPixX As Long
48         Dim noPixY As Long
49
50         anaNode = FindFullName( anaSurfName )
51         LoadAnalysis(anaNode, ana )
52         noPixX = 1 + ana.Amax - ana.Amin
53         noPixY = 1 + ana.Bmax - ana.Bmin
54
55         ' Set the beam dumps and all phantom objects to
              be untracable.
56         SetTraceableByKeyWord( "BeamDumps", False )
57         SetTraceableByKeyWord( "Phantoms", False )
58
59         'Ensure the attenuator is traceable
60         SetTraceableByKeyWord( "Attenuator", True )
61
62         ' Dimension ARN node and array to store
              irradiance map.
63         Dim arnNode As Long
64         Dim irrad() As Double
65
66         ' Trace rays and extract irradiance data.
67         EnableTextPrinting(False)
68         TraceCreate
69         IrradianceToARN( anaNode, "IrradMap", arnNode )
70         ARNGetDataAsDoubleArray ( arnNode, irrad() )
71         EnableTextPrinting(True)
```

```
72
73          WriteArrayToFile( saveName, irrad, noPixX,
                noPixY )
74
75          Update
76
77  End Function
78
79  Function ExportObjIrr( saveDir As String, fName As
        String, anaSurfName As String, phantomKW As String )
80
81          'Dimension save parameters.
82          Dim saveName As String
83
84          saveName = saveDir & fName & "Obj.dat"
85
86          ' Dimension analysis surface parameters.
87          Dim anaNode As Long
88          Dim ana As T_ANALYSIS
89          Dim noPixX As Long
90          Dim noPixY As Long
91
92          anaNode = FindFullName( anaSurfName )
93          LoadAnalysis(anaNode, ana )
94          noPixX = 1 + ana.Amax - ana.Amin
95          noPixY = 1 + ana.Bmax - ana.Bmin
96
97          ' Set the beam dumps and all phantom objects to
                be untracable.
98          SetTraceableByKeyWord( "BeamDumps", False )
99          SetTraceableByKeyWord( "Phantoms", False )
100
101         'Ensure the attenuator is traceable
102         SetTraceableByKeyWord( "Attenuator", True )
103
104         ' Set the phantom to traceable.
105         SetTraceableByKeyWord( phantomKW, True )
106
```

```
107         ' Dimension ARN node and array to store
                irradiance map.
108         Dim arnNode As Long
109         Dim irrad() As Double
110
111         ' Trace rays and extract irradiance data.
112         EnableTextPrinting(False)
113         TraceCreate
114         IrradianceToARN( anaNode, "IrradMap", arnNode )
115         ARNGetDataAsDoubleArray ( arnNode, irrad() )
116         EnableTextPrinting(True)
117
118         WriteArrayToFile( saveName, irrad, noPixX,
                noPixY )
119
120         Update
121
122 End Function
123
124 Function WriteArrayToFile( fullFileNa As String, dataArr
    () As Double, arraySizeX As Long, arraySizeY As Long
    )
125
126         Dim m As Long, n As Long
127         Dim row As String
128         Dim xInds As Long, yInds As Long
129
130         yInds = arraySizeY-1
131         xInds = arraySizeX-1
132
133
134         Open fullFileNa For Output As 1
135         For m = 0 To yInds
136                 row = ""
137                 For n = 0 To xInds
138                         row = row & Str(dataArr(xInds-n,
                            yInds-m)) & "    "
139                 Next n
```

```
140                 Print #1, row
141         Next m
142         Close #1
143
144 End Function
145
146
147 Function SetTraceableByKeyWord( kwName As String,
        traceFlag As Boolean )
148
149         Dim beamDumpKeyNo As Long
150         Dim beamDumpCount As Long
151         Dim itemType As String
152         Dim itemNodes() As Long
153         Dim kwArray(0) As Long
154         Dim m As Long
155
156         itemType = "ent"
157
158         beamDumpKeyNo = KeywordFind( kwName )
159
160         If beamDumpKeyNo < 0 Then
161                 Print "ERROR: specified keyword " &
                        kwName & " not found. Exiting
                        function."
162                 Exit Function
163         End If
164         kwArray(0) = beamDumpKeyNo
165
166         beamDumpCount = KeywordsGetAppliedItems(
                itemType, kwArray(), itemNodes() )
167
168         For m = 0 To (beamDumpCount - 1)
169                 SetTraceable itemNodes(m), traceFlag
170         Next
171
172         Update
173
```

```
End Function
```

B.4 Heat Expansion Scripts

```
Sub Main

Dim opticH      As Double       'OpticHeight.
Dim deltaT      As Double       'Temp change.
Dim expCoeff    As Double       'Expansion coefficient.
Dim opticNo()   As Long         'Holder for optic nodes
    no's.
Dim kwRet       As Long         'Holder for keyword
    number.

'Document Cleanup
DeleteRays()
ARNDeleteAllNodes()
ClearOutputWindow()

' Set the coefficients
expCoeff = 23.1E-6

' Calculate heat expansion factor.
fac = expCoeff * deltaT

' Find all elements with the keyword 'Optic'.
kwRet = KeywordsGetAppliedItems( 'ent', 'Optic', opticNo
    () )

' Perturb each optic.
for i = 0 To kwRet
        HeatExpandOptic(opticNo(i)
next i

End Sub
```

B.5 Vibration Scripts

```
'#Language "WWB-COM"

Option Explicit

Sub Main

Dim vibrations() As Double          ' Amplitude of
    vibrations.
Dim expTime As Long                 ' Exposure time (ms)
Dim opti As integer                 ' Optic index
Dim holi As integer                 ' Hologram Index
Dim expName As String               ' Name of the experiment
     (written into fNames)
Dim saveDir As String               ' Name of the directory
    for the data files.
Dim analysisNa As String            ' Name of the analysis
    surface being used.
Dim phantomKW As String             ' Keyword label on
    phantom to be used as object.


'Document Cleanup
DeleteRays()
ARNDeleteAllNodes()
ClearOutputWindow()

' Set filename and save directory for the exported data
    file.
saveDir = "C:\Documents\MSc Thesis\ThesisData\Exp 03 -
    LFTDH\"
expName = "FP1"

' Set the analysis name and phantom name.
analysisNa = "Analysis Surface(s).CMOSChip"
phantomKW = "FPSheet"

' Get node numbers of all optics.
```

```
kwRet = KeywordsGetAppliedItems( 'ent', 'Optic', opticNo() )

for holi = 0 To expTime
        for i = 0 To kwRet

                VibrateOptic(opticNo(i), opticH, vibrations())

        next i

        holNo = str(holi)

        ' Trace rays and save the resulting reference and object holograms.
        ExportRefIrrTA( saveDir, expName, holNo, analysisNa )
        Print "Reference hologram successfully acquired."
        ExportObjIrrTA( saveDir, expName, holNo, analysisNa, phantomKW )
        Print "Object hologram successfully acquired."

next holi

End Sub

Function VibrateOptic( opticNo As Long, opticH As Double, vibrations() As Double )

        Dim len As Long
        Dim amp As Double
        Dim i As Integer
        Dim xTrans As Double
        Dim yTrans As Double
        Dim zTrans As Double
        Dim xyRot As Double
        Dim yzRot As Double
```

```
62
63          len = vibrations.length
64          amp = 0
65
66          for i = 1 To len
67                  amp += vibrations(i)
68          next i
69          amp = amp/i
70
71          xTrans = rnd() * amp
72          yTrans = rnd() * amp
73          zTrans = rnd() * amp
74          xyRot = atan(xTrans/(opticH+yTrans))
75          yzRot = atan(zTrans/(opticH+yTrans))
76
77  End Function
78
79  Function ExportRefIrrTA( saveDir As String, fName As
        String, holNo As String, anaSurfName As String )
80
81          'Dimension save parameters.
82          Dim saveName As String
83
84          saveName = saveDir & fName & "Ref" & holNo & ".
                dat"
85
86          ' Dimension analysis surface parameters.
87          Dim anaNode As Long
88          Dim ana As T_ANALYSIS
89          Dim noPixX As Long
90          Dim noPixY As Long
91
92          anaNode = FindFullName( anaSurfName )
93          LoadAnalysis(anaNode, ana )
94          noPixX = 1 + ana.Amax - ana.Amin
95          noPixY = 1 + ana.Bmax - ana.Bmin
96
```

```
97          ' Set the beam dumps and all phantom objects to
               be untracable.
98          SetTraceableByKeyWord( "BeamDumps", False )
99          SetTraceableByKeyWord( "Phantoms", False )
100
101         'Ensure the attenuator is traceable
102         SetTraceableByKeyWord( "Attenuator", True )
103
104         ' Dimension ARN node and array to store
               irradiance map.
105         Dim arnNode As Long
106         Dim irrad() As Double
107
108         ' Trace rays and extract irradiance data.
109         EnableTextPrinting(False)
110         TraceCreate
111         IrradianceToARN( anaNode, "IrradMap", arnNode )
112         ARNGetDataAsDoubleArray ( arnNode, irrad() )
113         EnableTextPrinting(True)
114
115         WriteArrayToFile( saveName, irrad, noPixX,
               noPixY )
116
117         Update
118
119 End Function
120
121 Function ExportObjIrr( saveDir As String, fName As
       String, holNo as String, anaSurfName As String,
       phantomKW As String )
122
123         'Dimension save parameters.
124         Dim saveName As String
125
126         saveName = saveDir & fName & "Obj" & holNo & ".
               dat"
127
128         ' Dimension analysis surface parameters.
```

```
129         Dim anaNode As Long
130         Dim ana As T_ANALYSIS
131         Dim noPixX As Long
132         Dim noPixY As Long
133
134         anaNode = FindFullName( anaSurfName )
135         LoadAnalysis(anaNode, ana )
136         noPixX = 1 + ana.Amax - ana.Amin
137         noPixY = 1 + ana.Bmax - ana.Bmin
138
139         ' Set the beam dumps and all phantom objects to
              be untracable.
140         SetTraceableByKeyWord( "BeamDumps", False )
141         SetTraceableByKeyWord( "Phantoms", False )
142
143         'Ensure the attenuator is traceable
144         SetTraceableByKeyWord( "Attenuator", True )
145
146         ' Set the phantom to traceable.
147         SetTraceableByKeyWord( phantomKW, True )
148
149         ' Dimension ARN node and array to store
              irradiance map.
150         Dim arnNode As Long
151         Dim irrad() As Double
152
153         ' Trace rays and extract irradiance data.
154         EnableTextPrinting(False)
155         TraceCreate
156         IrradianceToARN( anaNode, "IrradMap", arnNode )
157         ARNGetDataAsDoubleArray ( arnNode, irrad() )
158         EnableTextPrinting(True)
159
160         WriteArrayToFile( saveName, irrad, noPixX,
              noPixY )
161
162         Update
163
```

```
164 End Function
165
166 Function WriteArrayToFile( fullFileNa As String, dataArr
    () As Double, arraySizeX As Long, arraySizeY As Long
    )
167
168         Dim m As Long, n As Long
169         Dim row As String
170         Dim xInds As Long, yInds As Long
171
172         yInds = arraySizeY-1
173         xInds = arraySizeX-1
174
175
176         Open fullFileNa For Output As 1
177         For m = 0 To yInds
178                 row = ""
179                 For n = 0 To xInds
180                         row = row & Str(dataArr(xInds-n,
                                yInds-m)) & "    "
181                 Next n
182                 Print #1, row
183         Next m
184         Close #1
185
186 End Function
187
188
189 Function SetTraceableByKeyWord( kwName As String,
    traceFlag As Boolean )
190
191         Dim beamDumpKeyNo As Long
192         Dim beamDumpCount As Long
193         Dim itemType As String
194         Dim itemNodes() As Long
195         Dim kwArray(0) As Long
196         Dim m As Long
197
```

```
198         itemType = "ent"
199
200         beamDumpKeyNo = KeywordFind( kwName )
201
202         If beamDumpKeyNo < 0 Then
203                 Print "ERROR: specified keyword " &
                        kwName & " not found. Exiting
                        function."
204                 Exit Function
205         End If
206         kwArray(0) = beamDumpKeyNo
207
208         beamDumpCount = KeywordsGetAppliedItems(
                itemType, kwArray(), itemNodes() )
209
210         For m = 0 To (beamDumpCount - 1)
211                 SetTraceable itemNodes(m), traceFlag
212         Next
213
214         Update
215
216 End Function
```